THE BELL SYSTEM
TECHNICAL JOURNAL

DEVOTED TO THE SCIENTIFIC AND ENGINEERING
ASPECTS OF ELECTRICAL COMMUNICATION

Volume 53 July–August 1974 Number 6

Scattering of a Plane Electromagnetic Wave by Axisymmetric Raindrops

By J. A. MORRISON and M.-J. CROSS

(Manuscript received January 9, 1974)

This paper gives details of the analytical and numerical procedures used to solve the basic problem of the scattering of a plane electromagnetic wave by an axisymmetric raindrop. A nonperturbative solution is obtained by expanding the scattered and transmitted fields in terms of spherical vector wave functions, so that Maxwell's equations are satisfied exactly in the regions exterior and interior to the raindrop, and by combining point matching with least-squares fitting to satisfy the boundary conditions on the surface of the raindrop with sufficient accuracy.

Numerical results are presented for scattering by oblate spheroidal raindrops, with eccentricity depending on (and increasing with) drop size, for two orthogonal polarizations of the incident wave. The calculations were made at 4, 11, 18.1, and 30 GHz, in the case in which the direction of propagation of the incident wave is perpendicular to the axis of symmetry of the raindrop, which is of interest for terrestrial microwave relay systems. At 30 GHz, the calculations were also made for the case in which the angle between the direction of propagation and the axis of symmetry is 70° and 50°, since different elevation angles are of interest for satellite systems. These basic results were summed earlier over the drop-size distribution to calculate the differential attenuation and differential phase shift caused by rain, which are of importance in the investigation of cross polarization in radio communication systems.

We also derive the first-order perturbation approximation to the scattering by axisymmetric raindrops that are nearly spherical, which generalizes Oguchi's results for spheroidal raindrops with small eccentricity. Some simplifications that may be made in his formulas are pointed out. The perturbation results serve as a useful check on the least-squares-fitting procedure applied to spheroidal raindrops with small eccentricity. In addition, considerable improvement is obtained in the closeness of the perturbation results to the least-squares-fitting ones, in particular for the larger drop sizes, by perturbing about an equivolumic spherical raindrop, with appropriate perturbation parameter, rather than perturbing about an inscribed spherical raindrop, as did Oguchi. Similar comparisons were also made earlier for the rain-induced differential attenuation and differential phase shift, and these quantities were calculated approximately at frequencies up to 100 GHz, using the results corresponding to perturbation about the equivolumic spherical raindrop. The perturbation results are obtained quite inexpensively, whereas the least-squares-fitting procedure is very costly.

I. INTRODUCTION

In a recent short note, the authors and Chu[1] gave calculated results of differential attenuation and differential phase shift caused by rain, based on scattering of a plane electromagnetic wave by oblate spheroidal raindrops. These results are of importance in the investigation of cross polarization in radio communications systems. In this paper, we give details of the analytical and numerical procedures used to solve the problem of scattering by a single raindrop, which were only outlined in the note. Although the results given in this paper are for oblate spheroidal raindrops, the procedures are applicable for axisymmetric raindrops that are not too nonspherical, and calculations could be made for raindrops that are more flattened on the bottom than on the top, such as for the shapes determined by Pruppacher and Pitter.[2]

Two polarizations of the incident wave, designated I and II, are considered, as depicted in Fig. 1. The factor $e^{-i\omega t}$ has been suppressed. In the first polarization, the electric field is parallel to the plane containing the axis of symmetry of the raindrop and the direction of propagation of the incident wave. In the second polarization, the electric field is perpendicular to this plane. The angle between the direction of propagation and the axis of symmetry is denoted by α. In terrestrial microwave relay systems, $\alpha = 90°$ is of main concern, but other values of α are of interest for satellite systems.

The incident wave induces a transmitted field in the interior of the raindrop and a scattered field. In the far field, the quantities of primary interest are the complex forward scattering amplitudes,[3] $S_{\mathrm{I}}(0)$ and $S_{\mathrm{II}}(0)$. In the two polarizations considered, the polarization of the far scattered field in the forward direction is the same as that of the incident wave. Also of basic interest are the cross sections of the raindrop. The total cross sections Q_t^{I} and Q_t^{II} are given in terms of the real parts of the forward scattering amplitudes by eq. (39), where k_0 is the free space wave number. We also calculate the scattering cross sections Q_s^{I} and Q_s^{II}. The absorption cross sections Q_a^{I} and Q_a^{II} are given in terms of the total and scattering cross sections by (38).

In Section II, we discuss the formulation of the problem of the scattering of a plane electromagnetic wave by a single raindrop. Spherical coordinates are chosen with polar axis along the axis of symmetry of the raindrop, and origin interior to it, as in Fig. 2. The scattered field is expanded in terms of solutions of the vector wave equation, with wave number k_0, which satisfy the radiation condition. An analogous expansion is assumed for the transmitted field inside the raindrop, in terms of vector wave functions, with wave number $k_1 = Nk_0$, which are finite at the origin. Here, N is the complex refractive index of the raindrop. The complex coefficients in the expansions are to be determined by satisfying the boundary conditions, namely, the continuity of the tangential components of the total electric and magnetic fields across the surface of the raindrop.

In Section III, the incident field is expanded in a (complex) Fourier series in the azimuthal angle φ. Because of the axial symmetry of the raindrop, the problem can be decomposed and the boundary conditions satisfied independently for each term of the Fourier series. In Section III, expressions are also given for the forward scattering amplitudes and the scattering cross sections in terms of the coefficients in the expansion of the scattered field. In addition, we express the total and scattering cross sections for an elliptically polarized incident wave in terms of those for the two linearly polarized incident waves under consideration.

In Section IV, we give expressions for the first-order approximations to the coefficients in the expansions of the scattered and transmitted fields for axisymmetric raindrops that are nearly spherical. These results generalize those given by Oguchi[4] for spheroidal raindrops with small eccentricity. Since our derivation follows closely the one given by Oguchi, we omit most details. However, we point out some simplifications that may be made in his expressions.

In Section V, we discuss an approximate nonperturbative solution to the problem of scattering by an axisymmetric raindrop. For each term in the Fourier series expansion in the azimuthal angle φ, the four boundary conditions should be satisfied on the cross-sectional boundary curve $r = R(\theta)$, $0 \leqq \theta \leqq \pi$, which defines the shape of the raindrop. Only a finite number of coefficients in the expansions of the scattered and transmitted fields is considered. These coefficients are determined approximately by requiring the boundary conditions to be satisfied in a least-squares sense at a total number of points on the cross-sectional curve that is greater than the number of unknown coefficients.

In Section V, we also discuss the advantage of using least-squares fitting rather than collocation, in which the total number of fitting points is equal to the number of unknown coefficients that are then determined by solving a system of simultaneous linear equations. After we had completed the calculations for scattering by oblate spheroidal raindrops at 4, 18.1, and 30 GHz, a paper was published by Oguchi[5] in which he carried out similar calculations for $\alpha = 90°$ at 19.3 and 34.8 GHz and used collocation for the expansions in terms of spherical vector wave functions. At 34.8 GHz, he also used an expansion in terms of spheroidal wave functions and truncated the infinite system of equations which he derived from the boundary conditions.

In Section VI, the least-squares-fitting program and some subsidiary programs are discussed. The numerical routines used for calculating the special functions that enter into the boundary conditions are also described. In addition, some indication of the running times involved and the storage requirements are given.

In Section VII, we first discuss the checks that were made on the least-squares-fitting program. These include comparison with the Mie theory[6] of the results of scattering by spherical raindrops at different angles of incidence. We also compare extrapolated results for oblate spheroidal raindrops with small eccentricity to the first-order perturbation results.

We then discuss our calculations of the scattering by oblate spheroidal raindrops, for which the ratio of minor to major semiaxis depends linearly on the radius $\bar{a}$ (in centimeters) of the equivolumic spherical drop; specifically,

$$a/b = (1 - \bar{a}), \qquad ab^2 - \bar{a}^3. \tag{1}$$

This relationship is similar to that used by Oguchi.[4,5] The rain-induced attenuation and phase shift were calculated[1] for both polarizations by

summing the real and imaginary parts of the forward scattering amplitudes over the Laws and Parsons drop-size distribution, as quoted by Setzer.[7] Thus, for rain rates up to 150 milimeters per hour, there are 14 different drop sizes, $\bar{a} = 0.025(0.025)0.35$, to be considered.

The calculations were done for wavelengths of 7.5, 2.727, 1.6575, and 1.0 cm, corresponding to frequencies of approximately 4, 11, 18.1, and 30 GHz. The refractive indices N at 20°C were obtained from an elaborate fitting equation in a recently published survey[8] of available measured data (except at 4 GHz, for which older data were used, since the calculations at that frequency were made at an earlier date). The angle of incidence α was taken to be 90° at 4, 11, and 18.1 GHz, while at 30 GHz the calculations were done for $\alpha = 70°$ and $\alpha = 50°$ also. The calculated values of the forward scattering amplitudes $S_{\mathrm{I}}(0)$ and $S_{\mathrm{II}}(0)$ are given in Tables II to VII, and those of the total cross sections Q_t^{I} and Q_t^{II} and the scattering cross sections Q_s^{I} and Q_s^{II} are given in Tables VIII to XIII. Section VII concludes by discussing some calculations using collocation and mentioning some checks on Oguchi's calculations at 19.3 and 34.8 GHz.

In Section VIII, we compare three sets of first-order perturbation results with those obtained by least-squares fitting for oblate spheroidal raindrops. One set of results corresponds to perturbation about a spherical raindrop with radius equal to the length a of the minor semiaxis of the spheroidal raindrop, which was the procedure used by Oguchi.[4] The other two sets correspond to perturbations about the equivolumic spherical raindrop, with different perturbation parameters that are consistent for small drop sizes. Considerable improvement is obtained in the closeness of the perturbation results to the least-squares-fit results by perturbing about the equivolumic spherical raindrop with the appropriate perturbation parameter. The comparisons are presented graphically in Figs. 3 to 14. The values of the forward scattering amplitude $S(0)$ and the total and scattering cross sections Q_t and Q_s for the equivolumic spherical raindrops are given in Tables XIV to XVII. These values are independent of the polarization of the incident wave and of the angle of incidence α.

The three sets of perturbation results for the differential quantities $Q_{t_1}^{\mathrm{II}} - Q_t^{\mathrm{I}}$ and $\mathrm{Im}[S_{\mathrm{I}}(0) - S_{\mathrm{II}}(0)]$ are compared in Figs. 15 to 23 with those obtained by least-squares fitting for oblate spheroidal raindrops. Again, considerable improvement is obtained by perturbing about the equivolumic spherical raindrop. In a recent short note,[9] similar comparisons were made for the rain-induced differential attenuation and differential phase shift. Moreover, these quantities were calculated

approximately at frequencies up to 100 GHz, using the two sets of results corresponding to perturbations about the equivolumic spherical raindrop. The perturbation results are obtained quite inexpensively, whereas the least-squares-fitting procedure is very costly.

The appendices contain some details that it was considered desirable to omit from the main text.

II. FORMULATION OF PROBLEM

We now consider the problem of scattering of a plane electromagnetic wave by a single raindrop. Suppressing the factor $e^{-i\omega t}$, where ω is the angular frequency, the divergenceless electric and magnetic fields **E** and **H** satisfy Maxwell's equations[10]

$$\nabla \times \mathbf{E} = i\omega\mu_0\mathbf{H}, \qquad \nabla \times \mathbf{H} = (\sigma - i\omega\epsilon)\mathbf{E}, \tag{2}$$

where μ_0 is the constant permeability, σ is the conductivity, and ϵ is the dielectric constant. Exterior to the raindrop $\sigma = 0$ and $\epsilon = \epsilon_0$, while interior to it $\sigma = \sigma_1$ and $\epsilon = \epsilon_1$. The appropriate boundary conditions[11] are that the tangential components of the total electric and magnetic fields be continuous across the surface of the raindrop. Let

$$k^2 = \omega\mu_0(\omega\epsilon + i\sigma), \tag{3}$$

with $\mathrm{Re}(k) > 0$. Then the free space wave number is $k_0 = \omega(\mu_0\epsilon_0)^{\frac{1}{2}}$ and the wave number in the raindrop is

$$k_1 = Nk_0, \tag{4}$$

where N is the complex index of refraction of water.

We consider two polarizations of the incident wave depicted in Fig. 1. We choose Cartesian coordinates (x, y, z) with origin interior to the

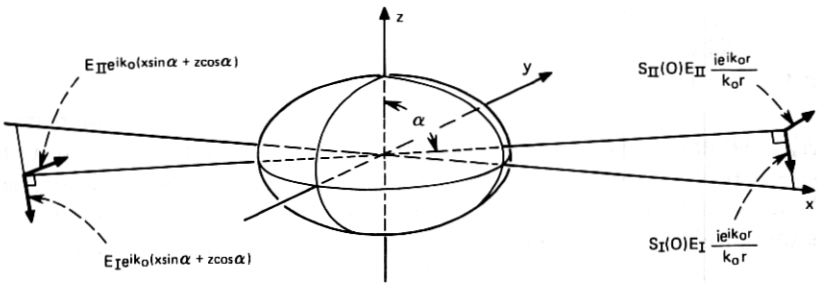

Fig. 1—Two polarizations of the incident wave.

raindrop and z-axis coinciding with the axis of symmetry of the raindrop. The direction of propagation of the incident wave is perpendicular to the y-axis and inclined at an angle α to the z-axis. In the first polarization, the magnetic field is assumed parallel to the y-axis and the incident fields are given by

$$\begin{aligned} \mathbf{E}_{\mathrm{I}}^{i} &= E_{\mathrm{I}}(\cos\alpha\mathbf{i} - \sin\alpha\mathbf{k}) \exp\left[ik_0(x\sin\alpha + z\cos\alpha)\right], \\ \mathbf{H}_{\mathrm{I}}^{i} &= \frac{k_0}{\omega\mu_0} E_{\mathrm{I}}\mathbf{j} \exp\left[ik_0(x\sin\alpha + z\cos\alpha)\right], \end{aligned} \tag{5}$$

where $\mathbf{i}$, $\mathbf{j}$, and $\mathbf{k}$ denote unit vectors parallel to the coordinate axes. In the second polarization, the electric field is assumed parallel to the y-axis and the incident fields are given by

$$\mathbf{E}_{\mathrm{II}}^{i} = E_{\mathrm{II}}\mathbf{j} \exp\left[ik_0(x\sin\alpha + z\cos\alpha)\right]$$

and (6)

$$\mathbf{H}_{\mathrm{II}}^{i} = \frac{-k_0}{\omega\mu_0} E_{\mathrm{II}}(\cos\alpha\mathbf{i} - \sin\alpha\mathbf{k}) \exp\left[ik_0(x\sin\alpha + z\cos\alpha)\right].$$

We now consider the problem of representing the scattered and transmitted fields induced by the incident wave. It is convenient to introduce spherical coordinates (r, θ, φ) with corresponding unit vectors $\mathbf{i}_1$, $\mathbf{i}_2$, and $\mathbf{i}_3$ as depicted in Fig. 2. Then the equations

$$\nabla \times \mathbf{M} = k\mathbf{N}, \qquad \nabla \times \mathbf{N} = k\mathbf{M} \tag{7}$$

are satisfied by the spherical vector wave functions,[12]

$$\mathbf{M}_{mn}(k) = z_n(kr)e^{im\varphi}\left[\frac{im}{\sin\theta} P_n^{|m|}(\cos\theta)\mathbf{i}_2 - \frac{dP_n^{|m|}(\cos\theta)}{d\theta}\mathbf{i}_3\right] \tag{8}$$

and

$$\begin{aligned} \mathbf{N}_{mn}(k) = e^{im\varphi}\Bigg\{ & n(n+1)\frac{z_n(kr)}{kr} P_n^{|m|}(\cos\theta)\mathbf{i}_1 + \left[\frac{z_n(kr)}{kr} + z_n'(kr)\right] \\ & \times \left[\frac{dP_n^{|m|}(\cos\theta)}{d\theta}\mathbf{i}_2 + \frac{im}{\sin\theta} P_n^{|m|}(\cos\theta)\mathbf{i}_3\right]\Bigg\}. \end{aligned} \tag{9}$$

Here z_n denotes a spherical Bessel function[13] of order n and $P_n^{|m|}$ denotes the associated Legendre function[14] (of the first kind) of degree n and order $|m|$, where m is a positive or negative integer, and n is an integer with $n \geqq |m|$ and $n \neq 0$. The prime denotes derivative with respect to the argument. As a matter of convenience, we have chosen to use complex linear combinations of the even and odd spherical vector wave functions.[12]

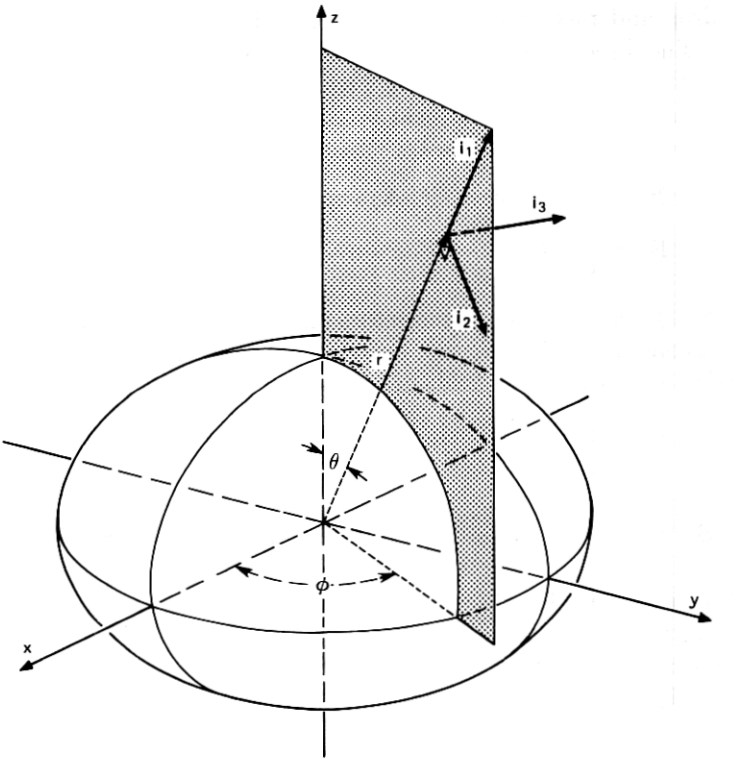

Fig. 2—Cartesian and spherical coordinates.

Outside the raindrop, the total electromagnetic field is the sum of the incident field of the plane wave and the scattered field. The scattered field must satisfy the radiation condition and, consequently, in view of eqs. (2), (3), and (7), we assume expansions of the form

$$\mathbf{E}^s = -\sum_{m=-\infty}^{\infty} \sum_{\substack{n \geqq |m| \\ n \neq 0}} [a_{mn}\mathbf{M}_{mn}^{(3)}(k_0) + b_{mn}\mathbf{N}_{mn}^{(3)}(k_0)] \tag{10}$$

and

$$\mathbf{H}^s = \frac{ik_0}{\omega\mu_0} \sum_{m=-\infty}^{\infty} \sum_{\substack{n \geqq |m| \\ n \neq 0}} [a_{mn}\mathbf{N}_{mn}^{(3)}(k_0) + b_{mn}\mathbf{M}_{mn}^{(3)}(k_0)], \tag{11}$$

where the superscript 3 denotes that spherical Bessel functions of the third kind, i.e., spherical Hankel functions of the first kind, are used.

Thus, in (8) and (9), $z_n(k_0r) = h_n^{(1)}(k_0r)$. For $k_0r \gg 1$,

$$h_n^{(1)}(k_0r) \sim \frac{(-i)^{n+1}}{k_0r} e^{ik_0r}, \tag{12}$$

so that the expansions in (10) and (11) involve outgoing waves.

Analogous expansions are assumed for the transmitted field inside the raindrop except that, since the origin of the coordinate system is interior to the raindrop, spherical Bessel functions of the first kind must be used so that the field remains finite at $r = 0$. Also, the wave number inside the raindrop is k_1, as given by (4). Thus, we assume expansions of the form

$$\mathbf{E}^t = -\sum_{m=-\infty}^{\infty} \sum_{\substack{n \geqq |m| \\ n \neq 0}} [c_{mn}\mathbf{M}_{mn}^{(1)}(k_1) + d_{mn}\mathbf{N}_{mn}^{(1)}(k_1)] \tag{13}$$

and

$$\mathbf{H}^t = \frac{ik_1}{\omega\mu_0} \sum_{m=-\infty}^{\infty} \sum_{\substack{n \geqq |m| \\ n \neq 0}} [c_{mn}\mathbf{N}_{mn}^{(1)}(k_1) + d_{mn}\mathbf{M}_{mn}^{(1)}(k_1)], \tag{14}$$

where the superscript 1 indicates that $z_n(k_1r) = j_n(k_1r)$ in (8) and (9).

The unknown (complex) coefficients a_{mn}, b_{mn}, c_{mn}, and d_{mn} in (10), (11), (13), and (14) must be determined from the boundary conditions. The surface of the raindrop is given by

$$r = R(\theta), \qquad 0 \leqq \theta \leqq \pi, \qquad 0 \leqq \varphi \leqq 2\pi, \tag{15}$$

where it is assumed that $R(\theta)$ is a single-valued, continuously differentiable function of θ. The continuity of the tangential components of the total electric and magnetic fields across the surface of the raindrop implies that, for $r = R(\theta)$,

$$E_3^i + E_3^s = E_3^t, \tag{16}$$

$$H_3^i + H_3^s = H_3^t, \tag{17}$$

$$E_2^i + E_2^s + \frac{1}{R}\frac{dR}{d\theta}(E_1^i + E_1^s) = E_2^t + \frac{1}{R}\frac{dR}{d\theta}E_1^t, \tag{18}$$

$$H_2^i + H_2^s + \frac{1}{R}\frac{dR}{d\theta}(H_1^i + H_1^s) = H_2^t + \frac{1}{R}\frac{dR}{d\theta}H_1^t, \tag{19}$$

where $E_j = \mathbf{E}\cdot\mathbf{i}_j$ and $H_j = \mathbf{H}\cdot\mathbf{i}_j$ and the incident fields $\mathbf{E}^i$ and $\mathbf{H}^i$ are given by (5) or (6).

III. FAR-FIELD QUANTITIES

Because of the axial symmetry of the raindrop, it is convenient to expand the incident plane wave in a (complex) Fourier series in the azimuthal angle φ, and we write

$$\mathbf{E}^i = \sum_{m=-\infty}^{\infty} \mathbf{e}_m(r, \theta)e^{im\varphi}, \qquad \mathbf{H}^i = \sum_{m=-\infty}^{\infty} \mathbf{h}_m(r, \theta)e^{im\varphi}. \tag{20}$$

It follows from (5) and (6) that

$$\mathbf{e}_m^{\mathrm{I}}(r, \theta) = E_{\mathrm{I}}\mathbf{f}_m(r, \theta), \qquad \mathbf{h}_m^{\mathrm{I}}(r, \theta) = E_{\mathrm{I}} \frac{k_0}{\omega\mu_0} \mathbf{g}_m(r, \theta) \tag{21}$$

and

$$\mathbf{e}_m^{\mathrm{II}}(r, \theta) = E_{\mathrm{II}}\mathbf{g}_m(r, \theta), \qquad \mathbf{h}_m^{\mathrm{II}}(r, \theta) = -E_{\mathrm{II}} \frac{k_0}{\omega\mu_0} \mathbf{f}_m(r, \theta), \tag{22}$$

where expressions for $\mathbf{f}_m(r, \theta)$ and $\mathbf{g}_m(r, \theta)$ are derived in Appendix A and are given by eqs. (79) and (80).

If the boundary conditions (16) to (19) are multiplied by $e^{-im\varphi}$ and integrated with respect to φ from 0 to 2π, then a set of four equations involving the unknown coefficients a_{mn}, b_{mn}, c_{mn}, and d_{mn} is obtained for each m. These equations are given by (81) to (84) in Appendix A, where we have used the notations $e_{mj} = \mathbf{e}_m \cdot \mathbf{i}_j$ and $h_{mj} = \mathbf{h}_m \cdot \mathbf{i}_j$. It follows readily from (21), (22), and (79) to (84) that, for the first polarization of the incident wave,

$$\begin{aligned} a_{-mn}^{\mathrm{I}} &= -a_{mn}^{\mathrm{I}}, & b_{-mn}^{\mathrm{I}} &= b_{mn}^{\mathrm{I}}, \\ c_{-mn}^{\mathrm{I}} &= -c_{mn}^{\mathrm{I}}, & d_{-mn}^{\mathrm{I}} &= d_{mn}^{\mathrm{I}}, \end{aligned} \tag{23}$$

and for the second polarization

$$\begin{aligned} a_{-mn}^{\mathrm{II}} &= a_{mn}^{\mathrm{II}}, & b_{-mn}^{\mathrm{II}} &= -b_{mn}^{\mathrm{II}}, \\ c_{-mn}^{\mathrm{II}} &= c_{mn}^{\mathrm{II}} & d_{-mn}^{\mathrm{II}} &= -d_{mn}^{\mathrm{II}}. \end{aligned} \tag{24}$$

Thus, it is sufficient to consider only nonnegative values of m.

It is worth noting that, if the raindrop is symmetrical about the plane $\theta = \pi/2$, i.e., $R(\pi - \theta) = R(\theta)$, $0 \leqq \theta \leqq \pi/2$, then some further reductions may be made. In particular, in the case $\alpha = \pi/2$, it is found that

$$\begin{aligned} a_{m,|m|+2s+1}^{\mathrm{I}} &= 0 = c_{m,|m|+2s+1}^{\mathrm{I}}, \\ b_{m,|m|+2s}^{\mathrm{I}} &= 0 = d_{m,|m|+2s}^{\mathrm{I}}, \end{aligned} \tag{25}$$

and

$$\begin{aligned} a_{m,|m|+2s}^{\mathrm{II}} &= 0 = c_{m,|m|+2s}^{\mathrm{II}}, \\ b_{m,|m|+2s+1}^{\mathrm{II}} &= 0 = d_{m,|m|+2s+1}^{\mathrm{II}}, \end{aligned} \tag{26}$$

for $s = 0, 1, 2, \cdots$, so that alternate coefficients vanish. Reductions

may still be made in the case of $\alpha \neq \pi/2$ by considering the sum and the difference of the boundary conditions corresponding to α and to $\hat{\alpha} = (\pi - \alpha)$, as shown in Appendix B. We have not utilized these reductions in the program for calculating the unknown coefficients, since we wanted the program to be applicable to raindrops without a meridional plane of symmetry, that is, those raindrops flattened more on the bottom than on the top. However, (25) and (26) served as a useful check on the program in the calculations for spheroidal raindrops with $\alpha = \pi/2$.

We describe in Section V how we obtain approximate values of (a finite number of) the coefficients a_{mn}, b_{mn}, c_{mn}, and d_{mn}, but we now turn to the quantities of physical interest. We consider only the far scattered field, so that $k_0 r \gg 1$. Thus, we restrict our attention to the leading term in the asymptotic expansion of the spherical Bessel function of the third kind, as given by (12). Also, it follows that

$$h_n^{(1)'}(k_0 r) \sim \frac{(-i)^n}{k_0 r} e^{ik_0 r}. \tag{27}$$

Then, from (8) to (11), it is found that

$$k_0 r e^{-ik_0 r}\mathbf{E}^s \sim \sum_{m=-\infty}^{\infty} \sum_{\substack{n \geqq |m| \\ n \neq 0}} (-i)^{n+1} \left\{ a_{mn} \left[\frac{dP_n^{|m|}(\cos\theta)}{d\theta} \mathbf{i}_3 - \frac{im}{\sin\theta} P_n^{|m|}(\cos\theta)\mathbf{i}_2 \right] - ib_{mn} \left[\frac{dP_n^{|m|}(\cos\theta)}{d\theta} \mathbf{i}_2 + \frac{im}{\sin\theta} P_n^{|m|}(\cos\theta)\mathbf{i}_3 \right] \right\} e^{im\varphi} \tag{28}$$

and

$$\omega\mu_0 \mathbf{H}^s \sim k_0 \mathbf{i}_1 \times \mathbf{E}^s. \tag{29}$$

Of particular interest are the scattered fields in the forward direction, corresponding to $\theta = \alpha$, $\varphi = 0$, for which, from (76),

$$(\cos\alpha\mathbf{i} - \sin\alpha\mathbf{k}) = \mathbf{i}_2, \qquad \mathbf{j} = \mathbf{i}_3. \tag{30}$$

From (5), (6), (23), (24), and (28) to (30), it follows that the far scattered field in the forward direction has the same polarization as the incident wave for either polarization. The forward scattering amplitudes are[3]

$$S_{\mathrm{I}}(0) = \frac{1}{E_{\mathrm{I}}} (\cos\alpha\mathbf{i} - \sin\alpha\mathbf{k}) \cdot \lim_{r\to\infty} \{-ik_0 r e^{-ik_0 r}\mathbf{E}_{\mathrm{I}}^s|_{\theta=\alpha,\ \varphi=0}\} \tag{31}$$

and

$$S_{\mathrm{II}}(0) = \frac{1}{E_{\mathrm{II}}} \mathbf{j} \cdot \lim_{r\to\infty} \{-ik_0 r e^{-ik_0 r}\mathbf{E}_{\mathrm{II}}^s|_{\theta=\alpha,\ \varphi=0}\}. \tag{32}$$

Thus, for the first polarization of the incident wave,

$$E_{\mathrm{I}}S_{\mathrm{I}}(0) = \sum_{m=-\infty}^{\infty} \sum_{\substack{n \geqq |m| \\ n \neq 0}} (-i)^{n-1} \times \left[a_{mn}^{\mathrm{I}} \cdot \frac{m}{\sin \alpha} P_n^{|m|}(\cos \alpha) + b_{mn}^{\mathrm{I}} \frac{dP_n^{|m|}(\cos \alpha)}{d\alpha} \right] \quad (33)$$

and for the second polarization,

$$E_{\mathrm{II}}S_{\mathrm{II}}(0) = \sum_{m=-\infty}^{\infty} \sum_{\substack{n \geqq |m| \\ n \neq 0}} (-i)^{n+2} \times \left[a_{mn}^{\mathrm{II}} \frac{dP_n^{|m|}(\cos \alpha)}{d\alpha} + b_{mn}^{\mathrm{II}} \cdot \frac{m}{\sin \alpha} P_n^{|m|}(\cos \alpha) \right]. \quad (34)$$

The energy scattered by the raindrop is[15]

$$W_s = \frac{1}{2} \operatorname{Re} \int_0^{2\pi} \int_0^{\pi} [E_2^s (H_3^s)^* - E_3^s (H_2^s)^*] r^2 \sin \theta d\theta d\varphi, \quad (35)$$

where the asterisk denotes complex conjugate. The calculation of W_s, using the asymptotic form of the scattered fields given by (28) and (29) and letting $r \to \infty$, is outlined in Appendix C. It is found that

$$W_s = \frac{2\pi}{\omega \mu_0 k_0} \sum_{m=-\infty}^{\infty} \sum_{n \geqq |m|} \frac{n(n+1)(n+|m|)!}{(2n+1)(n-|m|)!} (|a_{mn}|^2 + |b_{mn}|^2). \quad (36)$$

The scattering cross section Q_s is defined as the ratio of the scattered energy flow to the mean energy flow of the incident wave per unit area. Thus,[15]

$$Q_s^{\mathrm{I}} = \frac{2\omega\mu_0 W_s^{\mathrm{I}}}{k_0 E_{\mathrm{I}} E_{\mathrm{I}}^*}, \qquad Q_s^{\mathrm{II}} = \frac{2\omega\mu_0 W_s^{\mathrm{II}}}{k_0 E_{\mathrm{II}} E_{\mathrm{II}}^*}. \quad (37)$$

The total (extinction) cross section is the sum of the scattering and absorption cross sections, so that

$$Q_t^{\mathrm{I}} = Q_s^{\mathrm{I}} + Q_a^{\mathrm{I}}, \qquad Q_t^{\mathrm{II}} = Q_s^{\mathrm{II}} + Q_a^{\mathrm{II}}. \quad (38)$$

(We note that van de Hulst[16] uses the notations C_{ext}, C_{sca}, and C_{abs} for Q_t, Q_s, and Q_a, respectively.) It is "known"[17] that

$$Q_t^{\mathrm{I}} = \frac{4\pi}{k_0^2} \operatorname{Re} S_{\mathrm{I}}(0), \qquad Q_t^{\mathrm{II}} = \frac{4\pi}{k_0^2} \operatorname{Re} S_{\mathrm{II}}(0), \quad (39)$$

so that (38) may be used to determine the absorption cross sections Q_a^{I} and Q_a^{II}. The relations (39) which are consistent with the optical

theorem may be verified directly from the relations

$$Q_t^{\mathrm{I}} = \frac{2\omega\mu_0 W_t^{\mathrm{I}}}{k_0 E_{\mathrm{I}} E_{\mathrm{I}}^*}, \qquad Q_t^{\mathrm{II}} = \frac{2\omega\mu_0 W_t^{\mathrm{II}}}{k_0 E_{\mathrm{II}} E_{\mathrm{II}}^*}, \tag{40}$$

and the expression for the total energy[15]

$$W_t = \frac{1}{2}\,\mathrm{Re}\int_0^{2\pi}\int_0^{\pi} [E_3^i(H_2^s)^* + E_3^s(H^i)^* - E_2^i(H_3^s)^* - E_2^s(H_3^i)^*]r^2 \sin\theta d\theta d\varphi, \tag{41}$$

and a few of the details are given in Appendix C.

Let us now consider an (in general) elliptically polarized incident wave that is the sum of the two linearly polarized incident waves under consideration; i.e.,

$$\mathbf{E}^i = \mathbf{E}_{\mathrm{I}}^i + \mathbf{E}_{\mathrm{II}}^i \tag{42}$$

Then the scattered electric field is

$$\mathbf{E}^s = \mathbf{E}_{\mathrm{I}}^s + \mathbf{E}_{\mathrm{II}}^s, \tag{43}$$

and, as shown in Appendix C,

$$Q_s = \frac{(E_{\mathrm{I}}E_{\mathrm{I}}^* Q_s^{\mathrm{I}} + E_{\mathrm{II}}E_{\mathrm{II}}^* Q_s^{\mathrm{II}})}{(E_{\mathrm{I}}E_{\mathrm{I}}^* + E_{\mathrm{II}}E_{\mathrm{II}}^*)} \tag{44}$$

and

$$Q_t = \frac{(E_{\mathrm{I}}E_{\mathrm{I}}^* Q_t^{\mathrm{I}} + E_{\mathrm{II}}E_{\mathrm{II}}^* Q_t^{\mathrm{II}})}{(E_{\mathrm{I}}E_{\mathrm{I}}^* + E_{\mathrm{II}}E_{\mathrm{II}}^*)}. \tag{45}$$

Since for polarizations I and II the far scattered field in the forward direction has the same polarization as the incident wave, it follows from (31), (32), and (43) that the far scattered field in the forward direction for the elliptically polarized incident wave is given by

$$\mathbf{E}^s|_{\theta=\alpha,\ \varphi=0} \sim \frac{ie^{ik_0 r}}{k_0 r}[E_{\mathrm{I}}S_{\mathrm{I}}(0)(\cos\alpha\mathbf{i} - \sin\alpha\mathbf{k}) + E_{\mathrm{II}}S_{\mathrm{II}}(0)\mathbf{j}]. \tag{46}$$

Thus, from (39) and (44) to (46), it suffices to calculate $S_{\mathrm{I}}(0)$, $S_{\mathrm{II}}(0)$, Q_S^{I}, and Q_S^{II}. The relation between the polarizations of the incident field and the far scattered field in the forward direction may be determined from (42) and (46), using (5) and (6).

IV. FIRST-ORDER PERTURBATION THEORY

Oguchi considered spheroidal raindrops with small eccentricity and carried out a perturbation expansion originally determining the first-

order approximation[4] and later the second-order one.[18] We have calculated the first-order approximation for axisymmetric raindrops that are nearly spherical, so that the surface of the raindrop is given by $r = R(\theta)$, $0 \leqq \theta \leqq \pi$, where

$$R(\theta) = a[1 + \nu\sigma_1(\theta) + \cdots], \qquad |\nu| \ll 1. \tag{47}$$

Our derivation follows closely the one given by Oguchi.[4] Since the calculations are somewhat lengthy and involved, we merely outline the procedure, state the results, and point out some simplifications that may be made in the expressions given by Oguchi.

The incident wave may be expanded in terms of spherical vector wave functions,[4,19] and the expansions are given by eqs. (116) and (117) in Appendix D. These expansions are consistent with those given by Oguchi, but the reader should bear in mind that, in addition to using the even and odd spherical vector wave functions, Oguchi has assumed the time factor $e^{+i\omega t}$, and his waves propagate in the opposite direction to ours. Corresponding to (47), the coefficients in the expansions (10), (11), (13), and (14) are expanded in the form

$$a_{mn} = a_{mn}^{(0)} + \nu a_{mn}^{(1)} + \cdots, \quad b_{mn} = b_{mn}^{(0)} + \nu b_{mn}^{(1)} + \cdots, \tag{48}$$

$$c_{mn} = c_{mn}^{(0)} + \nu c_{mn}^{(1)} + \cdots, \quad d_{mn} = d_{mn}^{(0)} + \nu d_{mn}^{(1)} + \cdots. \tag{49}$$

Appendix D indicates how these coefficients may be determined from the boundary conditions (81) to (84).

The zero-order approximation, with $\nu = 0$ in (47), corresponds to a spherical raindrop of radius a. We have, for $n \geqq |m|$ and $n \neq 0$,

$$a_{mn}^{(0)} = \alpha_{mn} a_n, \qquad b_{mn}^{(0)} = \beta_{mn} b_n \tag{50}$$

and

$$c_{mn}^{(0)} = \alpha_{mn} c_n, \qquad d_{mn}^{(0)} = \beta_{mn} d_n, \tag{51}$$

where

$$\frac{\alpha_{mn}^{\mathrm{I}}}{E_{\mathrm{I}}} = \frac{-i^{n+1}(2n+1)(n-|m|)!}{n(n+1)(n+|m|)!} \frac{m}{\sin\alpha} P_n^{|m|}(\cos\alpha) = \frac{i\beta_{mn}^{\mathrm{II}}}{E_{\mathrm{II}}}, \tag{52}$$

$$\frac{\beta_{mn}^{\mathrm{I}}}{E_{\mathrm{I}}} = \frac{-i^{n+1}(2n+1)(n-|m|)!}{n(n+1)(n+|m|)!} \frac{dP_n^{|m|}(\cos\alpha)}{d\alpha} = \frac{i\alpha_{mn}^{\mathrm{II}}}{E_{\mathrm{II}}}, \tag{53}$$

and expressions for the quantities a_n, b_n, c_n, and d_n (which do not depend on the polarization) are given by eqs. (119) to (122) in Appendix D, where $\rho = k_0 a$ and the functions $F_n(\xi)$ and $G_n(\xi)$ are defined in (118). For $\alpha = 0$, the coefficients vanish unless $|m| = 1$, and the well-known Mie solution[6] is recovered.

The first-order corrections to the coefficients are given by

$$a_{mn}^{(1)} = j_n(N\rho)X_{mn}, \qquad c_{mn}^{(1)} = h_n^{(1)}(\rho)X_{mn}, \tag{54}$$

$$b_{mn}^{(1)} = G_n(N\rho)Y_{mn} + j_n(N\rho)Z_{mn}, \tag{55}$$

and

$$d_{mn}^{(1)} = F_n(\rho)Y_{mn} + \frac{1}{N}h_n^{(1)}(\rho)Z_{mn}, \tag{56}$$

where

$$X_{mn} = (1 - N^2)\rho^3 c_n \sum_{\substack{l \geq |m| \\ l \neq 0}} [d_{ml}^{(0)} G_l(N\rho)J_{nl}^m + ic_{ml}^{(0)} j_l(N\rho)I_{nl}^m], \tag{57}$$

$$Y_{mn} = (N^2 - 1)\rho^3 d_n \sum_{\substack{l \geq |m| \\ l \neq 0}} [c_{ml}^{(0)} j_l(N\rho)J_{nl}^m - id_{ml}^{(0)} G_l(N\rho)I_{nl}^m], \tag{58}$$

and

$$Z_{mn} = -i(N^2 - 1)\rho d_n \sum_{\substack{l \geq |m| \\ l \neq 0}} d_{ml}^{(0)} j_l(N\rho)H_{nl}^m. \tag{59}$$

The quantities H_{nl}^m, I_{nl}^m, and J_{nl}^m in (57) to (59) involve integrals over the perturbation of the raindrop surface from the sphere. Specifically,

$$\frac{2(n + |m|)!}{(2n + 1)(n - |m|)!} H_{nl}^m = \mathfrak{IC}_{nl}^m$$

$$\equiv l(l + 1)\int_0^\pi P_l^{|m|}(\cos\theta)P_n^{|m|}(\cos\theta)\sin\theta\sigma_1(\theta)d\theta, \tag{60}$$

$$\frac{2n(n + 1)(n + |m|)!}{(2n + 1)(n - |m|)!} I_{nl}^m = \mathfrak{g}_{nl}^m$$

$$\equiv \int_0^\pi \left[\frac{dP_l^{|m|}(\cos\theta)}{d\theta}\frac{dP_n^{|m|}(\cos\theta)}{d\theta} + \frac{m^2}{\sin^2\theta}P_l^{|m|}(\cos\theta)P^{|m|}(\cos\theta)\right]\sin\theta\sigma_1(\theta)d\theta, \tag{61}$$

and

$$\frac{2n(n + 1)(n + |m|)!}{(2n + 1)(n - |m|)!} J_{nl}^m = \mathfrak{J}_{nl}^m$$

$$\equiv m\int_0^\pi \left[P_l^{|m|}(\cos\theta)\frac{dP_n^{|m|}(\cos\theta)}{d\theta} + \frac{dP_l^{|m|}(\cos\theta)}{d\theta}P_n^{|m|}(\cos\theta)\right]\sigma_1(\theta)d\theta. \tag{62}$$

The above results were obtained after considerable algebra and after using the simplifications given in eqs. (125) to (131) in Appendix

D. The expressions in (54) to (56) hold for both polarizations of the incident wave, and the only quantities therein that depend on the polarization are the zero-order coefficients $c_{ml}^{(0)}$ and $d_{ml}^{(0)}$, which enter into the expressions given in (57) to (59) and are given by (51) to (53). In general, there are infinitely many terms in the sums in (57) to (59), but in particular cases there are only a finite number of terms.

Thus, for a spheroidal raindrop with

$$R(\theta) = a(1 - \nu \sin^2 \theta)^{-\frac{1}{2}} = a(1 + \tfrac{1}{2}\nu \sin^2 \theta + \cdots), \tag{63}$$

we have $\sigma_1(\theta) = \frac{1}{2} \sin^2 \theta$, from (47). The integrals in (60) to (62) may be evaluated explicitly, and it is found that H_{nl}^m and I_{nl}^m vanish unless $l = n, n + 2$, or $n - 2$, and J_{nl}^m vanishes unless $l = n - 1$ or $n + 1$. The explicit expressions for these quantities are given by eqs. (137), (139), and (142) in Appendix E, in which δ_{ln} denotes the Kronecker delta, i.e., $\delta_{ln} = 1$ for $l = n$, and 0 otherwise. We have verified that our results for the spheroid are consistent with those of Oguchi,[4] provided that simplifications corresponding to those in eqs. (123) and (127) to (130) are made in his expressions, and due allowance is made for the differences in notation. We remark that similar simplifications may be made in Oguchi's expressions even in the case in which the permeability of the spheroid differs from the free space value.

As is seen later, it is advantageous to obtain the first-order approximation for a spheroidal raindrop by perturbing about the equivolumic sphere, rather than the inscribed sphere as Oguchi[4] did. If $\bar{a}$ is the radius (in centimeters) of the equivolumic sphere, then, from (1),

$$a = \bar{a}(1 - \bar{a})^{\frac{1}{3}}, \qquad \nu = \bar{a}(2 - \bar{a}). \tag{64}$$

Hence, from (63),

$$\begin{aligned} R(\theta) &= \bar{a}[1 + 2\bar{a}(\tfrac{1}{2} \sin^2 \theta - \tfrac{1}{3}) + 0(\bar{a}^2)] \\ &= \bar{a}[1 + \nu(\tfrac{1}{2} \sin^2 \theta - \tfrac{1}{3}) + 0(\nu^2)]. \end{aligned} \tag{65}$$

We must now replace ρ by $\bar{\rho} = k_0\bar{a}$ and add terms to the expressions in (60) to (62) corresponding to $\bar{\sigma}_1(\theta) = -\frac{1}{3}$. It is readily found, using the orthogonality relation for the Legendre functions[14] and equations (102) and (103), that these additional terms correspond to

$$\tilde{H}_{nl}^m = -\tfrac{1}{3}n(n + 1)\delta_{ln}, \quad \tilde{I}_{nl}^m = -\tfrac{1}{3}\delta_{ln}, \quad \tilde{J}_{nl}^m = 0. \tag{66}$$

We also remark that the use of the perturbation parameter $\bar{\nu} = 2\bar{a}$, rather than ν as given by (64), generally gives better results for the larger drop sizes.

V. LEAST-SQUARES-FITTING PROCEDURE

We now discuss the calculation of an approximate nonperturbative solution of the scattering problem. As mentioned in Section III, it is sufficient to determine the unknown coefficients for nonnegative values of m and then to use the relationships in (23) or (24). For $m = 0, 1, 2, \cdots$, the boundary conditions in (81) to (84) take the form

$$K_{mq}(\theta) - \sum_{\substack{n \geqq m \\ n \neq 0}} [a_{mn}A_{mnq}(\theta) + b_{mn}B_{mnq}(\theta) + c_{mn}C_{mnq}(\theta) + d_{mn}D_{mnq}(\theta)] = 0. \quad (67)$$

for $q = 1, 2, 3, 4$ and $0 \leqq \theta \leqq \pi$, where

$$K_{m1}(\theta) = e_{m3}(R(\theta), \theta), \qquad K_{m2}(\theta) = \frac{i\omega\mu_0}{k_0} h_{m3}(R(\theta), \theta), \quad (68)$$

$$K_{m3}(\theta) = e_{m2}(R(\theta), \theta) + \frac{1}{R(\theta)} \frac{dR}{d\theta} e_{m1}(R(\theta), \theta), \quad (69)$$

and

$$K_{m4}(\theta) = \frac{i\omega\mu_0}{k_0} \left[h_{m2}(R(\theta), \theta) + \frac{1}{R(\theta)} \frac{dR}{d\theta} h_{m1}(R(\theta), \theta) \right]. \quad (70)$$

The function $R(\theta)$ describes the shape of the raindrop. The functions $e_{mj} = \mathbf{e}_m \cdot \mathbf{i}_j$ and $h_{mj} = \mathbf{h}_m \cdot \mathbf{i}_j$ are given by (21) or (22), depending on the polarization of the incident wave, where expressions for $\mathbf{f}_m(r, \theta)$ and $\mathbf{g}_m(r, \theta)$ are given by (79) and (80). The functions $A_{mnq}(\theta)$, $B_{mnq}(\theta)$, $C_{mnq}(\theta)$, $D_{mnq}(\theta)$, which do not depend on the polarization, involve the spherical Bessel functions of the first and third kinds and the associated Legendre functions and the derivatives of each of these functions. In view of (4), the argument of the spherical Bessel functions of the first kind is complex.

For each m there are infinitely many unknown coefficients a_{mn}, b_{mn}, c_{mn}, and d_{mn}. To obtain an approximate solution, only a finite number of coefficients is considered. One procedure is to truncate the sum in (67) at $n = N_0$, say, and then to satisfy the boundary conditions at the points $\theta = \theta_{lm}$, $l = 1, \cdots, (N_0 - m + 1 - \delta_{m0})$, which are appropriately selected, e.g., uniformly spaced in the interval 0 to π. This was the procedure adopted by Oguchi,[5] and it leads to a system of simultaneous linear equations for the coefficients. We refer to this procedure, in which the total number of fitting points is equal to the number of unknown coefficients, as collocation.

The method of collocation was used by Mullin et al.[20] for the much simpler two-dimensional scalar problem of scattering by a perfectly

conducting cylinder of smooth contour, which is not a gross perturbation from the circular. In this problem, there is only one set of unknown coefficients to be determined, namely, that occurring in the expansion of the scattered field. Mullin et al. checked the results for the circular cylinder obtained by collocation with the known analytical results and also considered elliptic cylinders (with ratio of minor to major axis of $\frac{2}{3}$, in particular). Before tackling the raindrop problem, we considered the same problems as Mullin et al., but combined point matching with least-squares fitting.

Thus, instead of using collocation, we satisfied the (single) boundary condition in a least-squares sense at a larger number of points than the number of unknown coefficients in the truncated expansion of the scattered field. We found that a significant improvement could be obtained in the overall fit of the boundary condition, although the far field quantities were not affected as significantly. This is because the higher-order coefficients are more significant on the boundary than in the far field. However, the accuracy of the lower-order coefficients is affected by the goodness of fit of the boundary condition. With collocation, there were much larger errors in the boundary condition (in between the fitting points) than with least-squares fitting with a sufficiently large number of points.

Since the fit of the boundary condition for the elliptic cylinder becomes poorer with increasing eccentricity, we considered it desirable to use least-squares fitting rather than collocation for the raindrop problem. Thus, in order to approximately satisfy the boundary conditions (67), we minimized the quantities

$$\Delta_m \equiv \sum_{q=1}^{4} w_{mq} \sum_{l=1}^{\lambda_m} \Big| K_{mq}(\theta_{lm}) - \sum_{\substack{n=m \\ n\neq 0}}^{N_m} [a_{mn}A_{mnq}(\theta_{lm}) + b_{mn}B_{mnq}(\theta_{lm}) + c_{mn}C_{mnq}(\theta_{lm}) + d_{mn}D_{mnq}(\theta_{lm})] \Big|^2 \quad (71)$$

for each $m = 0, \cdots, M$, with respect to the (complex) coefficients a_{mn}, b_{mn}, c_{mn}, and d_{mn}, where $w_{mq} > 0$ are appropriate weights and θ_{lm} are appropriate points in the interval 0 to π. It is assumed that

$$\lambda_m \geqq N_m - m + 1 - \delta_{m0}, \quad (72)$$

so that the total number of fitting points is not less than the number of unknown coefficients to be determined. In the case of equality in (72), least-squares fitting is equivalent to collocation.

The programs for carrying out least-squares fitting and for calculating the special functions occurring in the functions in (71) with argu-

ment θ_{lm} are described in the next section. Actually, more flexibility was built into the least-squares-fitting program, allowing for truncation of the sums in (67) at different limits for each of the coefficients a_{mn}, b_{mn}, c_{mn}, and d_{mn}, and for λ_m and θ_{lm} in (71) to depend on q, so that each of the four boundary conditions could be fit at different points, and in particular at a different number of them. It was anticipated that the least-squares-fit subroutine might become overloaded, in which case it would be desirable to hold the number of coefficients to a minimum. It turned out, however, that the subroutine was able to handle almost 100 (complex) coefficients without difficulty. Similarly, it might be desirable to keep the total number of fitting points to a minimum, and hence to use fewer fitting points for those of the four boundary conditions that are easier to fit. Again, it was not found necessary to do this for the calculations carried out so far.

For the calculations of this paper we took the weights to be independent of m and q, i.e., $w_{mq} \equiv 1$, since it was generally found that the difference was tolerable between the magnitudes of the maximum error in the fit of each of the four boundary conditions. We at first considered factoring out $(\sin \theta)^{m-1}$, for $m \geqq 2$, from the boundary conditions (67), but decided against it since we felt that the absolute, rather than the relative, error in the fit of the boundary conditions was important. However, because of the presence of this factor, we did experiment with unequally spaced fitting points which were closer together in the neighborhood of $\pi/2$. We decided that equally spaced fitting points would suffice, provided that enough were used. The total number of fitting points was usually taken to be slightly more than twice the number of unknown coefficients, i.e., $\lambda_m > 2(N_m - m + 1 - \delta_{m0})$.

Generally, N_m, the upper limit of n in (71), was taken to be independent of m, i.e., $N_m \equiv N_0$, $m = 0, \cdots, M$. The choice of N_0 and M depended both on drop size and on frequency. The choice of M was based on the rate of convergence of the outer sums in the expressions in (33), (34), and (36) for the far field quantities. On the other hand, to ensure the accuracy of the lower-order terms in the inner sums, it is necessary to take more terms in n than are really needed in the calculation of the far field quantities. A convergence test was carried out by doing the calculations for $N_m = \hat{N}_0$, $(\hat{N}_0 + 2)$ and $(\hat{N}_0 + 4)$.

VI. NUMERICAL ROUTINES

The program to compute the complex coefficients a_{mn}, b_{mn}, c_{mn}, d_{mn}, the scattering cross section Q_s, and the forward scattering amplitude

$S(0)$ for the two polarizations of the incident wave is written in Fortran IV for a Honeywell 6070 computer. It uses the complex arithmetic and math routines (such as sin, cos) written for that system. The program is written as a three-part package; the first part consists of a driver routine which sets up core storage for the least-squares matrix and associated vectors and the following subroutines:

L2FIT—The main subroutine which computes the elements of the complex matrix for input to the least-squares-fitting procedure and controls the other subroutines.

CLSTSQ—Computes a least-squares fit for a linear system with complex coefficients; the algorithm and Fortran routine were written by P. Businger of Bell Laboratories.

BJYNC—Computes the Bessel functions $J_n(z)$, $Y_n(z)$, for z complex, n a nonnegative integer; the algorithm and Fortran subroutine package were written by E. Sonnenblick of Bell Laboratories.

SBES—Computes the spherical Bessel functions $j_n(x)$, $y_n(x)$, x real, n a nonnegative integer.

CSB—Computes the spherical Bessel function $j_n(z)$, z complex, n a nonnegative integer.

SLEG—Computes the associated Legendre functions $P_n^m(\cos\theta)$, m, n nonnegative integers.

The second part of the package is the routine

SQS—Computes the forward scattering amplitude $S(0)$ and the scattering and total cross sections Q_s, Q_t for both polarizations from the least-squares-fit solutions.

The third part is a computational check on the least-squares fit. It consists of a driver routine as in the first part, the function subroutines BJYNC, SBES, CBS, SLEG, and the main subroutine

CHECK—Checks the accuracy of the least-squares computation of a_{mn}, b_{mn}, c_{mn}, d_{mn} by using these coefficients to compute the boundary fit at points in addition to those used to obtain the coefficients.

The internal computations of all the subroutines except CSB (see detailed description below) are done in double-precision arithmetic; on the Honeywell 6070 this means 18 digits are used for all computations. The function values (Bessel, spherical Bessel, Legendre), how-

ever, are returned as single-precision numbers (8 digits), since the accuracy of any more digits could not always be guaranteed.

The main subroutine, L2FIT, sets up the complex matrix to minimize the quantities (71). Instead of the limit N_m in (71), the program actually breaks the summation on n into four parts, using limits α_m, β_m, γ_m, δ_m for the coefficients a_{mn}, b_{mn}, c_{mn}, d_{mn}, respectively; further, it replaces the limit λ_m in the sum on l with four limits, λ_{mq}. Thus, for each $m = 0, 1, \cdots, M$ the matrix equation to be minimized takes the form $\|\mathbf{A}\cdot\mathbf{x} - \mathbf{b}\| \approx 0$, where $\mathbf{A}$ is an L-by-N matrix with L, N, which are both dependent on m, defined as follows:

$$L = \sum_{q=1}^{4} \lambda_{mq}$$

and

$$N = \alpha_m + \beta_m + \gamma_m + \delta_m - 4(m - 1 + \delta_{m0}).$$

Although the basic functions (Bessel, Legendre, and derivatives of these) are returned to L2FIT in single precision, the calculations of the elements A_{mnq}, B_{mnq}, C_{mnq}, D_{mnq} in the least-squares matrix and K_{mq} in the vector of constants, $\mathbf{b}$, are carried out and left in double precision for input to the least-squares-minimization program. To facilitate changing the raindrop shape and spacing of points on the boundary, the quantities θ_{lm} and $R(\theta_{lm})$ are computed in subroutines called by this routine.

The routine CLSTSQ uses elementary Hermitian (or Householder) transformations to compute a linear least-squares solution to the equation $\|\mathbf{A}\cdot\mathbf{x} - \mathbf{b}\| = \min$. The algorithm is an adaptation of an algorithm for a real matrix written by P. Businger and G. H. Golub.[21]

The routine CHECK uses the coefficients a_{mn}, b_{mn}, c_{mn}, d_{mn} from CLSTSQ as input into the expressions in (67) to compute the fit of the boundary condition in between the fitting points as well as at the fitting points. The goodness of this fit provides a check on the accuracy of the computed coefficients.

The computation of the elements for the least-squares matrix and constant vector requires values of $J_n(x)$, $j_n(x)$, $y_n(x)$, $j_n(z)$, $P_n^m(\cos\theta)$, where x and θ are real, z is complex, and n and m are nonnegative integers. The routine to compute $J_n(x)$, BJYNC[22] uses a downward recursion scheme (compute J_N, J_{N-1}, $\cdots$, J_0) for $|x| > 0.1$ and uses the power series expansion of $J_n(x)$ for $|x| \leqq 0.1$. Comparison of the

results of this routine with tables in Abramowitz and Stegun[23] for x values ranging from 0 to 5 yielded complete agreement in all cases.

The real spherical Bessel functions, $j_n(x)$ and $y_n(x)$, are computed recursively in the routine SBES using the algorithm of D. S. Drumheller,[24] an improved version of Miller's algorithm.

Miller's algorithm for $j_n(x)$ is: Let $g_{N+1}(x) \equiv 0$, $g_N(x) = 10^{-20}$ ⟨some small fixed number⟩; generate $g_{N-1}(x), \cdots, g_0(x)$ from the recurrence relations, $g_{n-1}(x) = (2n+1)x^{-1}g_n(x) - g_{n+1}(x)$, satisfied by the spherical Bessel functions;[25] compute $j_0(x) = x^{-1}\sin x$; normalize $j_l(x) = g_l(x)\cdot\dfrac{j_0(x)}{g_0(x)}$, $l = 0, 1, \cdots, N$.

Drumheller's algorithm generates ascending orders of $y_n(x)$ recursively, starting from Rayleigh's formulas[25] for $y_0(x)$, $y_1(x)$ up to some order N, where N is strictly limited only by the relation

$$y_N(x) \leqq \max - \text{the largest number the computer can handle (for the Honeywell 6070, max} \approx 10^{38}).$$

Letting

$$f_N(x) \equiv 0, \qquad f_{N-1}(x) = -(x^2 y_N(x))^{-1},$$

the algorithm then generates $f_{N-2}(x), \cdots, f_0(x)$ recursively, using the recurrence relations satisfied by the spherical Bessel functions. Although, as Drumheller points out, $f_0(x) = j_0(x)$ to some degree of precision (determined to a large extent by N), to ensure exactness in the lower orders of $j_n(x)$ and to shift any error to the higher-order, smaller-magnitude terms, we calculate $j_0(x)$ exactly and normalize $j_1(x), \cdots, j_N(x)$ as in Miller's algorithm. We compared these results to tables in Abramowitz and Stegun[26] and in the U. S. Math Tables Project[27] for the values of n and the range of x used in the least-squares fitting, and the agreement was excellent.

The complex spherical Bessel function, $j_n(z)$, is computed in the routine CSB, using an algorithm designed by A. E. Kaplan,[28] since Drumheller's (or Miller's) recursive algorithm yields inaccurate results for complex arguments with a significant imaginary part. Kaplan uses a Taylor series expansion to compute $j_N(z)$, $j_{N-1}(z)$, with $N \approx |z|^2$ for best results, then uses the backward recursion and normalization techniques discussed above to generate $j_{N-2}(z), \cdots, j_0(z)$. The use of the Taylor series for "large" complex arguments produces better starting values and, therefore, more accurate recursion results than either Drumheller's or Miller's algorithm. A "large" complex argument in

this case is one such that $|z| \geqq 9$; for $|z| < 9$, we use Drumheller's algorithm directly. In this routine, complex arithmetic is used for all internal computations; thus, since the Honeywell 6070 does not have double-precision complex arithmetic, all computations are in single precision. The accuracy of the results of this routine was checked by the following comparisons:

(*i*) For z real, they were compared to the spherical Bessel functions in Abramowitz and Stegun[26] and to results from SBES.

(*ii*) For z pure imaginary, they were compared (multiplied by appropriate factors) to the modified spherical Bessel functions of the first kind in Abramowitz and Stegun.[29]

(*iii*) For z any complex number, they were compared to Rayleigh's formulas[25] of order 0, 1, 2 (a straight computation of Rayleigh's formulas produces inaccurate values for higher orders).

For all values of z (from $|z| = 0$ to $|z| = 50$) and for order n as large as we could compute (or as large as we could compare to in tables or formulas), this routine produced answers agreeing in six to eight decimal places with the other results.

The associated Legendre function $P_n^m(\cos\theta)$ is computed directly from its series expansion, in powers of sines or cosines, as given by L. Robin.[30] It should be noted here that we use the following definition for $P_n^m(\cos\theta)$,

$$P_n^m(\cos\theta) = (-1)^m \sin^m\theta \frac{d^m P_n(\cos\theta)}{d(\cos\theta)^m},$$

whereas Stratton[31] omits the factor $(-1)^m$. Comparison of the results of this routine to explicit formulas for $m \leqq 4$, $n \leqq 7$ yielded eight places of agreement. Further checks of this routine against tables given by S. L. Belousov[32] and tables in the U. S. Math Tables Project[33] were done by S. Hoffberg for the values of m and n used in the least-squares fitting; her results also found complete agreement in all cases.

In the scattering problem, the matrix and vector sizes, as well as the highest order needed for the functions, depend on drop size and frequency; the sizes required by these parameters are discussed in the next section. Here, we give approximate running times for each of the three parts of the package and give some feeling for the correlation of the least-squares matrix size and the limit max m with the overall core storage and run time in the first part. In (71), we generally took $N_m \equiv N_0$, and λ_m dependent upon N_0 and decreasing with m (for $m \geqq 1$). Then the largest matrix size occurs when $m = 0$, and is thus a function

of N_0 alone. Tabulated below are some typical storage and run time figures for the least-squares fit.

max m	N_0	Largest Matrix Size	Approximate Storage	Approximate Run Time (hours)
6	13, 15, 17	164 × 68	70 K	0.13
7	15, 17, 19	180 × 76	80 K	0.2
8	19, 21, 23	212 × 92	103 K	0.39

In each of the above cases, we computed a set of coefficients a_{mn}, b_{mn}, c_{mn}, d_{mn}, $n = m, \cdots, N_0$ $(n \neq 0)$, for $m = 0, 1, \cdots,$ max m, and for each of the three values of N_0.

The second and third parts require much less storage because neither requires a large storage matrix. The total core requirement to run SQS is 12 K; it computes the quantities $S(0)$, Q_s, Q_t in typically less than 1 second. The third part uses 35 K to do the calculations for 428 rows and 92 columns (more rows are needed because the boundary fit is checked at θ values in addition to those used to obtain the coefficients); to check the L2FIT results for $N_0 = 23$ required approximately 0.05 hours.

As a final note, we save the coefficients computed from L2FIT on magnetic tape. At first, all coefficients were written on tape and the second and third parts used the tape as input; this proved very inefficient, due in part to the high cost of tape usage and in part to the fact that we were saving all data generated. We switched to writing the data from each run of L2FIT onto a high-speed disc file, using this as input to the other two parts; this change resulted in a noticeable cost reduction and allowed us to permanently save only the best data.

Table I — Raindrop parameters for different drop sizes

$\bar{a}$(cm)	a(cm)	ν
0.025	0.02458158	0.049375
0.05	0.04831913	0.0975
0.075	0.07120149	0.144375
0.1	0.09321698	0.19
0.125	0.11435330	0.234375
0.15	0.13459757	0.2775
0.175	0.15393617	0.319375
0.2	0.17235477	0.36
0.225	0.18983822	0.399375
0.25	0.20637045	0.4375
0.275	0.22193444	0.474375
0.3	0.23651206	0.51
0.325	0.25008398	0.544375
0.35	0.26262956	0.5775

Table II — Forward scattering amplitudes at 4 GHz with $\alpha = 90°$ for different drop sizes

$\bar{a}$(cm)	$S_{\mathrm{I}}(0)$	$S_{\mathrm{II}}(0)$
0.025	$6.9215 \times 10^{-8} - 8.6909 \times 10^{-6}i$	$7.3309 \times 10^{-8} - 8.9487 \times 10^{-6}i$
0.05	$5.8893 \times 10^{-7} - 6.8473 \times 10^{-5}i$	$6.5803 \times 10^{-7} - 7.2647 \times 10^{-5}i$
0.075	$2.2523 \times 10^{-6} - 2.2822 \times 10^{-4}i$	$2.6370 \times 10^{-6} - 2.4970 \times 10^{-4}i$
0.1	$6.3705 \times 10^{-6} - 5.3582 \times 10^{-4}i$	$7.7684 \times 10^{-6} - 6.0510 \times 10^{-4}i$
0.125	$1.5414 \times 10^{-5} - 1.0399 \times 10^{-3}i$	$1.9518 \times 10^{-5} - 1.2134 \times 10^{-3}i$
0.15	$3.3841 \times 10^{-5} - 1.7918 \times 10^{-3}i$	$4.4527 \times 10^{-5} - 2.1630 \times 10^{-3}i$
0.175	$6.9433 \times 10^{-5} - 2.8484 \times 10^{-3}i$	$9.5324 \times 10^{-5} - 3.5628 \times 10^{-3}i$
0.2	$1.3555 \times 10^{-4} - 4.276 \times 10^{-3}i$	$1.9565 \times 10^{-4} - 5.552 \times 10^{-3}i$
0.225	$2.551 \times 10^{-4} - 6.154 \times 10^{-3}i$	$3.916 \times 10^{-4} - 8.318 \times 10^{-3}i$
0.25	$4.68 \times 10^{-4} - 8.59 \times 10^{-3}i$	$7.77 \times 10^{-4} - 1.212 \times 10^{-2}i$
0.275	$8.45 \times 10^{-4} - 1.170 \times 10^{-2}i$	$1.553 \times 10^{-3} - 1.735 \times 10^{-2}i$
0.3	$1.51 \times 10^{-3} - 1.57 \times 10^{-2}i$	$3.20 \times 10^{-3} - 2.46 \times 10^{-2}i$
0.325	$2.72 \times 10^{-3} - 2.08 \times 10^{-2}i$	$6.96 \times 10^{-3} - 3.47 \times 10^{-2}i$
0.35	$4.9 \times 10^{-3} - 2.7 \times 10^{-2}i$	$1.63 \times 10^{-2} - 4.8 \times 10^{-2}i$

VII. LEAST-SQUARES-FITTING RESULTS

We begin by discussing the different ways in which the least-squares-fitting program was checked. First, calculations were carried out at both 4 and 34.8 GHz for centered spherical raindrops, corresponding to $R(\theta) \equiv a$ in (15). The results were compared with the calculations based on the zero-order solution given in Section IV, corresponding to $\nu = 0$ in (47). Comparison was made for several values of a and different values of α, and excellent agreement was obtained for the far-field quantities, generally to six or seven significant figures. As expected, the far-field quantities are independent of the angle of incidence α.

Table III — Forward scattering amplitudes at 11 GHz with $\alpha = 90°$ for different drop sizes

$\bar{a}$(cm)	$S_{\mathrm{I}}(0)$	$S_{\mathrm{II}}(0)$
0.025	$4.8189 \times 10^{-6} - 1.8194 \times 10^{-4}i$	$5.0841 \times 10^{-6} - 1.8734 \times 10^{-4}i$
0.05	$5.9423 \times 10^{-5} - 1.4657 \times 10^{-3}i$	$6.5120 \times 10^{-5} - 1.5555 \times 10^{-3}i$
0.075	$3.6151 \times 10^{-4} - 5.0737 \times 10^{-3}i$	$4.0920 \times 10^{-4} - 5.5577 \times 10^{-3}i$
0.1	$1.6675 \times 10^{-3} - 1.2532 \times 10^{-2}i$	$1.9652 \times 10^{-3} - 1.4186 \times 10^{-2}i$
0.125	$6.5377 \times 10^{-3} - 2.5280 \times 10^{-2}i$	$8.0766 \times 10^{-3} - 2.9419 \times 10^{-2}i$
0.15	$2.0109 \times 10^{-2} - 4.0292 \times 10^{-2}i$	$2.4674 \times 10^{-2} - 4.6783 \times 10^{-2}i$
0.175	$3.7203 \times 10^{-2} - 4.7914 \times 10^{-2}i$	$4.1732 \times 10^{-2} - 5.8328 \times 10^{-2}i$
0.2	$4.735 \times 10^{-2} - 5.734 \times 10^{-2}i$	$5.492 \times 10^{-2} - 8.098 \times 10^{-2}i$
0.225	$5.958 \times 10^{-2} - 7.504 \times 10^{-2}i$	$7.929 \times 10^{-2} - 1.1621 \times 10^{-1}i$
0.25	$7.67 \times 10^{-2} - 9.68 \times 10^{-2}i$	$1.173 \times 10^{-1} - 1.580 \times 10^{-1}i$
0.275	$9.89 \times 10^{-2} - 1.225 \times 10^{-1}i$	$1.725 \times 10^{-1} - 2.060 \times 10^{-1}i$
0.3	$1.29 \times 10^{-1} - 1.51 \times 10^{-1}i$	$2.51 \times 10^{-1} - 2.54 \times 10^{-1}i$
0.325	$1.67 \times 10^{-1} - 1.78 \times 10^{-1}i$	$3.54 \times 10^{-1} - 2.93 \times 10^{-1}i$
0.35	$2.1 \times 10^{-1} - 2.0 \times 10^{-1}i$	$4.8 \times 10^{-1} - 3.1 \times 10^{-1}i$

Table IV — Forward scattering amplitudes at 18.1 GHz with $\alpha = 90°$ for different drop sizes

$\bar{a}$(cm)	$S_{\mathrm{I}}(0)$	$S_{\mathrm{II}}(0)$
0.025	$4.0158 \times 10^{-5} - 8.1579 \times 10^{-4}i$	$4.2246 \times 10^{-5} - 8.4000 \times 10^{-4}i$
0.05	$6.5425 \times 10^{-4} - 6.7265 \times 10^{-3}i$	$7.1168 \times 10^{-4} - 7.1424 \times 10^{-3}i$
0.075	$5.0674 \times 10^{-3} - 2.3476 \times 10^{-2}i$	$5.6959 \times 10^{-3} - 2.5717 \times 10^{-2}i$
0.1	$2.2608 \times 10^{-2} - 5.1254 \times 10^{-2}i$	$2.5696 \times 10^{-2} - 5.7588 \times 10^{-2}i$
0.125	$5.0374 \times 10^{-2} - 8.0587 \times 10^{-2}i$	$5.7722 \times 10^{-2} - 9.6353 \times 10^{-2}i$
0.15	$8.5403 \times 10^{-2} - 1.2201 \times 10^{-1}i$	$1.0834 \times 10^{-1} - 1.5714 \times 10^{-1}i$
0.175	$1.3950 \times 10^{-1} - 1.7392 \times 10^{-1}i$	$1.9921 \times 10^{-1} - 2.3098 \times 10^{-1}i$
0.2	$2.1700 \times 10^{-1} - 2.2871 \times 10^{-1}i$	$3.3903 \times 10^{-1} - 2.9883 \times 10^{-1}i$
0.225	$3.181 \times 10^{-1} - 2.742 \times 10^{-1}i$	$5.229 \times 10^{-1} - 3.320 \times 10^{-1}i$
0.25	$4.307 \times 10^{-1} - 2.999 \times 10^{-1}i$	$7.173 \times 10^{-1} - 3.136 \times 10^{-1}i$
0.275	$5.390 \times 10^{-1} - 3.089 \times 10^{-1}i$	$8.899 \times 10^{-1} - 2.633 \times 10^{-1}i$
0.3	$6.36 \times 10^{-1} - 3.12 \times 10^{-1}i$	$1.038 - 2.14 \times 10^{-1}i$
0.325	$7.22 \times 10^{-1} - 3.20 \times 10^{-1}i$	$1.179 - 1.84 \times 10^{-1}i$
0.35	$8.0 \times 10^{-1} - 3.4 \times 10^{-1}i$	$1.34 - 1.8 \times 10^{-1}i$

Moreover, the values of the coefficients obtained from least-squares fitting were checked against those calculated from (50) and (51), subject to (52), (53), and (119) to (122).

Next, the least-squares fit was carried out for spherical raindrops when the origin of the coordinate system was offset from the center of the raindrop, so that

$$R(\theta) = a[\delta \cos\theta + (1 - \delta^2 \sin^2\theta)^{\frac{1}{2}}]. \tag{73}$$

The calculations were done for different values of a, δ, and α, with the largest value of δ being 0.325 at 4 GHz and at 0.2 at 34.8 GHz. As ex-

Table V — Forward scattering amplitudes at 30 GHz with $\alpha = 90°$ for different drop sizes

$\bar{a}$(cm)	$S_{\mathrm{I}}(0)$	$S_{\mathrm{II}}(0)$
0.025	$3.4513 \times 10^{-4} - 3.7481 \times 10^{-3}i$	$3.6235 \times 10^{-4} - 3.8595 \times 10^{-3}i$
0.05	$6.9873 \times 10^{-3} - 3.1187 \times 10^{-2}i$	$7.5859 \times 10^{-3} - 3.3144 \times 10^{-2}i$
0.075	$4.5783 \times 10^{-2} - 9.5267 \times 10^{-2}i$	$5.1071 \times 10^{-2} - 1.0490 \times 10^{-1}i$
0.1	$1.3415 \times 10^{-1} - 1.8677 \times 10^{-1}i$	$1.6165 \times 10^{-1} - 2.1613 \times 10^{-1}i$
0.125	$2.9755 \times 10^{-1} - 2.8388 \times 10^{-1}i$	$3.8979 \times 10^{-1} - 3.2171 \times 10^{-1}i$
0.15	$5.1727 \times 10^{-1} - 3.3781 \times 10^{-1}i$	$6.9041 \times 10^{-1} - 3.3561 \times 10^{-1}i$
0.175	$7.3731 \times 10^{-1} - 3.4278 \times 10^{-1}i$	$9.6534 \times 10^{-1} - 2.7438 \times 10^{-1}i$
0.2	$9.274 \times 10^{-1} - 3.461 \times 10^{-1}i$	$1.2001 - 2.302 \times 10^{-1}i$
0.225	$1.1122 - 3.885 \times 10^{-1}i$	$1.4661 - 2.419 \times 10^{-1}i$
0.25	$1.3309 - 4.693 \times 10^{-1}i$	$1.8221 - 2.627 \times 10^{-1}i$
0.275	$1.601 - 5.57 \times 10^{-1}i$	$2.245 - 2.21 \times 10^{-1}i$
0.3	$1.902 - 6.23 \times 10^{-1}i$	$2.662 - 1.20 \times 10^{-1}i$
0.325	$2.20 - 6.70 \times 10^{-1}i$	$3.06 - 2.4 \times 10^{-2}i$
0.35	$2.49 - 7.3 \times 10^{-1}i$	$3.50 + 4 \times 10^{-2}i$

Table VI — Forward scattering amplitudes at 30 GHz with $\alpha = 70°$ for different drop sizes

$\bar{a}$(cm)	$S_{\mathrm{I}}(0)$	$S_{\mathrm{II}}(0)$
0.025	$3.4679 \times 10^{-4} - 3.7610 \times 10^{-3}i$	$3.6200 \times 10^{-4} - 3.8594 \times 10^{-3}i$
0.05	$7.0267 \times 10^{-3} - 3.1417 \times 10^{-2}i$	$7.5553 \times 10^{-3} - 3.3145 \times 10^{-2}i$
0.075	$4.6185 \times 10^{-2} - 9.6618 \times 10^{-2}i$	$5.0856 \times 10^{-2} - 1.0513 \times 10^{-1}i$
0.1	$1.3701 \times 10^{-1} - 1.9131 \times 10^{-1}i$	$1.6133 \times 10^{-1} - 2.1727 \times 10^{-1}i$
0.125	$3.0867 \times 10^{-1} - 2.9154 \times 10^{-1}i$	$3.9039 \times 10^{-1} - 3.2498 \times 10^{-1}i$
0.15	$5.4041 \times 10^{-1} - 3.4346 \times 10^{-1}i$	$6.9413 \times 10^{-1} - 3.4113 \times 10^{-1}i$
0.175	$7.7133 \times 10^{-1} - 3.4313 \times 10^{-1}i$	$9.7408 \times 10^{-1} - 2.8097 \times 10^{-1}i$
0.2	$9.723 \times 10^{-1} - 3.425 \times 10^{-1}i$	$1.2143 - 2.357 \times 10^{-1}i$
0.225	$1.1720 - 3.832 \times 10^{-1}i$	$1.4838 - 2.454 \times 10^{-1}i$
0.25	$1.4123 - 4.621 \times 10^{-1}i$	$1.8412 - 2.678 \times 10^{-1}i$
0.275	$1.710 - 5.45 \times 10^{-1}i$	$2.269 - 2.34 \times 10^{-1}i$
0.3	$2.042 - 6.04 \times 10^{-1}i$	$2.699 - 1.41 \times 10^{-1}i$
0.325	$2.38 - 6.46 \times 10^{-1}i$	$3.11 - 4.8 \times 10^{-2}i$
0.35	$2.71 - 7.0 \times 10^{-1}i$	$3.56 + 1.5 \times 10^{-2}i$

pected, the far-field quantities are independent of δ, as well as α, and again excellent results were obtained. These calculations provided a nontrivial check on the programming of the boundary conditions, since $dR/d\theta \not\equiv 0$. In addition, they gave some idea of the increase in the number of terms in n that is required, a result of the ratio of maximum to minimum distance from the raindrop surface to the origin, which is necessarily greater than unity for oblate spheroidal raindrops.

As a final check on the least-squares-fitting program, calculations were carried out at 34.8 GHz for oblate spheroidal raindrops with small

Table VII — Forward scattering amplitudes at 30 GHz with $\alpha = 50°$ for different drop sizes

$\bar{a}$(cm)	$S_{\mathrm{I}}(0)$	$S_{\mathrm{II}}(0)$
0.025	$3.5101 \times 10^{-4} - 3.7936 \times 10^{-3}i$	$3.6111 \times 10^{-4} - 3.8590 \times 10^{-3}i$
0.05	$7.1265 \times 10^{-3} - 3.1998 \times 10^{-2}i$	$7.4779 \times 10^{-3} - 3.3147 \times 10^{-2}i$
0.075	$4.7204 \times 10^{-2} - 1.0005 \times 10^{-1}i$	$5.0312 \times 10^{-2} - 1.0571 \times 10^{-1}i$
0.1	$1.4431 \times 10^{-1} - 2.0284 \times 10^{-1}i$	$1.6054 \times 10^{-1} - 2.2016 \times 10^{-1}i$
0.125	$3.3714 \times 10^{-1} - 3.1102 \times 10^{-1}i$	$3.9193 \times 10^{-1} - 3.3329 \times 10^{-1}i$
0.15	$6.0012 \times 10^{-1} - 3.5745 \times 10^{-1}i$	$7.0369 \times 10^{-1} - 3.5523 \times 10^{-1}i$
0.175	$8.5967 \times 10^{-1} - 3.4211 \times 10^{-1}i$	$9.9679 \times 10^{-1} - 2.9777 \times 10^{-1}i$
0.2	$1.0888 - 3.278 \times 10^{-1}i$	$1.2518 - 2.491 \times 10^{-1}i$
0.225	$1.3247 - 3.580 \times 10^{-1}i$	$1.5306 - 2.520 \times 10^{-1}i$
0.25	$1.6145 - 4.252 \times 10^{-1}i$	$1.8902 - 2.752 \times 10^{-1}i$
0.275	$1.974 - 4.91 \times 10^{-1}i$	$2.327 - 2.58 \times 10^{-1}i$
0.3	$2.379 - 5.27 \times 10^{-1}i$	$2.785 - 1.87 \times 10^{-1}i$
0.325	$2.80 - 5.45 \times 10^{-1}i$	$3.24 - 1.03 \times 10^{-1}i$
0.35	$3.24 - 5.7 \times 10^{-1}i$	$3.72 - 4 \times 10^{-2}i$

Table VIII — Total and scattering cross sections at 4 GHz with $\alpha = 90°$ for different drop sizes

$\bar{a}$(cm)	Q_t^{I}(cm)^2	Q_t^{II}(cm)^2	Q_s^{I}(cm)^2	Q_s^{II}(cm)^2
0.025	1.2393×10^{-6}	1.3126×10^{-6}	8.9950×10^{-10}	9.5367×10^{-10}
0.05	1.0545×10^{-5}	1.1782×10^{-5}	5.5428×10^{-8}	6.2399×10^{-8}
0.075	4.0327×10^{-5}	4.7215×10^{-5}	6.0811×10^{-7}	7.2816×10^{-7}
0.1	1.1406×10^{-4}	1.3909×10^{-4}	3.2922×10^{-6}	4.2012×10^{-6}
0.125	2.7599×10^{-4}	3.4947×10^{-4}	1.2106×10^{-5}	1.6500×10^{-5}
0.15	6.0592×10^{-4}	7.9725×10^{-4}	3.4869×10^{-5}	5.0884×10^{-5}
0.175	1.2432×10^{-3}	1.7068×10^{-3}	8.4904×10^{-5}	1.3303×10^{-4}
0.2	2.427×10^{-3}	3.503×10^{-3}	1.830×10^{-4}	3.088×10^{-4}
0.225	4.568×10^{-3}	7.011×10^{-3}	3.599×10^{-4}	6.567×10^{-4}
0.25	8.38×10^{-3}	1.391×10^{-2}	6.60×10^{-4}	1.309×10^{-3}
0.275	1.51×10^{-2}	2.78×10^{-2}	1.15×10^{-3}	2.50×10^{-3}
0.3	2.71×10^{-2}	5.73×10^{-2}	1.93×10^{-3}	4.7×10^{-3}
0.325	4.87×10^{-2}	1.246×10^{-1}	3.2×10^{-3}	8.8×10^{-3}
0.35	8.8×10^{-2}	2.92×10^{-1}	5.2×10^{-3}	1.78×10^{-2}

eccentricity, corresponding to $\nu = 0$, 0.05, 0.1, and 0.15 in (63). The calculations were done for $\alpha = 90°$ and for $a = 0.025(0.025)0.275$. Corresponding to (48), the total cross section may be expanded in the form $Q_t = Q_t^{(0)} + \nu Q_t^{(1)} + \cdots$. Values of $Q_t^{I(1)}$ and $Q_t^{II(1)}$ were obtained from the least-squares results by extrapolation and were compared with the perturbation values given by Oguchi.[4] Unfortunately, there were significant discrepancies for the larger drop sizes, the largest error being more than 17 percent. Consequently, we did the perturbation calculations ourselves and obtained results differing from our extrap-

Table IX — Total and scattering cross sections at 11 GHz with $\alpha = 90°$ for different drop sizes

$\bar{a}$(cm)	Q_t^{I}(cm)^2	Q_t^{II}(cm)^2	Q_s^{I}(cm)^2	Q_s^{II}(cm)^2
0.025	1.1407×10^{-5}	1.2035×10^{-5}	5.1556×10^{-8}	5.4666×10^{-8}
0.05	1.4066×10^{-4}	1.5415×10^{-4}	3.2095×10^{-6}	3.6172×10^{-6}
0.075	8.5573×10^{-4}	9.6863×10^{-4}	3.5933×10^{-5}	4.3203×10^{-5}
0.1	3.9471×10^{-3}	4.6519×10^{-3}	2.0259×10^{-4}	2.6114×10^{-4}
0.125	1.5476×10^{-2}	1.9118×10^{-2}	8.1236×10^{-4}	1.1302×10^{-3}
0.15	4.7600×10^{-2}	5.8407×10^{-2}	2.7238×10^{-3}	4.0701×10^{-3}
0.175	8.8064×10^{-2}	9.8785×10^{-2}	7.3803×10^{-3}	1.1535×10^{-2}
0.2	1.1208×10^{-1}	1.3001×10^{-1}	1.559×10^{-2}	2.643×10^{-2}
0.225	1.4103×10^{-1}	1.8769×10^{-1}	2.815×10^{-2}	5.325×10^{-2}
0.25	1.815×10^{-1}	2.777×10^{-1}	4.60×10^{-2}	9.76×10^{-2}
0.275	2.341×10^{-1}	4.084×10^{-1}	7.21×10^{-2}	1.701×10^{-1}
0.3	3.05×10^{-1}	5.94×10^{-1}	1.09×10^{-1}	2.84×10^{-1}
0.325	3.95×10^{-1}	8.4×10^{-1}	1.57×10^{-1}	4.5×10^{-1}
0.35	5.0×10^{-1}	1.13	2.1×10^{-1}	6.5×10^{-1}

Table X — Total and scattering cross sections at 18.1 GHz with $\alpha = 90°$ for different drop sizes

$\bar{a}$(cm)	Q_t^{I}(cm)^2	Q_t^{II}(cm)^2	Q_s^{I}(cm)^2	Q_s^{II}(cm)^2
0.025	3.5118×10^{-5}	3.6944×10^{-5}	3.7881×10^{-7}	4.0173×10^{-7}
0.05	5.7214×10^{-4}	6.2236×10^{-4}	2.4119×10^{-5}	2.7242×10^{-5}
0.075	4.4314×10^{-3}	4.9810×10^{-3}	2.8514×10^{-4}	3.4542×10^{-4}
0.1	1.9770×10^{-2}	2.2471×10^{-2}	1.7668×10^{-3}	2.3060×10^{-3}
0.125	4.4052×10^{-2}	5.0478×10^{-2}	7.1078×10^{-3}	1.0013×10^{-2}
0.15	7.4684×10^{-2}	9.4745×10^{-2}	1.9966×10^{-2}	3.0950×10^{-2}
0.175	1.2199×10^{-1}	1.7421×10^{-1}	4.3974×10^{-2}	7.4834×10^{-2}
0.2	1.8976×10^{-1}	2.9648×10^{-1}	8.312×10^{-2}	1.5229×10^{-1}
0.225	2.782×10^{-1}	4.572×10^{-1}	1.377×10^{-1}	2.640×10^{-1}
0.25	3.766×10^{-1}	6.273×10^{-1}	1.999×10^{-1}	3.888×10^{-1}
0.275	4.714×10^{-1}	7.782×10^{-1}	2.598×10^{-1}	5.028×10^{-1}
0.3	5.56×10^{-1}	9.08×10^{-1}	3.12×10^{-1}	6.00×10^{-1}
0.325	6.32×10^{-1}	1.031	3.54×10^{-1}	6.89×10^{-1}
0.35	7.0×10^{-1}	1.17	3.9×10^{-1}	7.8×10^{-1}

olated least-squares results by at most $\frac{1}{2}$ percent, which is reasonably consistent with the error to be expected from the extrapolation. Oguchi[34] has since redone his calculations, and he agrees with our perturbation results. The same good agreement was obtained between the extrapolated and perturbation values of $S_{\mathrm{I}}^{(1)}(0)$, $S_{\mathrm{II}}^{(1)}(0)$, $Q_s^{\mathrm{I}(1)}$, and $Q_s^{\mathrm{II}(1)}$.

After the least-squares-fitting program had been checked in the above manner, we carried out calculations for oblate spheroidal raindrops corresponding to (63), with a and ν given by (64). Here $\bar{a}$ is the

Table XI — Total and scattering cross sections at 30 GHz with $\alpha = 90°$ for different drop sizes

$\bar{a}$(cm)	Q_t^{I}(cm)^2	Q_t^{II}(cm)^2	Q_s^{I}(cm)^2	Q_s^{II}(cm)^2
0.025	1.0986×10^{-4}	1.1534×10^{-4}	2.8823×10^{-6}	3.0581×10^{-6}
0.05	2.2241×10^{-3}	2.4147×10^{-3}	1.9542×10^{-4}	2.2197×10^{-4}
0.075	1.4573×10^{-2}	1.6256×10^{-2}	2.5201×10^{-3}	3.1009×10^{-3}
0.1	4.2701×10^{-2}	5.1454×10^{-2}	1.4263×10^{-2}	1.9185×10^{-2}
0.125	9.4713×10^{-2}	1.2407×10^{-1}	4.3818×10^{-2}	6.2849×10^{-2}
0.15	1.6465×10^{-1}	2.1977×10^{-1}	8.9103×10^{-2}	1.2903×10^{-1}
0.175	2.3469×10^{-1}	3.0728×10^{-1}	1.3595×10^{-1}	1.9338×10^{-1}
0.2	2.9521×10^{-1}	3.8199×10^{-1}	1.7408×10^{-1}	2.4628×10^{-1}
0.225	3.5403×10^{-1}	4.6666×10^{-1}	2.0731×10^{-1}	3.0183×10^{-1}
0.25	4.236×10^{-1}	5.800×10^{-1}	2.450×10^{-1}	3.766×10^{-1}
0.275	5.095×10^{-1}	7.146×10^{-1}	2.938×10^{-1}	4.710×10^{-1}
0.3	6.05×10^{-1}	8.47×10^{-1}	3.51×10^{-1}	5.69×10^{-1}
0.325	7.01×10^{-1}	9.74×10^{-1}	4.08×10^{-1}	6.62×10^{-1}
0.35	7.9×10^{-1}	1.11	4.6×10^{-1}	7.6×10^{-1}

Table XII — Total and scattering cross sections at 30 GHz with $\alpha = 70°$ for different drop sizes

$\bar{a}$(cm)	Q_t^{I}(cm)^2	Q_t^{II}(cm)^2	Q_s^{I}(cm)^2	Q_s^{II}(cm)^2
0.025	1.1039×10^{-4}	1.1523×10^{-4}	2.9029×10^{-6}	3.0582×10^{-6}
0.05	2.2367×10^{-3}	2.4049×10^{-3}	1.9851×10^{-4}	2.2196×10^{-4}
0.075	1.4701×10^{-2}	1.6188×10^{-2}	2.5867×10^{-3}	3.1000×10^{-3}
0.1	4.3613×10^{-2}	5.1354×10^{-2}	1.4859×10^{-2}	1.9213×10^{-2}
0.125	9.8252×10^{-2}	1.2427×10^{-1}	4.6292×10^{-2}	6.3156×10^{-2}
0.15	1.7202×10^{-1}	2.2095×10^{-1}	9.4694×10^{-2}	1.3017×10^{-1}
0.175	2.4552×10^{-1}	3.1006×10^{-1}	1.4482×10^{-1}	1.9599×10^{-1}
0.2	3.0950×10^{-1}	3.8653×10^{-1}	1.8634×10^{-1}	2.5071×10^{-1}
0.225	3.7305×10^{-1}	4.7231×10^{-1}	2.2389×10^{-1}	3.0787×10^{-1}
0.25	4.496×10^{-1}	5.861×10^{-1}	2.676×10^{-1}	3.837×10^{-1}
0.275	5.442×10^{-1}	7.223×10^{-1}	3.240×10^{-1}	4.796×10^{-1}
0.3	6.50×10^{-1}	8.59×10^{-1}	3.90×10^{-1}	5.81×10^{-1}
0.325	7.57×10^{-1}	9.91×10^{-1}	4.58×10^{-1}	6.79×10^{-1}
0.35	8.6×10^{-1}	1.13	5.2×10^{-1}	7.8×10^{-1}

radius (in centimeters) of the equivolumic spherical drop, and the calculations were done for $\bar{a} = 0.025(0.025)0.35$. The corresponding values of a and ν are given in Table I. The values taken for the wavelength $\lambda = 2\pi/k_0$ were (in centimeters) 7.5, 2.727, 1.6575, and 1.0, corresponding approximately to frequencies of 4, 11, 18.1, and 30 GHz. At 20°C, the refractive indices $N = 7.884 + 2.184i$ at 11 GHz, $N = 6.859 + 2.716i$ at 18.1 GHz, and $N = 5.581 + 2.848i$ at 30 GHz were obtained from an elaborate fitting equation in a recently published survey[8] of available measured data. Since the calculations at 4 GHz were made at an earlier date, the value $N = 8.77 + 0.915i$, taken from the older

Table XIII — Total and scattering cross sections at 30 GHz with $\alpha = 50°$ for different drop sizes

$\bar{a}$(cm)	Q_t^{I}(cm)^2	Q_t^{II}(cm)^2	Q_s^{I}(cm)^2	Q_s^{II}(cm)^2
0.025	1.1173×10^{-4}	1.1495×10^{-4}	2.9552×10^{-6}	3.0584×10^{-6}
0.05	2.2684×10^{-3}	2.3803×10^{-3}	2.0634×10^{-4}	2.2193×10^{-4}
0.075	1.5025×10^{-2}	1.6015×10^{-2}	2.7560×10^{-3}	3.0978×10^{-3}
0.1	4.5936×10^{-2}	5.1102×10^{-2}	1.6378×10^{-2}	1.9286×10^{-2}
0.125	1.0732×10^{-1}	1.2476×10^{-1}	5.2632×10^{-2}	6.3941×10^{-2}
0.15	1.9102×10^{-1}	2.2399×10^{-1}	1.0914×10^{-1}	1.3308×10^{-1}
0.175	2.7364×10^{-1}	3.1729×10^{-1}	1.6796×10^{-1}	2.0272×10^{-1}
0.2	3.4658×10^{-1}	3.9846×10^{-1}	2.1846×10^{-1}	2.6230×10^{-1}
0.225	4.2166×10^{-1}	4.8721×10^{-1}	2.6706×10^{-1}	3.2371×10^{-1}
0.25	5.139×10^{-1}	6.017×10^{-1}	3.253×10^{-1}	4.021×10^{-1}
0.275	6.283×10^{-1}	7.405×10^{-1}	3.996×10^{-1}	5.009×10^{-1}
0.3	7.57×10^{-1}	8.87×10^{-1}	4.87×10^{-1}	6.09×10^{-1}
0.325	8.9×10^{-1}	1.03	5.8×10^{-1}	7.2×10^{-1}
0.35	1.03	1.18	6.75×10^{-1}	8.3×10^{-1}

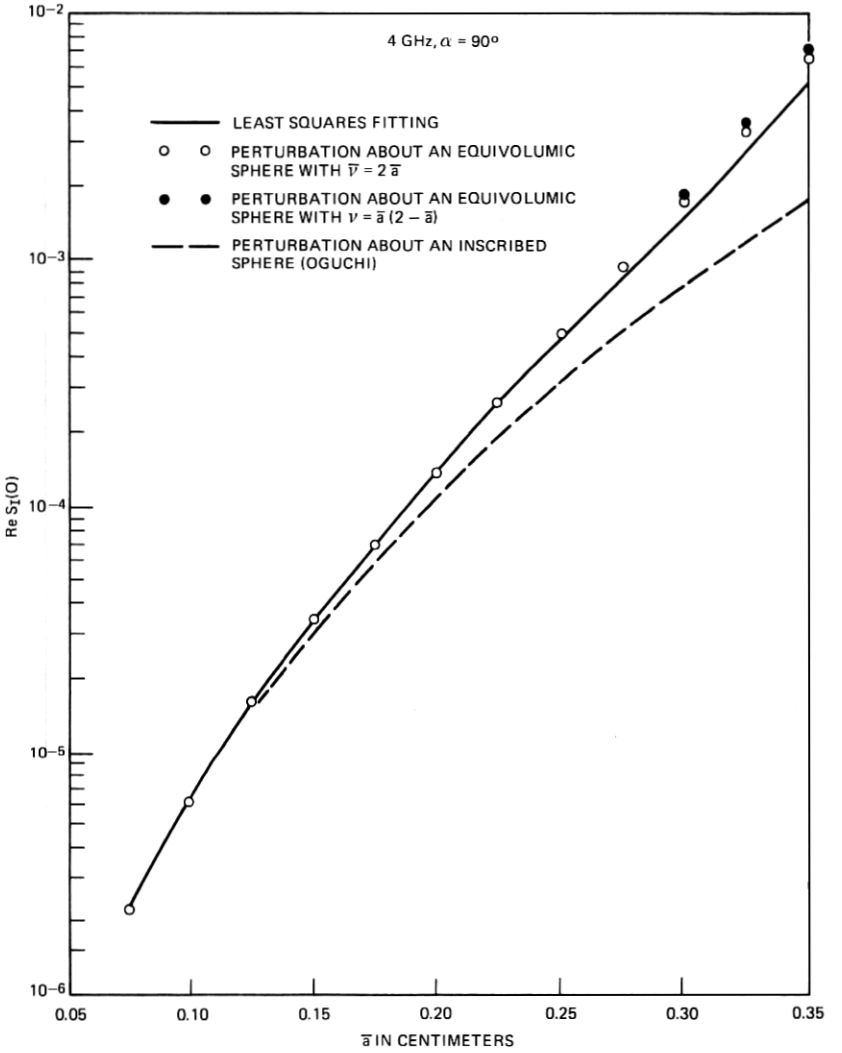

Fig. 3—Comparison of perturbation approximations to the least-squares-fitting value of Re $S_I(0)$ at 4 GHz with $\alpha = 90°$ as a function of drop size.

literature, was used, rather than $N = 8.78 + 0.977i$. The angle of incidence α was taken to be 90° at 4, 11, and 18.1 GHz, while at 30 GHz the calculations were done for $\alpha = 70°$ and $\alpha = 50°$ also.

The calculated values of the forward scattering amplitudes $S_I(0)$ and $S_{II}(0)$ are given in Tables II to VII, and those of the total cross

sections Q_t^{I} and Q_t^{II} and the scattering cross sections Q_s^{I} and Q_s^{II} are given in Tables VIII to XIII, all rounded in the last significant figure. The values of the absorption cross sections Q_a^{I} and Q_a^{II} follow from (38).

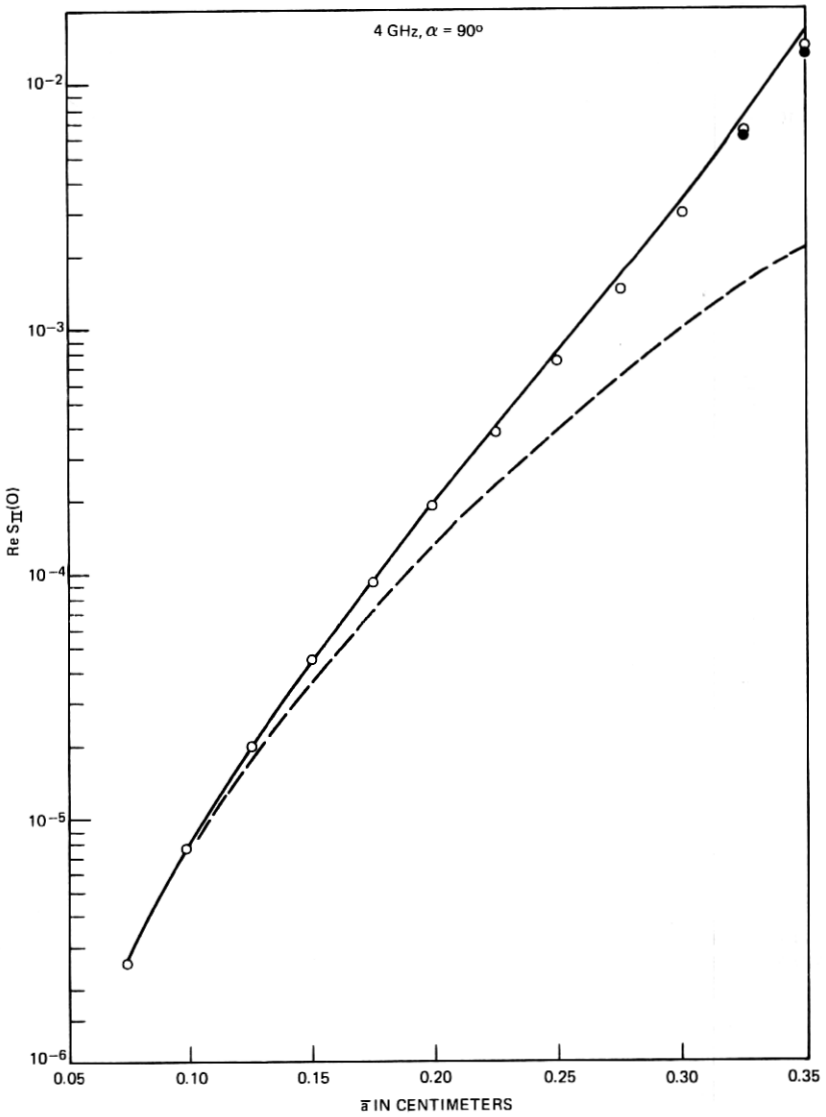

Fig. 4—Comparison of perturbation approximations to the least-squares-fitting value of Re $S_{\mathrm{II}}(0)$ at 4 GHz with $\alpha = 90°$ as a function of drop size.

The accuracy of the least-squares fit of the boundary conditions decreases with increasing drop size, because of the increase in eccentricity, which is why fewer significant figures are given in the tables for the larger drop sizes. Except for the smaller drop sizes, for which the results could be given more accurately, the number of significant figures reflects the degree of convergence of the results, as evidenced by increasing the upper limit of n in the least-squares fit by 2 and by 4. The

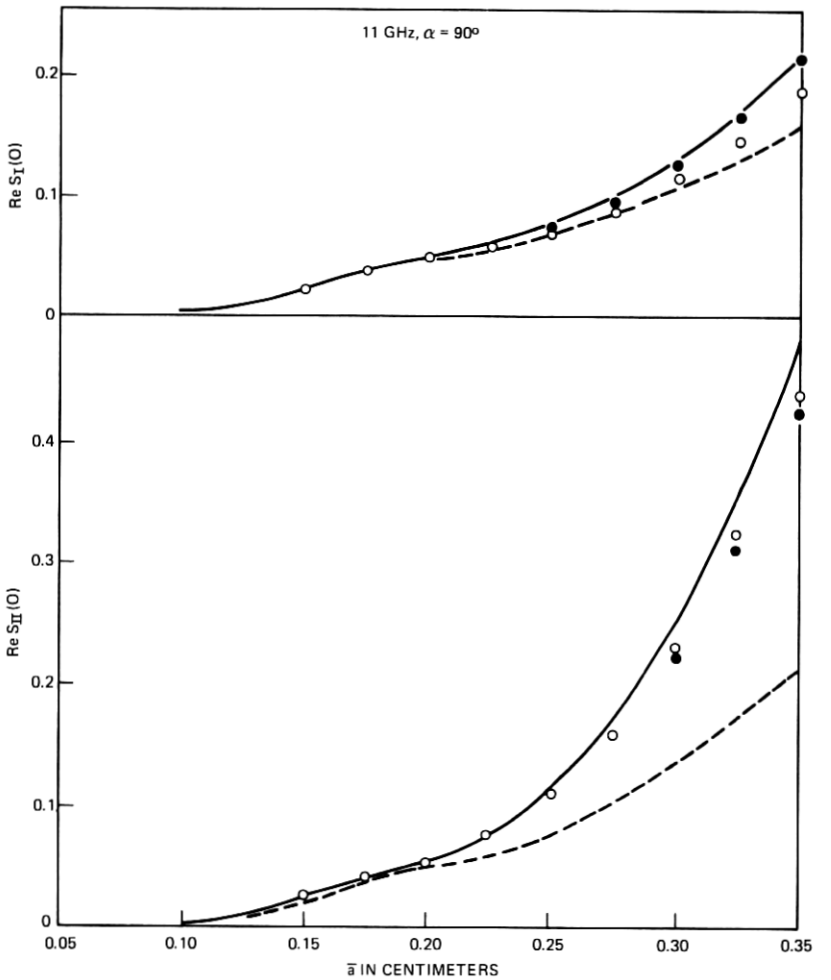

Fig. 5—Comparison of perturbation approximations to the least-squares-fitting values of Re $S_{\mathrm{I}}(0)$ and Re $S_{\mathrm{II}}(0)$ at 11 GHz with $\alpha = 90°$ as a function of drop size.

accuracy of the far-field results is generally at least one order of magnitude greater than that of the fit of the boundary conditions for the reasons discussed in Section V. We note that the largest drops occur only at the heaviest rain rates,[7] and then only a small percentage of them, so that the lower accuracy of the results for these drops is acceptable when summing over the drop size distribution.

The number of terms required to obtain the desired accuracy for the far-field quantities and to adequately satisfy the boundary conditions increases with both drop size and with frequency. At 4 GHz, it was found that max $m = 4$ and max $n = 17$ were sufficient for the largest drop size. For $\alpha = 90°$ at 30 GHz, it was necessary to take max $m = 8$ and max $n = 23$ for the largest drop size. In this latter case, more than half the capacity of the Honeywell 6070 computer was used. In some cases, it was found that max n or max m could not be increased without causing overflow in some of the subroutines, in particular SBES and L2FIT.

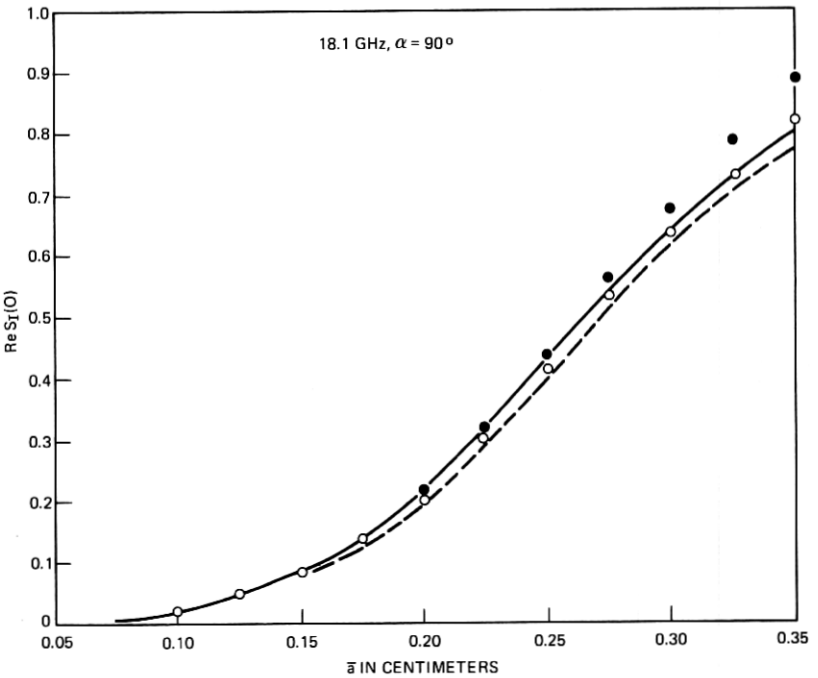

Fig. 6—Comparison of perturbation approximations to the least-squares-fitting value of Re $S_1(0)$ at 18.1 GHz with $\alpha = 90°$ as a function of drop size.

To check on the advantage of using least-squares fitting (with approximately twice as many fitting points as unknown coefficients) rather than collocation, we used collocation in several cases at different frequencies and for different drop sizes. Our general conclusion is that, for the same max m and max n, results may be obtained by collocation for the far-field quantities that are almost as accurate as those obtained by least-squares fitting. However, there are much larger errors in the boundary conditions (in between the fitting points) with collocation

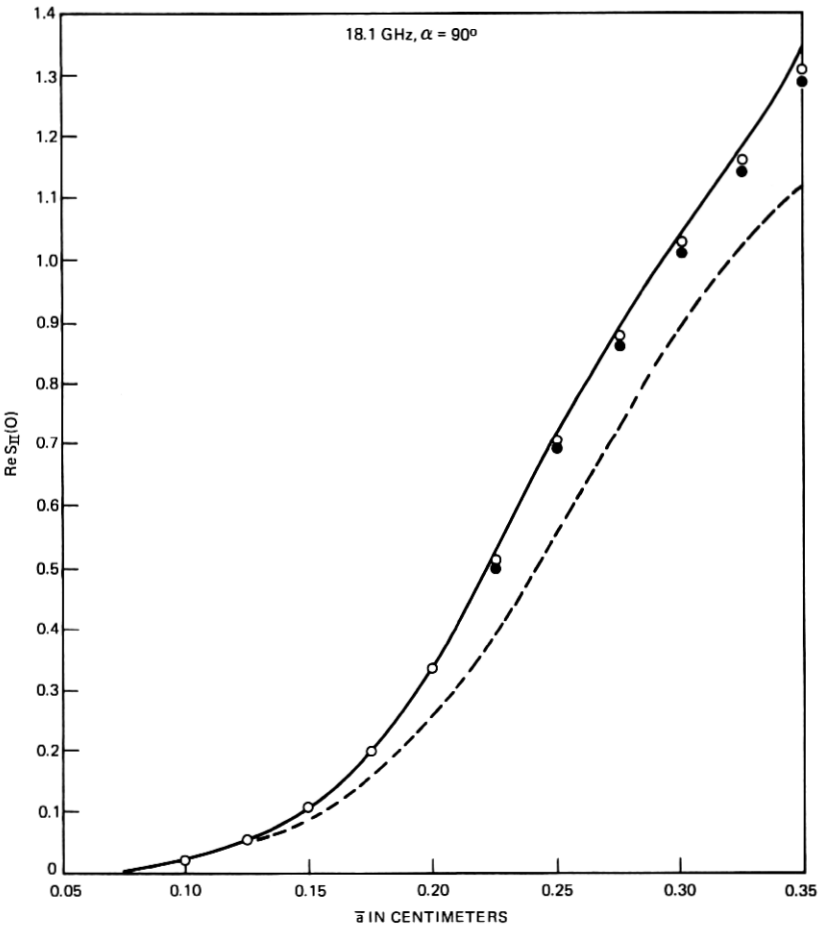

Fig. 7—Comparison of perturbation approximations to the least-squares-fitting value of Re $S_{11}(0)$ at 18.1 GHz with $\alpha = 90°$ as a function of drop size.

than with least-squares fitting. For the larger, more eccentric raindrops, some of these errors were of the order of 100 percent, which seem to be unacceptable. However, for the smaller raindrops, the errors in the boundary conditions with collocation are acceptable. Since the cost of carrying out the least-squares fit is less when fewer fitting points are used, collocation has the advantage of reducing the cost, although fewer terms are required, anyway, to obtain the desired accuracy for the smaller raindrops. It is possible that the collocation fit may be improved

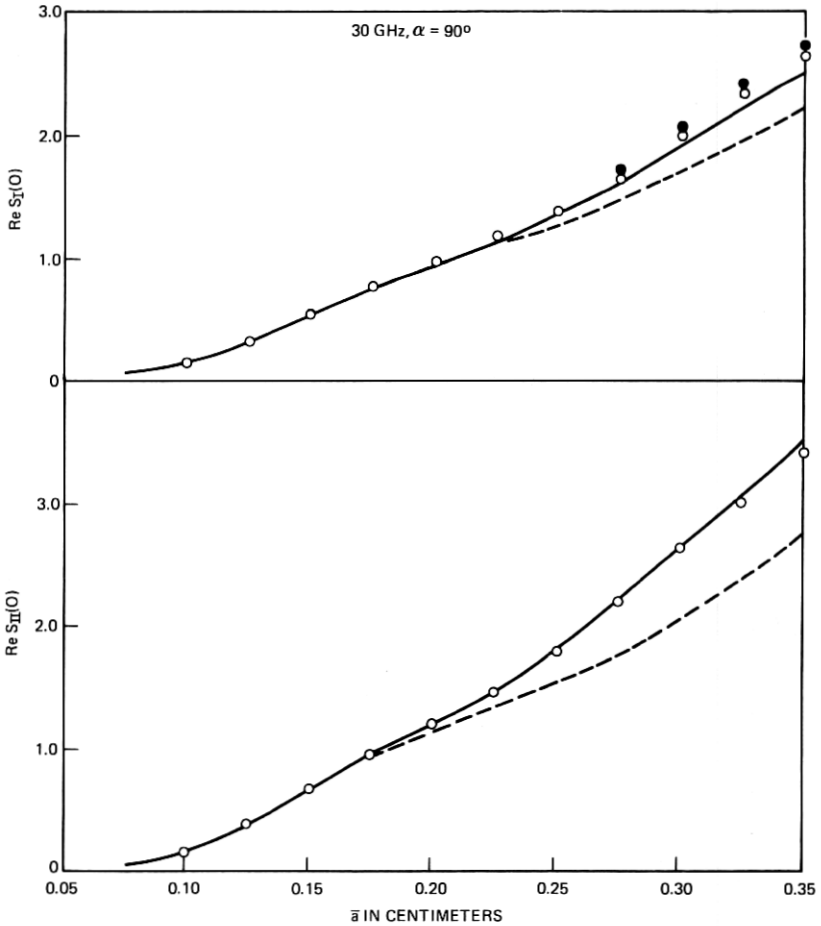

Fig. 8—Comparison of perturbation approximations to the least-squares-fitting values of Re $S_{\mathrm{I}}(0)$ and Re $S_{\mathrm{II}}(0)$ at 30 GHz with $\alpha = 90°$ as a function of drop size.

by satisfying the boundary conditions at nonuniformly spaced points, but we have not investigated this.

As a check on the point-matching (collocation) results of Oguchi,[5] we carried out the least-squares fitting for $\alpha = 90°$, at 19.3 GHz for $\bar{a} = 0.3$ and at 34.8 GHz for $\bar{a} = 0.075$, 0.15, 0.225, and 0.3, using

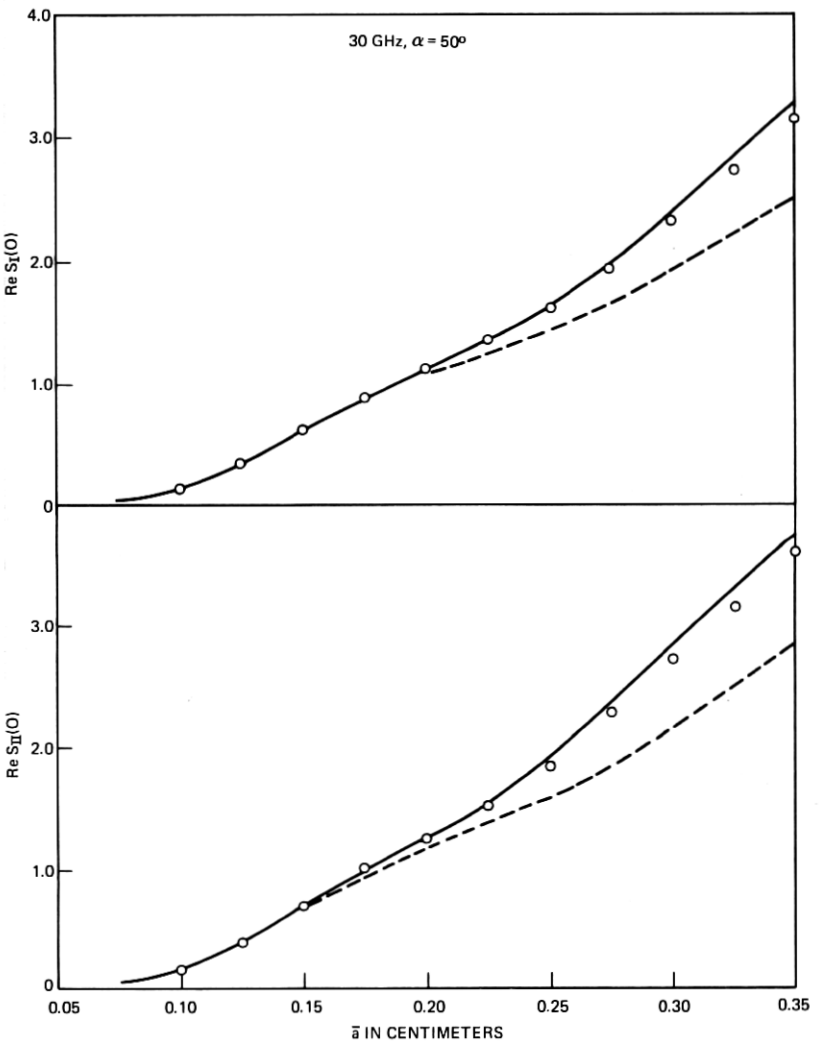

Fig. 9—Comparison of perturbation approximations to the least-squares-fitting values of Re $S_{\mathrm{I}}(0)$ and Re $S_{\mathrm{II}}(0)$ at 30 GHz with $\alpha = 50°$ as a function of drop size.

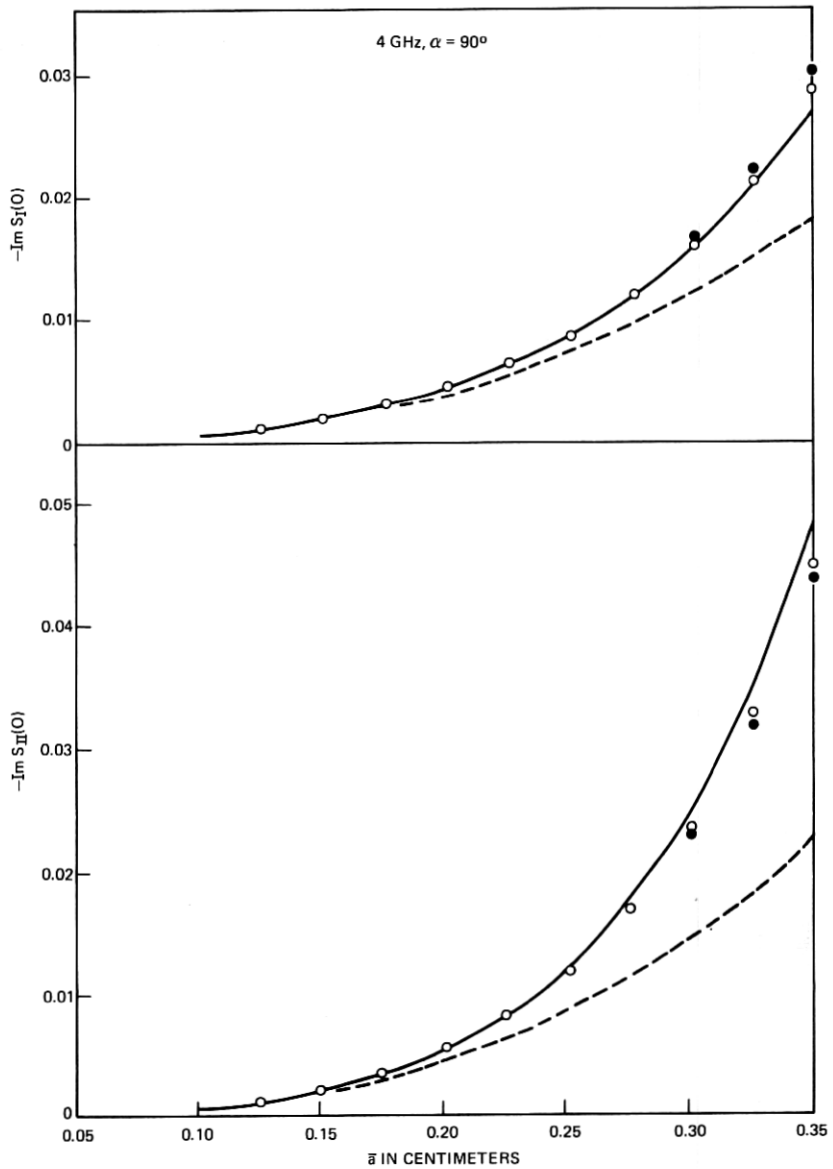

Fig. 10—Comparison of perturbation approximations to the least-squares-fitting values of Im $S_{\mathrm{I}}(0)$ and Im $S_{\mathrm{II}}(0)$ at 4 GHz with $\alpha = 90°$ as a function of drop size.

Oguchi's relationship[5]

$$\frac{a}{b} = \left(1 - \frac{4.1}{4.5}\,\bar{a}\right), \tag{74}$$

instead of the first relationship in (1). Our results for the forward scattering amplitudes are consistent with his point-matching values, but they may be given to greater accuracy. Our truncated values for $\bar{a} = 0.3$ are given below where, in Oguchi's notation,[5]

$$f^v \times 10^3 = \frac{-5\lambda}{\pi}\, iS_{\mathrm{I}}^*(0), \qquad f^h \times 10^3 = \frac{-5\lambda}{\pi}\, iS_{\mathrm{II}}^*(0), \tag{75}$$

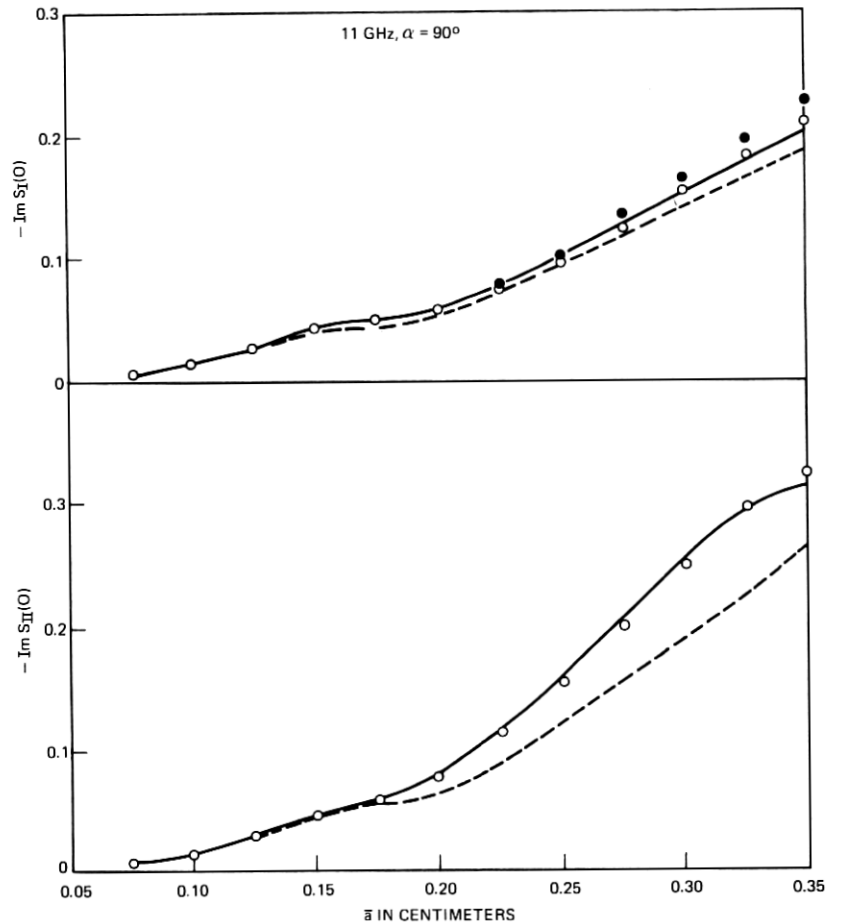

Fig. 11—Comparison of perturbation approximations to the least-squares-fitting values of Im $S_{\mathrm{I}}(0)$ and Im $S_{\mathrm{II}}(0)$ at 11 GHz with $\alpha = 90°$ as a function of drop size.

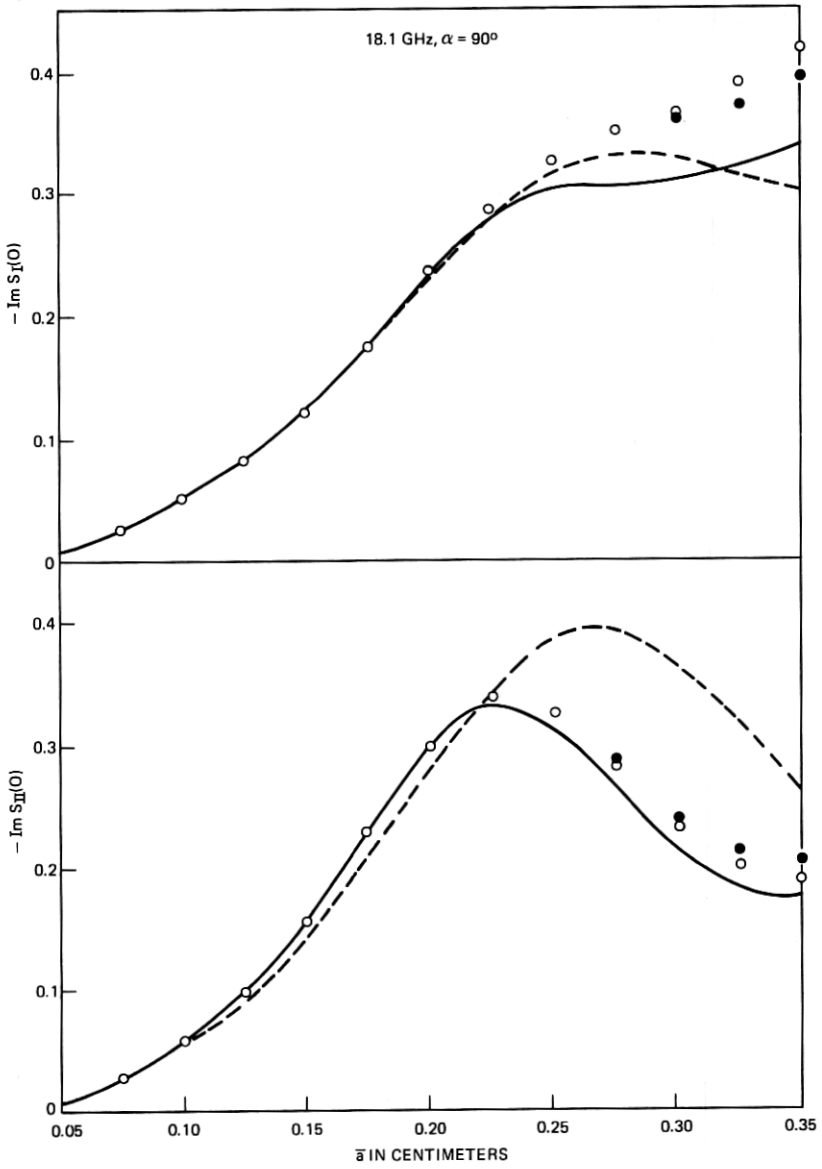

Fig. 12—Comparison of perturbation approximations to the least-squares-fitting values of Im $S_{\mathrm{I}}(0)$ and Im $S_{\mathrm{II}}(0)$ at 18.1 GHz with $\alpha = 90°$ as a function of drop size.

and the vertical lines indicate where Oguchi truncated his results:

GHz	$f^v \times 10^3$	$f^h \times 10^3$
19.3	$0.81\,\vert 30 - 1.884\,\vert i$	$0.510\,\vert 9 - 2.81\,\vert 7i$
34.8	$0.917\,\vert 8 - 3.73\,\vert 0i$	$\vert 0.0646 - 4.71\,\vert 0i$

The values taken[34] for the wavelength λ (in centimeters) were 1.5533330 and 0.86135810, corresponding approximately to frequencies of 19.3 and 34.8 GHz, with refractive indices $N = 6.5449188 + 2.8104040i$ and $N = 5.0487284 + 2.7948416i$, respectively.

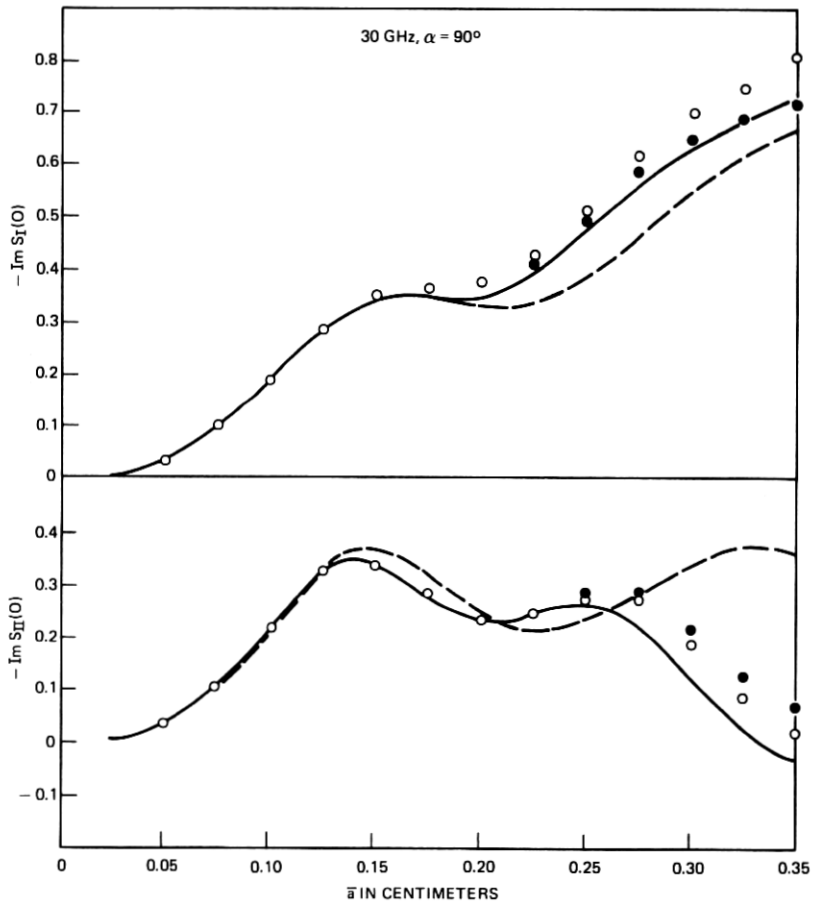

Fig. 13—Comparison of perturbation approximations to the least-squares-fitting values of Im $S_I(0)$ and Im $S_{II}(0)$ at 30 GHz with $\alpha = 90°$ as a function of drop size.

The main reason for the greater accuracy of our results is that we took larger values of max n than Oguchi, who did the point-matching at both frequencies for max $n = 12$ and 14, with max $m =$ max n. For $\bar{a} = 0.3$ we took max $m = 7$ at 19.3 GHz and max $m = 9$ at 34.8 GHz, which were sufficient, and took max $n = 21$ at both frequencies for the least-squares fitting. We also used collocation for $\bar{a} = 0.3$ and max $n = 12$, 14, and 21. For max $n = 21$ the collocation results differ by at most 1 in the last decimal place from the results given above, but errors in some boundary conditions were of the order of 10 percent, as compared with much less than 1 percent for least-squares fitting. This is consistent with our general conclusion discussed earlier in this section. We point out that the raindrops satisfying (74) are less eccentric than those satisfying (1), so that the overall errors are correspondingly smaller. For collocation with max $n = 14$, some errors in the boundary conditions were close to 100 percent, which explains why, with point-matching, Oguchi did not give any significant figures for Re f^h at 34.8 GHz, for either $\bar{a} = 0.3$ or $\bar{a} = 0.325$.

Although Oguchi[5] gives four significant figures for f^v and f^h at 34.8

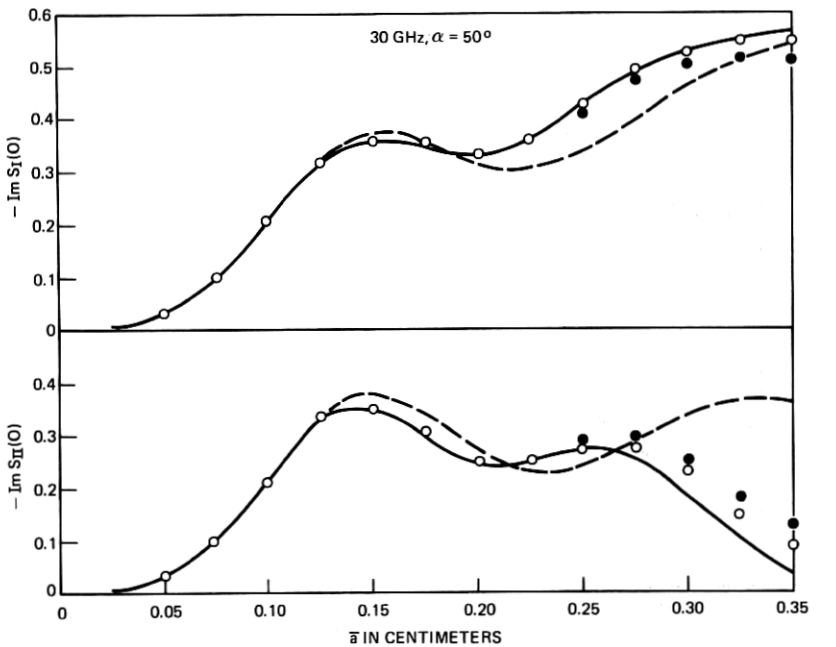

Fig. 14—Comparison of perturbation approximations to the least-squares-fitting values of Im $S_I(0)$ and Im $S_{II}(0)$ at 30 GHz with $\alpha = 50°$ as a function of drop size.

GHz for all drop sizes corresponding to his solution in terms of spheroidal wave functions (with modal sums truncated at 9), these values are not consistent with his point-matching ones for the larger drop

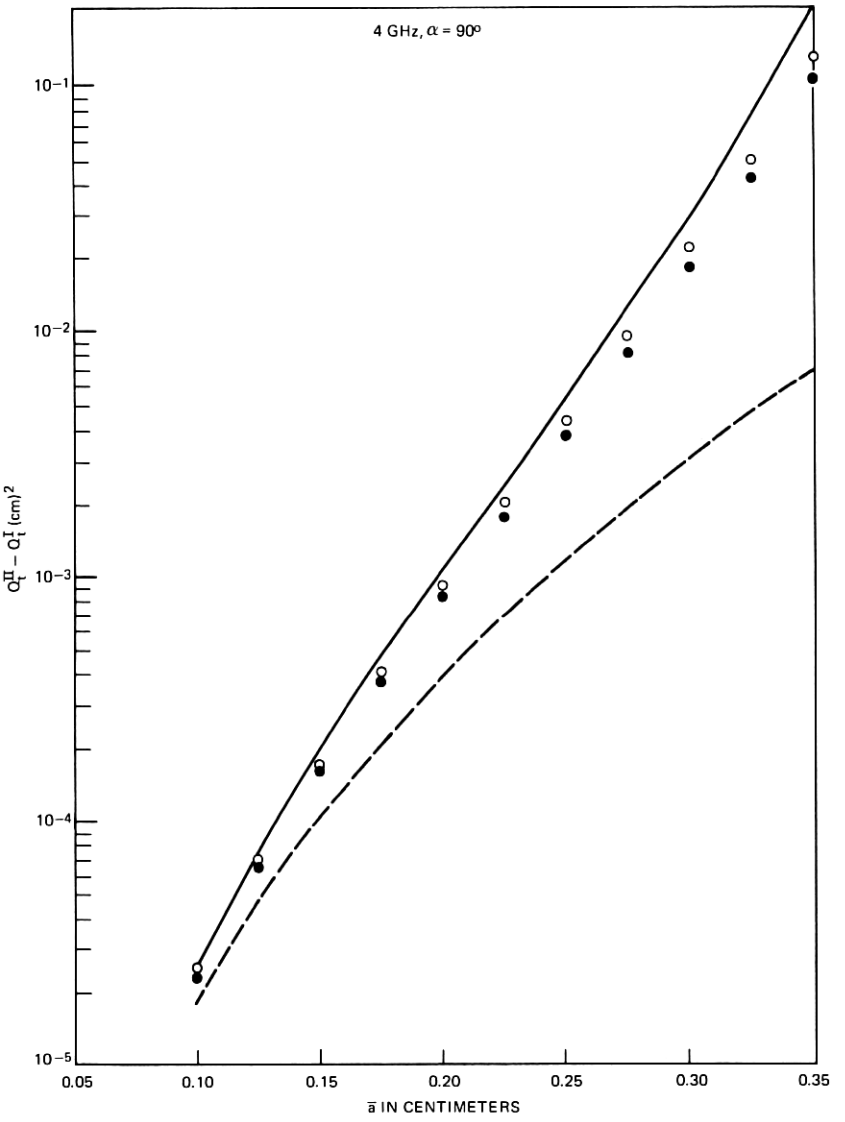

Fig. 15—Comparison of perturbation approximations to the least-squares-fitting value of $Q_t^{II} - Q_t^I$ at 4 GHz with $\alpha = 90°$ as a function of drop size.

sizes. For $\bar{a} = 0.3$, he gives $f^h \times 10^3 = 0.06470 - 4.709i$, which is in fact quite close to our value, but he also gives $f^v \times 10^3 = 0.9100 - 3.726i$, with real part differing by almost 1 percent from our value.

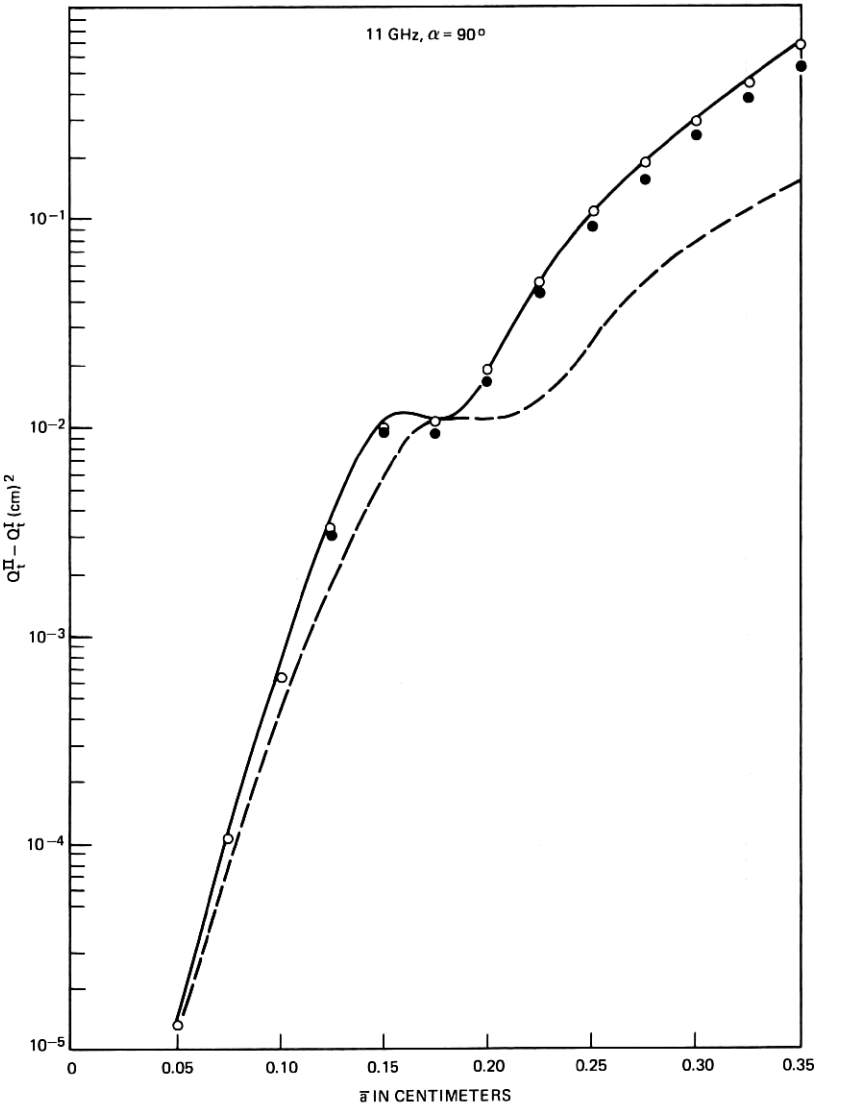

Fig. 16—Comparison of perturbation approximations to the least-squares-fitting value of $Q_t^{II} - Q_t^I$ at 11 GHz with $\alpha = 90°$ as a function of drop size.

VIII. PERTURBATION RESULTS

In this final section, we compare three sets of first-order perturbation results with those obtained by least-squares fitting. The comparisons are made graphically in Figs. 3 to 23, since this is much more revealing than tabulating the results. The solid curves correspond to least-squares fitting and the dashed curves to perturbation about the inscribed sphere of radius a, corresponding to the expansion in (63), with perturbation parameter ν given by (64). The circles and dots correspond to perturbation about the equivolumic sphere of radius $\bar{a}$, with perturbation parameters $\bar{\nu} = 2\bar{a}$ and ν, respectively, corresponding to the expansions in (65). The dots have been omitted in those cases in which they would lie very close to the corresponding circle or solid curve. Comparisons are made for $\alpha = 90°$ at 4, 11, 18.1, and 30 GHz and for $\alpha = 50°$ at 30 GHz.

The real parts of the forward scattering amplitudes $S_{\mathrm{I}}(0)$ and $S_{\mathrm{II}}(0)$ and the first-order approximations to these quantities are depicted in

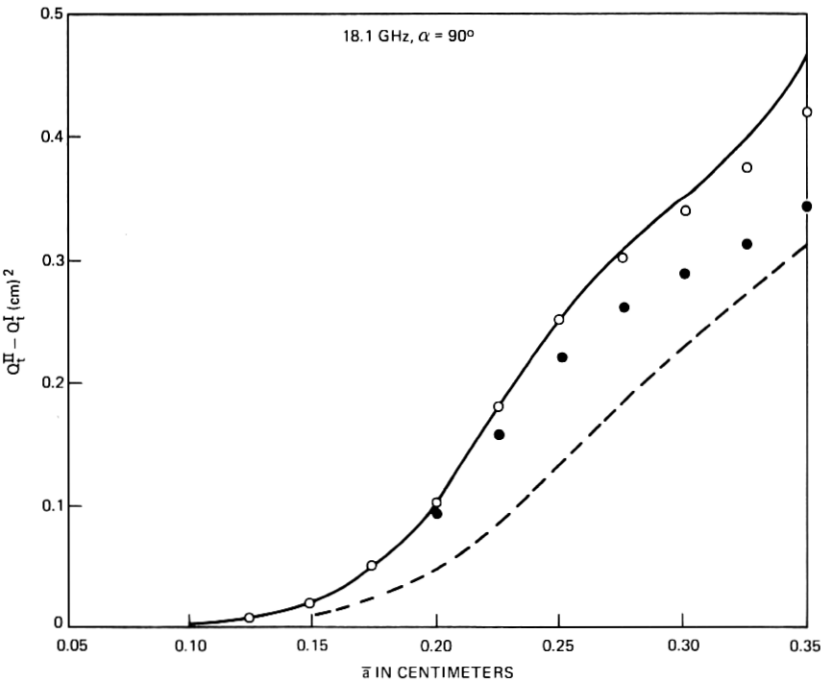

Fig. 17—Comparison of perturbation approximations to the least-squares-fitting value of $Q^{\mathrm{II}} - Q_t^{\mathrm{I}}$ at 18.1 GHz with $\alpha = 90°$ as a function of drop size.

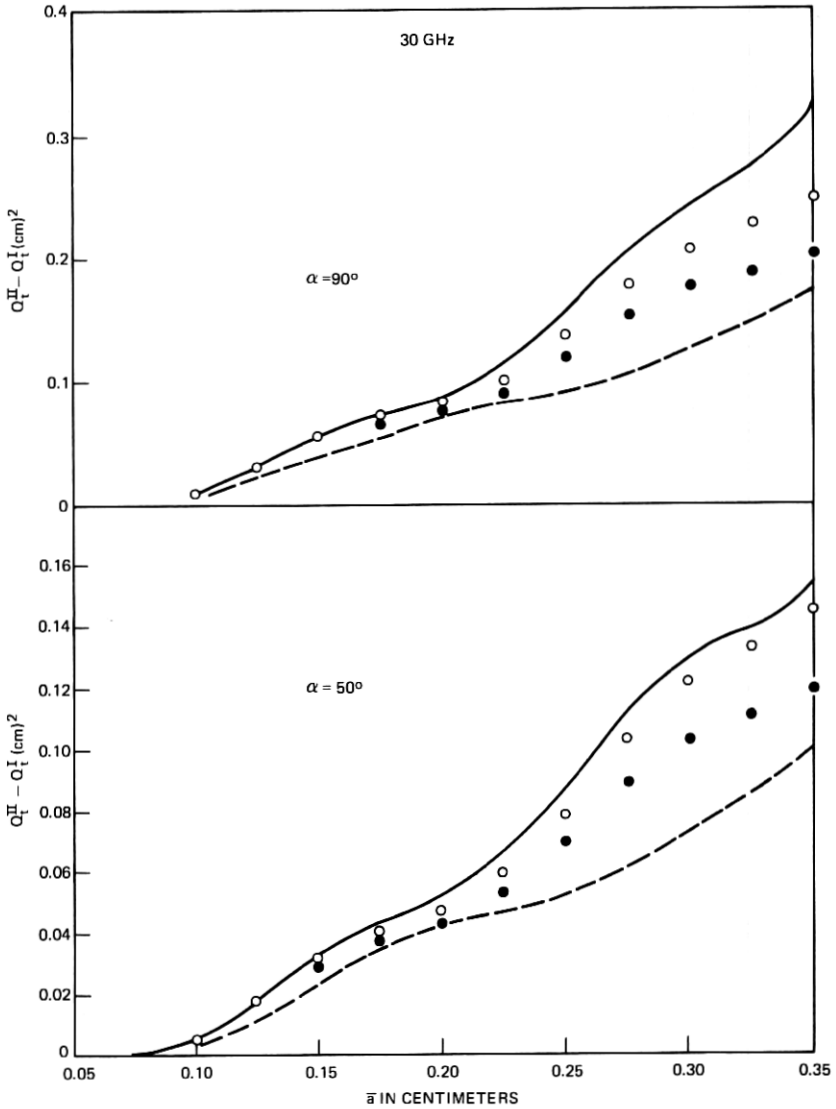

Fig. 18—Comparison of perturbation approximations to the least-squares-fitting value of $Q_t^{II} - Q_t^I$ at 30 GHz with $\alpha = 90°$ and $\alpha = 50°$ as a function of drop size.

Figs. 3 to 9, while the imaginary parts are depicted in Figs. 10 to 14. It should be noted that a logarithmic scale has been used in Figs. 3 and 4. Thus, at 4 GHz the first-order approximation to the real part of

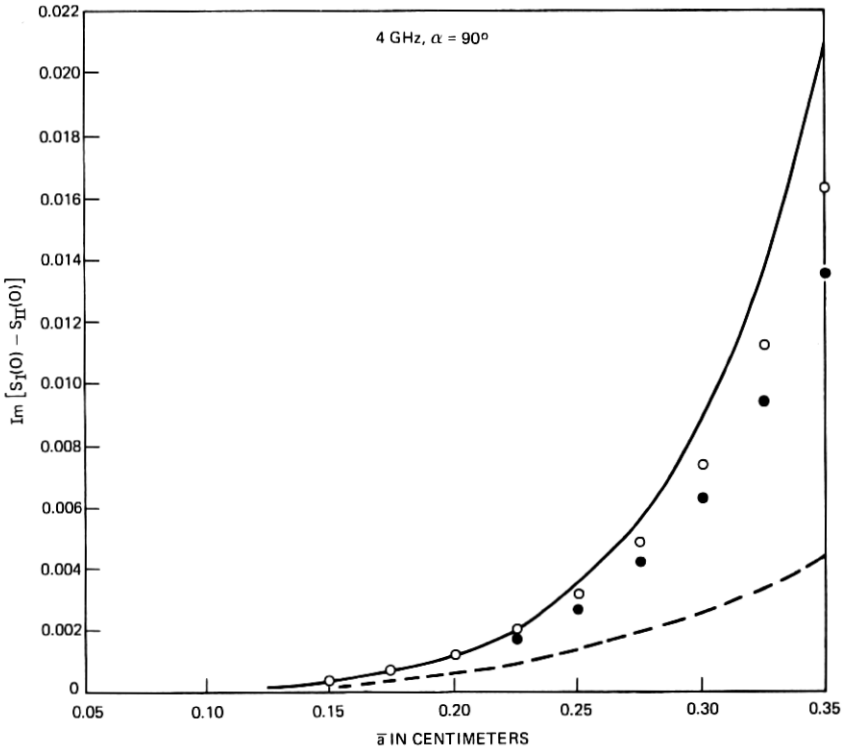

Fig. 19—Comparison of perturbation approximations to the least-squares-fitting value of $\mathrm{Im}[S_I(0) - S_{II}(0)]$ at 4 GHz with $\alpha = 90°$ as a function of drop size.

$S_{II}(0)$, obtained by perturbing about the inscribed sphere, is in error by an order of magnitude for the largest drop size. It is seen that the best overall approximation is obtained by perturbing about the equivolumic sphere with perturbation parameter $\bar{\nu} = 2\bar{a}$, and in most cases there is a significant improvement over the approximation obtained by perturbing about the inscribed sphere as Oguchi[4] did. The second best overall approximation is obtained by perturbing about the equivolumic sphere with perturbation parameter $\nu = \bar{a}(2 - \bar{a})$, and is generally much better than the approximation obtained by perturbing about the inscribed sphere. The above ordering of the three sets of perturbation results is consistent with the order of the geometrical errors in the corresponding approximations in (63) and (65) to the oblate spheroid.

Although the comparison is not depicted for some of the smallest drop sizes, all three approximations are good for these, since the ec-

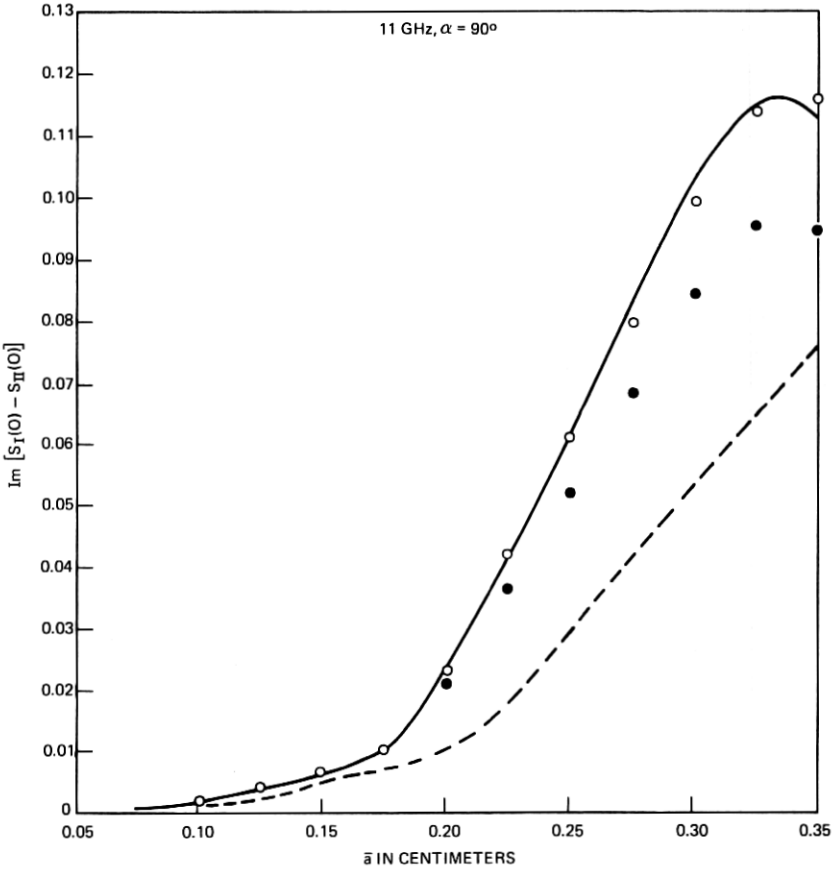

Fig. 20—Comparison of perturbation approximations to the least-squares-fitting value of $\mathrm{Im}[S_{\mathrm{I}}(0) - S_{\mathrm{II}}(0)]$ at 11 GHz with $\alpha = 90°$ as a function of drop size.

centricity is small. On the other hand, the approximations obtained by perturbing about the equivolumic sphere are remarkably good for the largest drop sizes, in view of the fact that neither the eccentricity nor the perturbation parameter is small. In particular, these approximations to the imaginary part of $S_{\mathrm{II}}(0)$, depicted in Figs. 10 to 14, are quite impressive. It is not too surprising that perturbing about the inscribed sphere leads to poor results for the larger drop sizes in the second polarization. The first-order approximations to the scattering cross sections Q_s^{I} and Q_s^{II} are very similar to those depicted in Figs. 3 to 9 for the real parts of $S_{\mathrm{I}}(0)$ and $S_{\mathrm{II}}(0)$, which are related to the total cross sections Q_t^{I} and Q_t^{II} by (39).

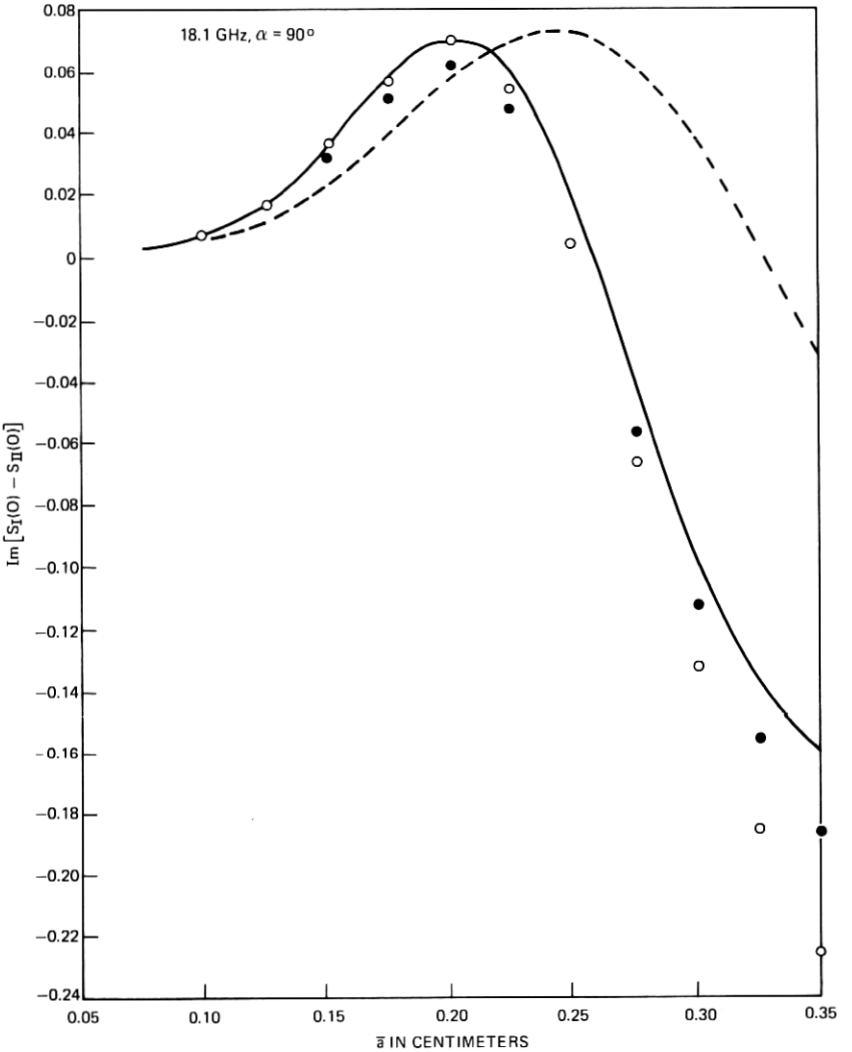

Fig. 21—Comparison of perturbation approximations to the least-squares-fitting value of $\mathrm{Im}[S_{\mathrm{I}}(0) - S_{\mathrm{II}}(0)]$ at 18.1 GHz with $\alpha = 90°$ as a function of drop size.

For purposes of comparison, the values of the forward scattering amplitude $S(0)$ and the total and scattering cross sections Q_t and Q_s for the equivolumic spherical drops are given in Tables XIV to XVII. These quantities do not depend on the polarization of the incident wave or on the angle of incidence α. As is seen from Tables VIII to XIII,

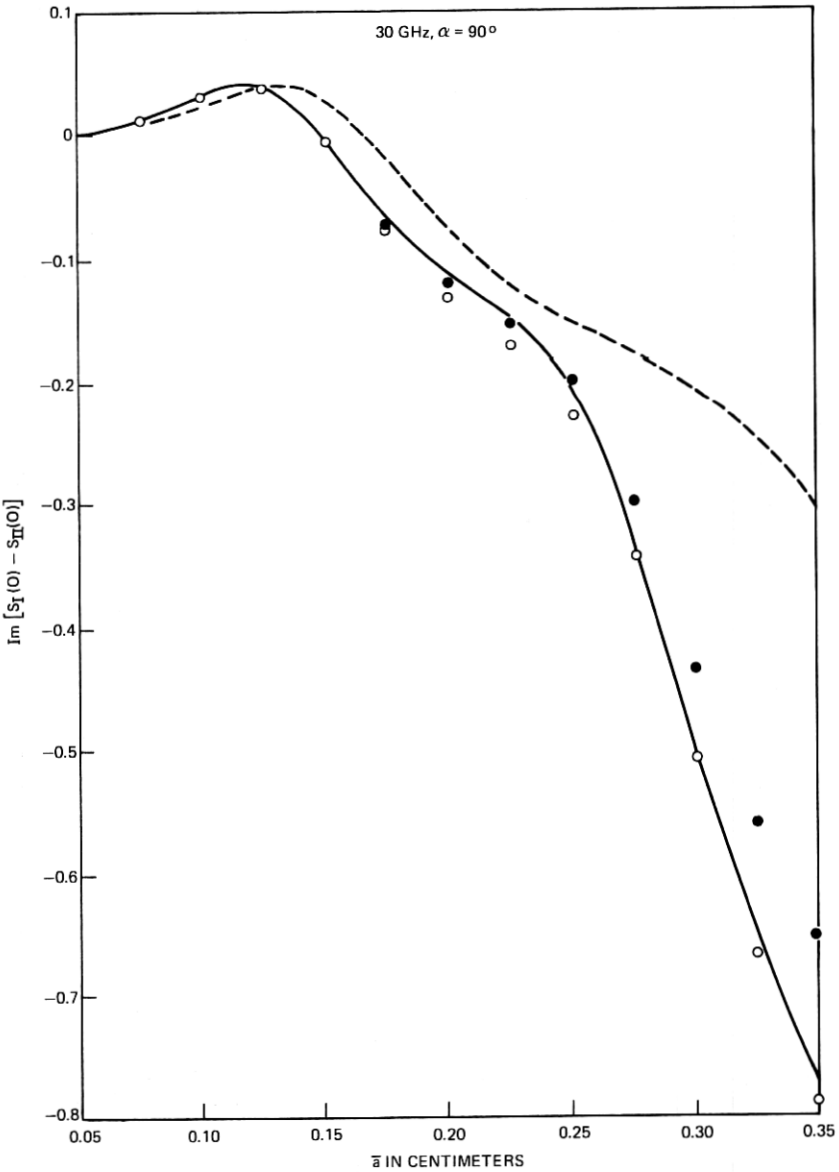

Fig. 22—Comparison of perturbation approximations to the least-squares-fitting value of $\mathrm{Im}[S_I(0) - S_{II}(0)]$ at 30 GHz with $\alpha = 90°$ as a function of drop size.

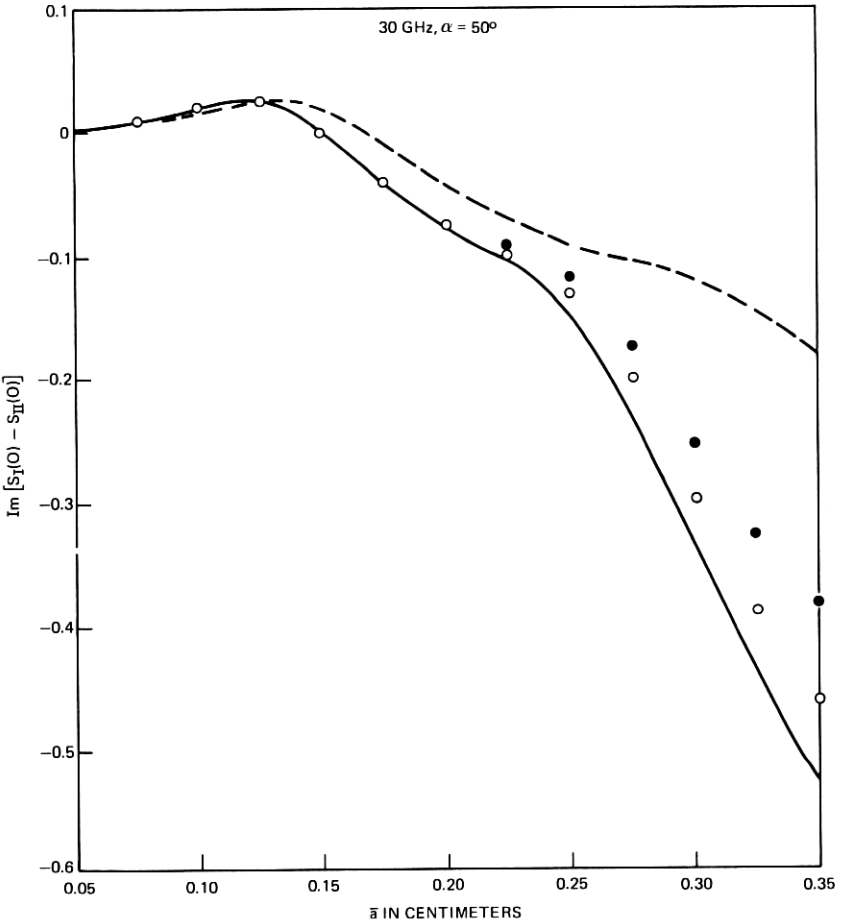

Fig. 23—Comparison of perturbation approximations to the least-squares-fitting value of $\mathrm{Im}[S_{\mathrm{I}}(0) - S_{\mathrm{II}}(0)]$ at 30 GHz with $\alpha = 50°$ as a function of drop size.

the value of Q_t lies between the corresponding values for the two polarizations for the oblate spheroidal drop of the same size and similarly for the value of Q_s. Although this happens to be true at 30 GHz for $\alpha = 90°$, 70°, and 50°, these relations should not be expected to hold for all values of α, since for $\alpha = 0°$ the cross sections are independent of the polarization because of the axial symmetry of the oblate spheroidal drop. We have verified that $Q_t \neq Q_t^{\mathrm{I}} = Q_t^{\mathrm{II}}$ and $Q_s \neq Q_s^{\mathrm{I}} = Q_s^{\mathrm{II}}$ for $\alpha = 0°$ at 11 GHz, for $\bar{a} = 0\ 025$, 0.1, and 0.175.

The rain-induced differential attenuation and differential phase

Table XIV — Forward scattering amplitude and total and scattering cross sections for the equivolumic spherical drop at 4 GHz for different drop sizes

$\bar{a}$(cm)	$S(0)$	Q_t(cm)^2	Q_s(cm)^2
0.025	$7.1886 \times 10^{-8} - 8.8610 \times 10^{-6}i$	1.2871×10^{-6}	9.3508×10^{-10}
0.05	$6.3247 \times 10^{-7} - 7.1195 \times 10^{-5}i$	1.1324×10^{-5}	5.9937×10^{-8}
0.075	$2.4837 \times 10^{-6} - 2.4204 \times 10^{-4}i$	4.4470×10^{-5}	6.8450×10^{-7}
0.1	$7.1665 \times 10^{-6} - 5.7975 \times 10^{-4}i$	1.2832×10^{-4}	3.8606×10^{-6}
0.125	$1.7619 \times 10^{-5} - 1.1481 \times 10^{-3}i$	3.1547×10^{-4}	1.4804×10^{-5}
0.15	$3.9266 \times 10^{-5} - 2.0191 \times 10^{-3}i$	7.0305×10^{-4}	4.4509×10^{-5}
0.175	$8.1912 \times 10^{-5} - 3.2771 \times 10^{-3}i$	1.4666×10^{-3}	1.1325×10^{-4}
0.2	$1.6324 \times 10^{-4} - 5.0244 \times 10^{-3}i$	2.9228×10^{-3}	2.5537×10^{-4}
0.225	$3.1562 \times 10^{-4} - 7.3913 \times 10^{-3}i$	5.6511×10^{-3}	5.2608×10^{-4}
0.25	$6.0030 \times 10^{-4} - 1.0551 \times 10^{-2}i$	1.0748×10^{-2}	1.0123×10^{-3}
0.275	$1.1392 \times 10^{-3} - 1.4745 \times 10^{-2}i$	2.0397×10^{-2}	1.8527×10^{-3}
0.3	$2.1916 \times 10^{-3} - 2.0322 \times 10^{-2}i$	3.9240×10^{-2}	3.2838×10^{-3}
0.325	$4.3555 \times 10^{-3} - 2.7783 \times 10^{-2}i$	7.7985×10^{-2}	5.7649×10^{-3}
0.35	$9.1208 \times 10^{-3} - 3.7683 \times 10^{-2}i$	1.6331×10^{-1}	1.0372×10^{-2}

shift are obtained[1] by summing the real and imaginary parts of $S_{II}(0) - S_I(0)$ over the Laws and Parsons drop-size distribution.[7] In a recent short note,[9] the three first-order perturbation approximations have been compared to the least-squares fitting results for the differential attenuation and differential phase shift at several different rain rates. The same ordering of the overall closeness of the three approximations holds for these quantities. Since the perturbation results are obtained quite inexpensively whereas the least-squares-fitting procedure is very costly, approximations to the differential attenuation and differential phase shift at frequencies up to 100 GHz were obtained by per-

Table XV — Forward scattering amplitude and total and scattering cross sections for the equivolumic spherical drop at 11 GHz for different drop sizes

$\bar{a}$(cm)	$S(0)$	Q_t(cm)^2	Q_s(cm)^2
0.025	$4.9868 \times 10^{-6} - 1.8550 \times 10^{-4}i$	1.1804×10^{-5}	5.3599×10^{-8}
0.05	$6.2648 \times 10^{-5} - 1.5238 \times 10^{-3}i$	1.4829×10^{-4}	3.4733×10^{-6}
0.075	$3.8512 \times 10^{-4} - 5.3789 \times 10^{-3}i$	9.1163×10^{-4}	4.0552×10^{-5}
0.1	$1.7992 \times 10^{-3} - 1.3547 \times 10^{-2}i$	4.2588×10^{-3}	2.3883×10^{-4}
0.125	$7.1756 \times 10^{-3} - 2.7813 \times 10^{-2}i$	1.6985×10^{-2}	1.0004×10^{-3}
0.15	$2.2023 \times 10^{-2} - 4.4760 \times 10^{-2}i$	5.2132×10^{-2}	3.4809×10^{-3}
0.175	$3.9051 \times 10^{-2} - 5.5463 \times 10^{-2}i$	9.2438×10^{-2}	9.7067×10^{-3}
0.2	$5.0153 \times 10^{-2} - 7.3383 \times 10^{-2}i$	1.1872×10^{-1}	2.1692×10^{-2}
0.225	$6.8317 \times 10^{-2} - 1.0343 \times 10^{-1}i$	1.6171×10^{-1}	4.2294×10^{-2}
0.25	$9.6583 \times 10^{-2} - 1.3932 \times 10^{-1}i$	2.2862×10^{-1}	7.4229×10^{-2}
0.275	$1.3508 \times 10^{-1} - 1.8178 \times 10^{-1}i$	3.1976×10^{-1}	1.2397×10^{-1}
0.3	$1.8972 \times 10^{-1} - 2.2945 \times 10^{-1}i$	4.4910×10^{-1}	2.0165×10^{-1}
0.325	$2.6372 \times 10^{-1} - 2.7484 \times 10^{-1}i$	6.2427×10^{-1}	3.1470×10^{-1}
0.35	$3.5439 \times 10^{-1} - 3.1001 \times 10^{-1}i$	8.3887×10^{-1}	4.6135×10^{-1}

Table XVI — Forward scattering amplitude and total and scattering cross sections for the equivolumic spherical drop at 18.1 GHz for different drop sizes

$\bar{a}$(cm)	$S(0)$	Q_t(cm)^2	Q_s(cm)^2
0.025	$4.1444 \times 10^{-5} - 8.3170 \times 10^{-4}i$	3.6243×10^{-5}	3.9388×10^{-7}
0.05	$6.8431 \times 10^{-4} - 6.9938 \times 10^{-3}i$	5.9843×10^{-4}	2.6138×10^{-5}
0.075	$5.3548 \times 10^{-3} - 2.4905 \times 10^{-2}i$	4.6827×10^{-3}	3.2305×10^{-4}
0.1	$2.4004 \times 10^{-2} - 5.5611 \times 10^{-2}i$	2.0991×10^{-2}	2.0935×10^{-3}
0.125	$5.4019 \times 10^{-2} - 9.1780 \times 10^{-2}i$	4.7240×10^{-2}	8.8579×10^{-3}
0.15	$9.7706 \times 10^{-2} - 1.4719 \times 10^{-1}i$	8.5444×10^{-2}	2.6617×10^{-2}
0.175	$1.7343 \times 10^{-1} - 2.1684 \times 10^{-1}i$	1.5166×10^{-1}	6.2646×10^{-2}
0.2	$2.8868 \times 10^{-1} - 2.8757 \times 10^{-1}i$	2.5245×10^{-1}	1.2552×10^{-1}
0.225	$4.4398 \times 10^{-1} - 3.3858 \times 10^{-1}i$	3.8826×10^{-1}	2.1846×10^{-1}
0.25	$6.1859 \times 10^{-1} - 3.5216 \times 10^{-1}i$	5.4095×10^{-1}	3.2834×10^{-1}
0.275	$7.8546 \times 10^{-1} - 3.3543 \times 10^{-1}i$	6.8688×10^{-1}	4.3596×10^{-1}
0.3	$9.3560 \times 10^{-1} - 3.0993 \times 10^{-1}i$	8.1818×10^{-1}	5.3377×10^{-1}
0.325	$1.0751 - 2.9126 \times 10^{-1}i$	9.4019×10^{-1}	6.2372×10^{-1}
0.35	$1.2136 - 2.8673 \times 10^{-1}i$	1.0613	7.1027×10^{-1}

turbing about the equivolumic sphere. However, the results may be less reliable at the higher frequencies, particularly at the heavier rain rates.[18]

The difference $Q_t^{\mathrm{II}} - Q_t^{\mathrm{I}}$, which is related to the real part of $S_{\mathrm{II}}(0) - S_{\mathrm{I}}(0)$ by (39), is depicted in Figs. 15 to 18, and the imaginary part of $S_{\mathrm{I}}(0) - S_{\mathrm{II}}(0)$ is depicted in Figs. 19 to 23. We note that, although extra first-order correction terms arise in the expansions about the equivolumic sphere given in (65), they correspond to a constant change in the radius of the drop. Hence, the corresponding increments in the forward scattering amplitudes are the same for both polarizations, and

Table XVII — Forward scattering amplitude and total and scattering cross sections for the equivolumic spherical drop at 30 GHz for different drop sizes

$\bar{a}$(cm)	$S(0)$	Q_t(cm)^2	Q_s(cm)^2
0.025	$3.5549 \times 10^{-4} - 3.8212 \times 10^{-3}i$	1.1316×10^{-4}	2.9980×10^{-6}
0.05	$7.2950 \times 10^{-3} - 3.2466 \times 10^{-2}i$	2.3221×10^{-3}	2.1254×10^{-4}
0.075	$4.8577 \times 10^{-2} - 1.0204 \times 10^{-1}i$	1.5463×10^{-2}	2.8859×10^{-3}
0.1	$1.5024 \times 10^{-1} - 2.0855 \times 10^{-1}i$	4.7823×10^{-2}	1.7391×10^{-2}
0.125	$3.5560 \times 10^{-1} - 3.1825 \times 10^{-1}i$	1.1319×10^{-1}	5.6317×10^{-2}
0.15	$6.3545 \times 10^{-1} - 3.5742 \times 10^{-1}i$	2.0227×10^{-1}	1.1723×10^{-1}
0.175	$9.0831 \times 10^{-1} - 3.2571 \times 10^{-1}i$	2.8913×10^{-1}	1.8042×10^{-1}
0.2	$1.1444 - 2.9371 \times 10^{-1}i$	3.6426×10^{-1}	2.3403×10^{-1}
0.225	$1.3868 - 3.0778 \times 10^{-1}i$	4.4142×10^{-1}	2.8578×10^{-1}
0.25	$1.6859 - 3.5609 \times 10^{-1}i$	5.3662×10^{-1}	3.4813×10^{-1}
0.275	$2.0559 - 3.9425 \times 10^{-1}i$	6.5441×10^{-1}	4.2750×10^{-1}
0.3	$2.4657 - 3.9064 \times 10^{-1}i$	7.8486×10^{-1}	5.1929×10^{-1}
0.325	$2.8763 - 3.5872 \times 10^{-1}i$	9.1557×10^{-1}	6.1372×10^{-1}
0.35	$3.2831 - 3.3474 \times 10^{-1}i$	1.0450	7.0680×10^{-1}

therefore do not affect the difference $S_{II}(0) - S_I(0)$. Figures 15 to 23 show that the approximations to the differential quantities obtained by perturbing about the equivolumic sphere with perturbation parameter $\bar{\nu} = 2\bar{a}$ are overall remarkably close to the least-squares-fitting results and far better than the approximations obtained by perturbing about the inscribed sphere.

IX. ACKNOWLEDGMENTS

The authors are indebted to D. C. Hogg for bringing this problem to their attention, to T. S. Chu for some helpful discussions, to J. McKenna and N. L. Schryer for suggesting the matching and least-squares-fitting approaches and for several helpful discussions in relation to these, and to P. A. Businger, whose least-squares-fitting subroutine was incorporated into the main program. The authors are greatly indebted to Mary Ann Gatto, who took over the burdensome task of running the main program, set up the transfer of data onto a disc file, and made some other program modifications, and to Susan Hoffberg who wrote the programs for calculating the first-order perturbation approximations and carefully checked some special function routines against tables. The authors are grateful to T. Oguchi for his private communications and for making available at an early date a preprint of his detailed paper.[35] Finally, the authors are particularly indebted to T. S. Chu, D. C. Hogg, and J. McKenna for their continued encouragement throughout the lengthy course of this work.

APPENDIX A

We first derive the expansion of the incident plane wave in a Fourier series in the azimuthal angle φ, as given by (20). The unit vectors in Cartesian coordinates are given in terms of those in spherical coordinates by

$$\begin{aligned} \mathbf{i} &= \sin\theta\cos\varphi\mathbf{i}_1 + \cos\theta\cos\varphi\mathbf{i}_2 - \sin\varphi\mathbf{i}_3, \\ \mathbf{j} &= \sin\theta\sin\varphi\mathbf{i}_1 + \cos\theta\sin\varphi\mathbf{i}_2 + \cos\varphi\mathbf{i}_3, \end{aligned}$$

and

$$\mathbf{k} = \cos\theta\mathbf{i}_1 - \sin\theta\mathbf{i}_2. \tag{76}$$

Also, we have

$$x\sin\alpha + z\cos\alpha = r(\sin\alpha\sin\theta\cos\varphi + \cos\alpha\cos\theta). \tag{77}$$

But[36] for integer values of p,

$$\frac{1}{2\pi}\int_0^{2\pi} e^{-ip\varphi}\exp(i\xi\cos\varphi)d\varphi = i^p J_p(\xi), \tag{78}$$

where J_p denotes the regular Bessel function (of the first kind) of order p.

It follows, from (5), (6), (20) to (22), and (76) to (78), using the recurrence relations for the Bessel functions,[37] that

$$\mathbf{f}_m(r,\theta) = i^m \exp(ik_0 r\cos\alpha\cos\theta)\Big[J_m(k_0 r\sin\alpha\sin\theta)\sin\alpha \times(\sin\theta\mathbf{i}_2 - \cos\theta\mathbf{i}_1) - iJ'_m(k_0 r\sin\alpha\sin\theta)\cos\alpha(\sin\theta\mathbf{i}_1 + \cos\theta\mathbf{i}_2) + \frac{mJ_m(k_0 r\sin\alpha\sin\theta)}{k_0 r\sin\alpha\sin\theta}\cos\alpha\mathbf{i}_3\Big] \quad (79)$$

and

$$\mathbf{g}_m(r,\theta) = -i^m \exp(ik_0 r\cos\alpha\cos\theta)\Big[\frac{mJ_m(k_0 r\sin\alpha\sin\theta)}{k_0 r\sin\alpha\sin\theta} \times(\sin\theta\mathbf{i}_1 + \cos\theta\mathbf{i}_2) + iJ'_m(k_0 r\sin\alpha\sin\theta)\mathbf{i}_3\Big], \quad (80)$$

where, as before, the prime denotes derivative with respect to the argument.

From (8) to (11), (13), (14), and (20), the boundary conditions (16) and (17), when multiplied by $e^{-im\varphi}$ and integrated with respect to φ from 0 to 2π, lead to the equations

$$e_{m3}(R,\theta) + \sum_{\substack{n\geqq|m|\\ n\neq 0}} a_{mn}h_n^{(1)}(k_0R)\frac{dP_n^{|m|}(\cos\theta)}{d\theta} - \sum_{\substack{n\geqq|m|\\ n\neq 0}} b_{mn}\Big[\frac{h_n^{(1)}(k_0R)}{k_0R} + h_n^{(1)'}(k_0R)\Big]\cdot\frac{im}{\sin\theta}P_n^{|m|}(\cos\theta) = \sum_{\substack{n\geqq|m|\\ n\neq 0}} c_{mn}j_n(k_1R)\frac{dP_n^{|m|}(\cos\theta)}{d\theta} - \sum_{\substack{n\geqq|m|\\ n\neq 0}} d_{mn}\Big[\frac{j_n(k_1R)}{k_1R} + j'_n(k_1R)\Big]\cdot\frac{im}{\sin\theta}P_n^{|m|}(\cos\theta) \quad (81)$$

and, using (4),

$$\frac{i\omega\mu_0}{k_0}h_{m3}(R,\theta) + \sum_{\substack{n\geqq|m|\\ n\neq 0}} b_{mn}h_n^{(1)}(k_0R)\frac{dP_n^{|m|}(\cos\theta)}{d\theta} - \sum_{\substack{n\geqq|m|\\ n\neq 0}} a_{mn}\Big[\frac{h_n^{(1)}(k_0R)}{k_0R} + h_n^{(1)'}(k_0R)\Big]\cdot\frac{im}{\sin\theta}P_n^{|m|}(\cos\theta) = N\sum_{\substack{n\geqq|m|\\ n\neq 0}} d_{mn}j_n(k_1R)\frac{dP_n^{|m|}(\cos\theta)}{d\theta} - N\sum_{\substack{n\geqq|m|\\ n\neq 0}} c_{mn}\Big[\frac{j_n(k_1R)}{k_1R} + j'_n(k_1R)\Big]\cdot\frac{im}{\sin\theta}P_n^{|m|}(\cos\theta). \quad (82)$$

We are using the notations $e_{mj} = \mathbf{e}_m\cdot\mathbf{i}_j$ and $h_{mj} = \mathbf{h}_m\cdot\mathbf{i}_j$.

Similarly, the boundary conditions (18) and (19) lead to the equations

$$e_{m2}(R,\theta) + \frac{1}{R}\frac{dR}{d\theta}\, e_{m1}(R,\theta) - \sum_{\substack{n \geqq |m| \\ n \neq 0}} a_{mn} h_n^{(1)}(k_0 R) \cdot \frac{im}{\sin\theta} P_n^{|m|}(\cos\theta)$$
$$- \sum_{\substack{n \geqq |m| \\ n \neq 0}} b_{mn} \left\{ \left[\frac{h_n^{(1)}(k_0 R)}{k_0 R} + h_n^{(1)'}(k_0 R) \right] \frac{dP_n^{|m|}(\cos\theta)}{d\theta} \right.$$
$$\left. + \frac{n(n+1)}{R} \frac{dR}{d\theta} \frac{h_n^{(1)}(k_0 R)}{k_0 R} P_n^{|m|}(\cos\theta) \right\}$$
$$= - \sum_{\substack{n \geqq |m| \\ n \neq 0}} c_{mn} j_n(k_1 R) \cdot \frac{im}{\sin\theta} P_n^{|m|}(\cos\theta)$$
$$- \sum_{\substack{n \geqq |m| \\ n \neq 0}} d_{mn} \left\{ \left[\frac{j_n(k_1 R)}{k_1 R} + j_n'(k_1 R) \right] \frac{dP_n^{|m|}(\cos\theta)}{d\theta} \right.$$
$$\left. + \frac{n(n+1)}{R} \frac{dR}{d\theta} \frac{j_n(k_1 R)}{k_1 R} P_n^{|m|}(\cos\theta) \right\} \quad (83)$$

and

$$\frac{i\omega\mu_0}{k_0} \left[h_{m2}(R,\theta) + \frac{1}{R}\frac{dR}{d\theta} h_{m1}(R,\theta) \right]$$
$$- \sum_{\substack{n \geqq |m| \\ n \neq 0}} b_{mn} h_n^{(1)}(k_0 R) \cdot \frac{im}{\sin\theta} P_n^{|m|}(\cos\theta)$$
$$- \sum_{\substack{n \geqq |m| \\ n \neq 0}} a_{mn} \left\{ \left[\frac{h_n^{(1)}(k_0 R)}{k_0 R} + h_n^{(1)'}(k_0 R) \right] \frac{dP_n^{|m|}(\cos\theta)}{d\theta} \right.$$
$$\left. + \frac{n(n+1)}{R} \frac{dR}{d\theta} \frac{h_n^{(1)}(k_0 R)}{k_0 R} P_n^{|m|}(\cos\theta) \right\}$$
$$= - N \sum_{\substack{n \geqq |m| \\ n \neq 0}} d_{mn} j_n(k_1 R) \cdot \frac{im}{\sin\theta} P_n^{|m|}(\cos\theta)$$
$$- N \sum_{\substack{n \geqq |m| \\ n \neq 0}} c_{mn} \left\{ \left[\frac{j_n(k_1 R)}{k_1 R} + j_n'(k_1 R) \right] \frac{dP_n^{|m|}(\cos\theta)}{d\theta} \right.$$
$$\left. + \frac{n(n+1)}{R} \frac{dR}{d\theta} \frac{j_n(k_1 R)}{k_1 R} P_n^{|m|}(\cos\theta) \right\}. \quad (84)$$

APPENDIX B

We consider here the case in which the raindrop is symmetrical about the plane $\theta = \pi/2$ so that

$$R(\pi - \theta) = R(\theta), \qquad 0 \leqq \theta \leqq \pi/2. \quad (85)$$

Let $\hat{\alpha} = (\pi - \alpha)$. Then, from (21), (79), and (80), it follows that, cor-

responding to $\hat{\alpha}$,

$$\hat{e}^{\mathrm{I}}_{m3}(R, \theta) = -e^{\mathrm{I}}_{m3}(R, \pi - \theta), \tag{86}$$

$$\hat{h}^{\mathrm{I}}_{m3}(R, \theta) = h^{\mathrm{I}}_{m3}(R, \pi - \theta), \tag{87}$$

$$\left[\hat{e}^{\mathrm{I}}_{m2}(R, \theta) + \frac{1}{R}\frac{dR}{d\theta}\hat{e}_{m1}(R, \theta)\right] = \left[e^{\mathrm{I}}_{m2}(R, \pi - \theta) + \frac{1}{R}\frac{dR(\pi - \theta)}{d(\pi - \theta)}e^{\mathrm{I}}_{m1}(R, \pi - \theta)\right], \tag{88}$$

and

$$\left[\hat{h}^{\mathrm{I}}_{m2}(R, \theta) + \frac{1}{R}\frac{dR}{d\theta}\hat{h}^{\mathrm{I}}_{m1}(R, \theta)\right] = -\left[h^{\mathrm{I}}_{m2}(R, \pi - \theta) + \frac{1}{R}\frac{dR(\pi - \theta)}{d(\pi - \theta)}h^{\mathrm{I}}_{m1}(R, \pi - \theta)\right]. \tag{89}$$

But[14]

$$P^{|m|}_n(-\cos\theta) = (-1)^{n+|m|}P^{|m|}_n(\cos\theta). \tag{90}$$

It follows from (81) to (90) that

$$a^{\mathrm{I}}_{mn} + (-1)^{n+|m|+1}\hat{a}^{\mathrm{I}}_{mn} = 0, \qquad c^{\mathrm{I}}_{mn} + (-1)^{n+|m|+1}\hat{c}^{\mathrm{I}}_{mn} = 0 \tag{91}$$

and

$$b^{\mathrm{I}}_{mn} + (-1)^{n+|m|}\hat{b}^{\mathrm{I}}_{mn} = 0, \qquad d^{\mathrm{I}}_{mn} + (-1)^{n+|m|}\hat{d}^{\mathrm{I}}_{mn} = 0. \tag{92}$$

For $\alpha = \pi/2$, we have $\hat{\alpha} = \alpha$, and hence we obtain the relationships in (25).

Similarly, from (22), (79), and (80),

$$\hat{e}^{\mathrm{II}}_{m3}(R, \theta) = e^{\mathrm{II}}_{m3}(R, \pi - \theta), \tag{93}$$

$$\hat{h}^{\mathrm{II}}_{m3}(R, \theta) = -h^{\mathrm{II}}_{m3}(R, \pi - \theta), \tag{94}$$

$$\left[\hat{e}^{\mathrm{II}}_{m2}(R, \theta) + \frac{1}{R}\frac{dR}{d\theta}\hat{e}^{\mathrm{II}}_{m1}(R, \theta)\right] = -\left[e^{\mathrm{II}}_{m2}(R, \pi - \theta) + \frac{1}{R}\frac{dR(\pi - \theta)}{d(\pi - \theta)}e^{\mathrm{II}}_{m1}(R, \pi - \theta)\right], \tag{95}$$

and

$$\left[\hat{h}^{\mathrm{II}}_{m2}(R, \theta) + \frac{1}{R}\frac{dR}{d\theta}\hat{h}^{\mathrm{II}}_{m1}(R, \theta)\right] = \left[h^{\mathrm{II}}_{m2}(R, \pi - \theta) + \frac{1}{R}\frac{dR(\pi - \theta)}{d(\pi - \theta)}h^{\mathrm{II}}_{m1}(R, \pi - \theta)\right]. \tag{96}$$

It follows, from (81) to (85), (90), and (93) to (96), that

$$a_{mn}^{\mathrm{II}} + (-1)^{n+|m|}\hat{a}_{mn}^{\mathrm{II}} = 0, \qquad c_{mn}^{\mathrm{II}} + (-1)^{n+|m|}\hat{c}_{mn}^{\mathrm{II}} = 0 \quad (97)$$

and

$$b_{mn}^{\mathrm{II}} + (-1)^{n+|m|+1}\hat{b}_{mn}^{\mathrm{II}} = 0, \qquad d_{mn}^{\mathrm{II}} + (-1)^{n+|m|+1}\hat{d}_{mn}^{\mathrm{II}} = 0. \quad (98)$$

For $\alpha = \pi/2$ we obtain the relationships in (26).

For $\alpha \neq \pi/2$ we may consider the sum and the difference of the boundary conditions corresponding to α and to $\hat{\alpha} = (\pi - \alpha)$. Then the sums $(a_{mn} + \hat{a}_{mn})$, $(b_{mn} + \hat{b}_{mn})$, $(c_{mn} + \hat{c}_{mn})$, and $(d_{mn} + \hat{d}_{mn})$ and the differences $(a_{mn} - \hat{a}_{mn})$, $(b_{mn} - \hat{b}_{mn})$, $(c_{mn} - \hat{c}_{mn})$, and $(d_{mn} - \hat{d}_{mn})$ may be determined separately, and these sums and differences vanish for alternate values of n, depending on the polarization.

APPENDIX C

We first consider the calculation of the scattered energy W_s, which is defined by (35), by letting $r \to \infty$. From (29) it follows that

$$W_s = \lim_{r\to\infty} \left\{ \frac{k_0 r^2}{2\omega\mu_0} \int_0^{2\pi} \int_0^{\pi} (|E_2^s|^2 + |E_3^s|^2) \sin\theta \, d\theta \, d\varphi \right\}. \quad (99)$$

But from (28),

$$E_2^s \sim \frac{-e^{ik_0 r}}{k_0 r} \sum_{m=-\infty}^{\infty} \sum_{\substack{n \geq |m| \\ n \neq 0}} (-i)^n \left[a_{mn} \cdot \frac{m}{\sin\theta} P_n^{|m|}(\cos\theta) + b_{mn} \frac{dP_n^{|m|}(\cos\theta)}{d\theta} \right] e^{im\varphi} \quad (100)$$

and

$$E_3^s \sim \frac{e^{ik_0 r}}{k_0 r} \sum_{m=-\infty}^{\infty} \sum_{\substack{n \geq |m| \\ n \neq 0}} (-i)^{n+1} \left[a_{mn} \frac{dP_n^{|m|}(\cos\theta)}{d\theta} + b_{mn} \cdot \frac{m}{\sin\theta} P_n^{|m|}(\cos\theta) \right] e^{im\varphi}. \quad (101)$$

Substituting (100) and (101) into (99), the integration with respect to φ is straightforward. The integration with respect to θ readily follows with the help of the identities

$$m \int_0^{\pi} \left[P_l^{|m|}(\cos\theta) \frac{dP_n^{|m|}(\cos\theta)}{d\theta} + \frac{dP_l^{|m|}(\cos\theta)}{d\theta} P_n^{|m|}(\cos\theta) \right] d\theta = 0 \quad (102)$$

and[38]

$$\int_0^\pi \left[\frac{dP_l^{|m|}(\cos\theta)}{d\theta}\frac{dP_n^{|m|}(\cos\theta)}{d\theta} + \frac{m^2}{\sin^2\theta}P_l^{|m|}(\cos\theta)P_n^{|m|}(\cos\theta)\right]\sin\theta d\theta = \frac{2n(n+1)(n+|m|)!}{(2n+1)(n-|m|)!}\delta_{ln}, \quad (103)$$

where δ_{ln} denotes the Kronecker delta, i.e., $\delta_{ln} = 1$ for $l = n$, and 0 otherwise. Thus, the expression for W_s given in (36) is obtained.

We remark that there is no need to let $r \to \infty$ to obtain this expression for W_s. The same result follows from (35) by using the expressions (10) and (11) for the scattered field, wherein $\mathbf{M}_{mn}^{(3)}(k_0)$ and $\mathbf{N}_{mn}^{(3)}(k_0)$ are defined by (8) and (9), with $z_n(k_0r) = h_n^{(1)}(k_0r)$. The dependence on r is found to vanish, as is to be expected, in view of the Wronskian relationship[39]

$$j_n(k_0r)y_n'(k_0r) - y_n(k_0r)j_n'(k_0r) = \frac{1}{(k_0r)^2}. \quad (104)$$

We also remark that the expression in (36) holds quite generally, e.g., for scattering from nonaxisymmetric raindrops, since at this point we have made no use of the properties of the coefficients a_{mn} and b_{mn}.

We next consider the calculation of the total energy W_t, which is defined by (41). We begin by allowing for a general incident field, given by

$$\mathbf{E}^i = -\sum_{m=-\infty}^{\infty}\sum_{\substack{n\geq|m|\\ n\neq 0}}[A_{mn}\mathbf{M}_{mn}^{(1)}(k_0) + B_{mn}\mathbf{N}_{mn}^{(1)}(k_0)] \quad (105)$$

and

$$\mathbf{H}^i = \frac{ik_0}{\omega\mu_0}\sum_{m=-\infty}^{\infty}\sum_{\substack{n\geq|m|\\ n\neq 0}}[A_{mn}\mathbf{N}_{mn}^{(1)}(k_0) + B_{mn}\mathbf{M}_{mn}^{(1)}(k_0)], \quad (106)$$

where the superscript 1 indicates that $z_n(k_0r) = j_n(k_0r)$ in (8) and (9). The calculation of W_t is similar to that of W_s and it is found, after some reductions, that

$$W_t = \frac{-2\pi}{\omega\mu_0k_0}\operatorname{Re}\sum_{m=-\infty}^{\infty}\sum_{\substack{n\geq|m|\\ n\neq 0}}\frac{n(n+1)(n+|m|)!}{(2n+1)(n-|m|)!} \times (a_{mn}A_{mn}^* + b_{mn}B_{mn}^*). \quad (107)$$

We now consider the incident electric field given by (42), where $\mathbf{E}_{\mathrm{I}}^i$ and $\mathbf{E}_{\mathrm{II}}^i$ are given by (5) and (6), respectively. Then (43) holds and, from (10) and (11),

$$a_{mn} = a_{mn}^{\mathrm{I}} + a_{mn}^{\mathrm{II}}, \qquad b_{mn} = b_{mn}^{\mathrm{I}} + b_{mn}^{\mathrm{II}}. \quad (108)$$

From (5) and (6) and the expansions in (116) and (117), it follows from (105) to (107) that

$$W_t = \frac{2\pi}{\omega\mu_0 k_0} \operatorname{Re} \sum_{m=-\infty}^{\infty} \sum_{\substack{n \geqq |m| \\ n \neq 0}} (-i)^{n-1} \times \left\{ E_{\mathrm{I}}^* \left[a_{mn} \cdot \frac{m}{\sin \alpha} P_n^{|m|}(\cos \alpha) + b_{mn} \frac{dP_n^{|m|}(\cos \alpha)}{d\alpha} \right] + iE_{\mathrm{II}}^* \left[a_{mn} \frac{dP_n^{|m|}(\cos \alpha)}{d\alpha} + b_{mn} \cdot \frac{m}{\sin \alpha} P_n^{|m|}(\cos \alpha) \right] \right\}. \quad (109)$$

The relations (39) now follow from (33), (34), (40), and (108) by setting first $E_{\mathrm{II}} = 0$ and second $E_{\mathrm{I}} = 0$, in (109). We also note that, from (5), (6), (28), (30), (42), and (109),

$$W_t = \frac{2\pi}{\omega\mu_0 k_0} \operatorname{Re} \left[\lim_{r \to \infty} \left\{ \frac{-ik_0 r e^{-ik_0 r} (\mathbf{E}^i)^* \cdot \mathbf{E}^s \,|_{\theta=\alpha,\ \varphi=0}}{\exp[-ik_0(x \sin \alpha + z \cos \alpha)]} \right\} \right]. \quad (110)$$

We remark that both (109) and (110) hold, subject to (42), (43), and (108), for scattering from generally shaped raindrops.

Finally, we consider the particular case of an axisymmetric raindrop given by $r = R(\theta)$, so that (23) and (24) hold. Thus,

$$(a_{mn}^{\mathrm{I}} a_{mn}^{\mathrm{II}*} + b_{mn}^{\mathrm{I}} b_{mn}^{\mathrm{II}*}) = -(a_{-mn}^{\mathrm{I}} a_{-mn}^{\mathrm{II}*} + b_{-mn}^{\mathrm{I}} b_{-mn}^{\mathrm{II}*}). \quad (111)$$

Hence, from (36) and (108),

$$W_s = W_s^{\mathrm{I}} + W_s^{\mathrm{II}}. \quad (112)$$

Then, from (37), with

$$Q_s = \frac{2\omega\mu_0 W_s}{k_0(E_{\mathrm{I}} E_{\mathrm{I}}^* + E_{\mathrm{II}} E_{\mathrm{II}}^*)}, \quad (113)$$

we obtain (44). Also, from (23), (24), (108), and (109),

$$W_t = W_t^{\mathrm{I}} + W_t^{\mathrm{II}}. \quad (114)$$

Hence, from (40), with

$$Q_t = \frac{2\omega\mu_0 W_t}{k_0(E_{\mathrm{I}} E_{\mathrm{I}}^* + E_{\mathrm{II}} E_{\mathrm{II}}^*)}, \quad (115)$$

we obtain (45).

APPENDIX D

We first give the expansions for the incident wave in terms of spherical vector wave functions.[4,19] It is found that

$$(\cos\alpha\mathbf{i} - \sin\alpha\mathbf{k}) \exp[ik_0(x\sin\alpha + z\cos\alpha)]$$
$$= -\sum_{m=-\infty}^{\infty}\sum_{\substack{n=|m|\\ n\neq 0}}^{\infty} \frac{i^{n+1}(2n+1)(n-|m|)!}{n(n+1)(n+|m|)!}$$
$$\times\left[\frac{m}{\sin\alpha}P_n^{|m|}(\cos\alpha)\mathbf{M}_{mn}^{(1)}(k_0) + \frac{dP_n^{|m|}(\cos\alpha)}{d\alpha}\mathbf{N}_{mn}^{(1)}(k_0)\right] \quad (116)$$

and

$$\mathbf{j}\exp[ik_0(x\sin\alpha + z\cos\alpha)]$$
$$= -\sum_{m=-\infty}^{\infty}\sum_{\substack{n=|m|\\ n\neq 0}}^{\infty} \frac{i^{n}(2n+1)(n-|m|)!}{n(n+1)(n+|m|)!}$$
$$\times\left[\frac{dP_n^{|m|}(\cos\alpha)}{d\alpha}\mathbf{M}_{mn}^{(1)}(k_0) + \frac{m}{\sin\alpha}P_n^{|m|}(\cos\alpha)\mathbf{N}_{mn}^{(1)}(k_0)\right]. \quad (117)$$

Expressions for the quantities $\mathbf{e}_m(r,\theta)$ and $\mathbf{h}_m(r,\theta)$, defined in (20), then follow from (5), (6), (8), and (9). Thus, we may now consider the boundary conditions (81) to (84).

We first multiply (81) by $dP_l^{|m|}(\cos\theta)/d\theta \sin\theta$ and (83) by $im\,P_l^{|m|}(\cos\theta)$ and add, and then multiply (81) by $im\,P_l^{|m|}(\cos\theta)$ and (83) by $dP_l^{|m|}(\cos\theta)/d\theta \sin\theta$ and subtract, and integrate both these equations with respect to θ from 0 to π. In the zero-order approximation corresponding to $\nu = 0$ in (47), this leads, with the help of (102) and (103), to simultaneous linear equations for $a_{ml}^{(0)}$ and $c_{ml}^{(0)}$. Similarly, multiplying (82) by $dP_l^{|m|}(\cos\theta)/d\theta \sin\theta$ and (84) by $im\,P_l^{|m|}(\cos\theta)$ and adding, and multiplying (82) by $im\,P_l^{|m|}(\cos\theta)$ and (84) by $dP_l^{|m|}(\cos\theta)/d\theta \sin\theta$ and subtracting, and integrating both these equations with respect to θ from 0 to π, we obtain simultaneous linear equations for the zero-order coefficients $b_{ml}^{(0)}$ and $d_{ml}^{(0)}$. The solution of these two pairs of simultaneous equations leads to the relations (50) and (51), where the quantities α_{mn} and β_{mn} depend on the polarization, as given by (52) and (53). It remains to give the expressions for the quantities a_n, b_n, c_n, and d_n occurring in (50) and (51).

We define

$$F_n(\xi) = \left[\frac{h_n^{(1)}(\xi)}{\xi} + h_n^{(1)'}(\xi)\right], \qquad G_n(\xi) = \left[\frac{j_n(\xi)}{\xi} + j_n'(\xi)\right]. \quad (118)$$

Then, with $\rho = k_0 a$, it is found that

$$a_n = \frac{[j_n(\rho)NG_n(N\rho) - j_n(N\rho)G_n(\rho)]}{[h_n^{(1)}(\rho)NG_n(N\rho) - j_n(N\rho)F_n(\rho)]}, \quad (119)$$

$$b_n = \frac{[j_n(\rho)G_n(N\rho) - Nj_n(N\rho)G_n(\rho)]}{[h_n^{(1)}(\rho)G_n(N\rho) - Nj_n(N\rho)F_n(\rho)]}, \quad (120)$$

and

$$c_n = (i/\rho^2)[h_n^{(1)}(\rho)NG_n(N\rho) - j_n(N\rho)F_n(\rho)]^{-1}, \quad (121)$$

$$d_n = (i/\rho^2)[h_n^{(1)}(\rho)G_n(N\rho) - Nj_n(N\rho)F_n(\rho)]^{-1}. \quad (122)$$

In obtaining (121) and (122), we have made use of the Wronskian relationship[39]

$$j_n(\rho)h_n^{(1)\prime}(\rho) - h_n^{(1)}(\rho)j_n'(\rho) = (i/\rho^2). \quad (123)$$

Next, considering the first-order terms in ν in the integrated forms of the boundary conditions, and making use of (47) to (49), two pairs of simultaneous linear equations are obtained for $a_{mn}^{(1)}$ and $c_{mn}^{(1)}$ and for $b_{mn}^{(1)}$ and $d_{mn}^{(1)}$. These equations contain somewhat involved expressions, but after considerable reductions they lead to the expressions given in (54) to (56), subject to (57) to (62). In particular, use has been made of the differential equation satisfied by the spherical Bessel functions,[39]

$$\xi^2 z_l''(\xi) + 2\xi z_l'(\xi) + [\xi^2 - l(l+1)]z_l(\xi) = 0. \quad (124)$$

Moreover, from (118) to (124) it follows that

$$j_l(\rho) - a_l h_l^{(1)}(\rho) + c_l j_l(N\rho) = 0, \quad (125)$$

$$j_l'(\rho) - a_l h_l^{(1)\prime}(\rho) + Nc_l j_l'(N\rho) = 0, \quad (126)$$

$$G_l'(\rho) - a_l F_l'(\rho) + N^2 c_l G_l'(N\rho) = (1 - N^2)c_l j_l(N\rho), \quad (127)$$

$$Nj_l(\rho) - Nb_l h_l^{(1)}(\rho) + d_l j_l(N\rho) = (1 - N^2)d_l j_l(N\rho), \quad (128)$$

$$j_l'(\rho) - b_l h_l^{(1)\prime}(\rho) + N^2 d_l j_l'(N\rho) = (N^2 - 1)d_l G_l(N\rho), \quad (129)$$

and

$$N\rho^2[G_l'(\rho) - b_l F_l'(\rho) + Nd_l G_l'(N\rho)] = l(l+1)(1 - N^2)d_l j_l(N\rho). \quad (130)$$

We have also used the fact that

$$\int_0^\pi P_l^{|m|}(\cos\theta)\frac{dP_n^{|m|}(\cos\theta)}{d\theta}\sin\theta\frac{d\sigma_1}{d\theta}d\theta = \frac{n(n+1)}{l(l+1)}\mathfrak{Z}\mathfrak{C}_{nl}^m - \mathfrak{g}_{nl}^m, \quad (131)$$

where $\mathfrak{Z}\mathfrak{C}_{nl}^m$ and $\mathfrak{g}_{nl}^m$ are given by (60) and (61). This result follows directly by integration by parts and use of the differential equation satisfied by the associated Legendre functions,[14]

$$\frac{1}{\sin\theta}\frac{d}{d\theta}\left[\sin\theta\frac{dP_n^{|m|}(\cos\theta)}{d\theta}\right] + \left[n(n+1) - \frac{m^2}{\sin^2\theta}\right]P_n^{|m|}(\cos\theta) = 0. \quad (132)$$

APPENDIX E

We outline here the calculation of the integrals in (60) to (62) in the case

$$\sigma_1(\theta) = \tfrac{1}{2}\sin^2\theta. \tag{133}$$

It is assumed that $l \geqq |m|$, $n \geqq |m|$, $l \neq 0$ and $n \neq 0$. Integration by parts of the expression in (62) leads to

$$\begin{aligned}\mathcal{J}_{nl}^{m} &= -m\int_0^{\pi} P_l^{|m|}(\cos\theta)P_n^{|m|}(\cos\theta)\sin\theta\cos\theta d\theta \\ &= -m\int_{-1}^{1} xP_l^{|m|}(x)P_n^{|m|}(x)dx.\end{aligned} \tag{134}$$

But,[14] with $P_{|m|-1}^{|m|}(x) \equiv 0$,

$$(2l+1)xP_l^{|m|}(x) = (l-|m|+1)P_{l+1}^{|m|}(x) + (l+|m|)P_{l-1}^{|m|}(x). \tag{135}$$

Substituting (134) into (135), and using the relationship[14]

$$\int_{-1}^{1} P_l^{|m|}(x)P_n^{|m|}(x)dx = \frac{2(n+|m|)!}{(2n+1)(n-|m|)!}\,\delta_{ln}, \tag{136}$$

it follows from (62) that

$$J_{nl}^{m} = \frac{-m}{n(n+1)}\left[\frac{(n-|m|)}{(2n-1)}\,\delta_{l,n-1} + \frac{(n+|m|+1)}{(2n+3)}\,\delta_{l,n+1}\right]. \tag{137}$$

Next, from (60) and (133),

$$\mathcal{K}_{nl}^{m} = \frac{1}{2}l(l+1)\int_{-1}^{1}(1-x^2)P_l^{|m|}(x)P_n^{|m|}(x)dx. \tag{138}$$

The integral in (138) may be evaluated by using (136) and the recurrence relation (135), with l replaced by n also. Then, from (60), it is found that

$$\begin{aligned}H_{nl}^{m} = {} & \frac{n(n+1)(m^2+n^2+n-1)}{(2n-1)(2n+3)}\,\delta_{ln} \\ & - \frac{(n+2)(n+3)(n+|m|+1)(n+|m|+2)}{2(2n+3)(2n+5)}\,\delta_{l,n+2} \\ & - \frac{(n-2)(n-1)(n-|m|)(n-|m|-1)}{2(2n-3)(2n-1)}\,\delta_{l,n-2}.\end{aligned} \tag{139}$$

Finally, from (61) and (133),

$$g_{nl}^{m} = \frac{1}{2}\int_{-1}^{1}\left[(1-x^2)^2\frac{dP_l^{|m|}(x)}{dx}\frac{dP_n^{|m|}(x)}{dx} + m^2P_l^{|m|}(x)P_n^{|m|}(x)\right]dx. \tag{140}$$

The integral in (140) may be evaluated by using (136) and the relation[14]

$$(2k+1)(1-x^2)\frac{dP_k^{|m|}(x)}{dx} = (k+1)(k+|m|)P_{k-1}^{|m|}(x) - k(k-|m|+1)P_{k+1}^{|m|}(x). \quad (141)$$

Then from (61) it is found that

$$I_{nl}^m = \frac{1}{2}\left\{\frac{m^2}{n(n+1)} + \frac{n[(n+1)^2-m^2]}{(n+1)(2n+1)(2n+3)} + \frac{(n+1)(n^2-m^2)}{n(4n^2-1)}\right\}\delta_{ln} - \frac{(n+3)(n+|m|+1)(n+|m|+2)}{2(n+1)(2n+3)(2n+5)} \times \delta_{l,n+2} - \frac{(n-2)(n-|m|)(n-|m|-1)}{2n(2n-3)(2n-1)}\delta_{l,n-2}. \quad (142)$$

We note that the above results are consistent with the expressions given by Oguchi,[4] without derivation, for the integrals in (131), (61), and (62), subject to (133).

REFERENCES

1. J. A. Morrison, M.-J. Cross, and T. S. Chu, "Rain-Induced Differential Attenuation and Differential Phase Shift at Microwave Frequencies," B.S.T.J., *52*, No. 4 (April 1973), pp. 599–604.
2. H. R. Pruppacher and R. L. Pitter, "A Semi-Empirical Determination of the Shape of a Cloud and Rain Drops," J. Atmosph. Sci., *28*, No. 1 (January 1971), pp. 86–94.
3. H. C. Van de Hulst, *Light Scattering by Small Particles*, New York: Wiley, 1957, p. 34.
4. T. Oguchi, "Attenuation of Electromagnetic Wave Due to Rain with Distorted Raindrops," J. Radio Res. Labs. (Tokyo), *7*, No. 33 (September 1960), pp. 467–485.
5. T. Oguchi, "Attenuation and Phase Rotation of Radio Waves Due to Rain: Calculations at 19.3 and 34.8 GHz," Radio Sci., *8*, No. 1 (January 1973), pp. 31–38.
6. J. A. Stratton, *Electromagnetic Theory*, New York: McGraw-Hill, 1941, pp. 563–565.
7. D. E. Setzer, "Computed Transmission Through Rain at Microwave and Visible Frequencies," B.S.T.J., *49*, No. 8 (October 1970), pp. 1873–1892.
8. P. S. Ray, "Broadband Complex Refractive Indices of Ice and Water," Appl. Opt., *11*, No. 8 (August 1972), pp. 1836–1844.
9. J. A. Morrison and T. S. Chu, "Perturbation Calculations of Rain-Induced Differential Attenuation and Differential Phase Shift at Microwave Frequencies," B.S.T.J., *52*, No. 10 (December 1973), pp. 1907–1913.
10. Ref. 6, p. 137.
11. Ref. 6, p. 37.
12. Ref. 6, pp. 414–416.
13. Ref. 6, pp. 404–406.
14. W. Magnus and F. Oberhettinger, *Formulas and Theorems for the Functions of Mathematical Physics*, New York: Chelsea, 1954, pp. 53–54.
15. Ref. 6, pp. 568–569.
16. Ref. 3, p. 13.
17. Ref. 3, p. 31.

18. T. Oguchi, "Attenuation of Electromagnetic Wave Due to Rain with Distorted Raindrops (Part II)," J. Radio Res. Labs. (Tokyo), *11*, No. 53 (January 1964), pp. 19–44.
19. P. M. Morse and H. Feshbach, *Methods of Theoretical Physics*, New York: McGraw-Hill, 1953, p. 1866.
20. C. R. Mullin, R. Sandburg, and C. O. Velline, "A Numerical Technique for the Determination of Scattering Cross Sections of Infinite Cylinders of Arbitrary Geometrical Cross Section," IEEE Trans. Ant. and Prop., *AP-13*, No. 1 (January 1965), pp. 141–149.
21. P. Businger and G. H. Golub, "Linear Least Squares Solutions by Householder Transformations," Numer. Math., *7*, No. 4 (September 1965), pp. 269–276.
22. E. Sonnenblick, "A Program to Compute Bessel Functions J and Y of Complex Argument, Integer Order," unpublished work.
23. M. Abramowitz and I. A. Stegun, *Handbook of Mathematical Functions*, Washington: National Bureau of Standards, 1964, pp. 390–407.
24. D. S. Drumheller, "A New Method for Generating Spherical Bessel Functions," unpublished work.
25. Ref. 23, p. 439.
26. Ref. 23, pp. 457–466.
27. U. S. Math Tables Project, *Tables of Spherical Bessel Functions*, Vols. I and II, New York: Columbia, 1947.
28. A. E. Kaplan, "Numerical Generation of Spherical Bessel Functions of Real and Complex Arguments," unpublished work.
29. Ref. 23, pp. 469–473.
30. L. Robin, *Fonctions Sphériques de Legendre et Fonctions Sphéroidales*, Tome 1, Paris: Gauthier-Villars, 1957, pp. 74–75, 82–83.
31. Ref. 6, p. 401.
32. S. L. Belousov, *Tables of Normalized Associated Legendre Functions*, New York: Macmillan, 1962.
33. U. S. Math Tables Project, *Tables of Associated Legendre Functions*, New York: Columbia, 1945.
34. T. Oguchi, private communication.
35. T. Oguchi, "Scattering Properties of Oblate Raindrops and Cross Polarization of Radio Waves Due to Rain: Calculations at 19.3 and 34.8 GHz," J. Radio Res. Labs. (Tokyo), *20*, No. 102 (1973), pp. 79–118.
36. Ref. 23, p. 360.
37. Ref. 23, p. 361.
38. Ref. 6, p. 417.
39. Ref. 23, p. 437.